Politecnico di Torino

AVL

POLITECNICO DI TORINO

Master's Degree in Aerospace Engineering

A.y 2023/2024

Graduation session: July

Comparative Aeroacustic Analysis of Rotating Axial Fans

University Supervisors:

Prof. Francesco Avallone
Prof. Domenic D'Ambrosio

Company supervisor:

Ing. Johannes Tieber

Candidate

Leonardo Mihael Giordo

JULY 2024

A mio nonno.

Abstract

This thesis addresses the challenge of noise generation by cooling fans in electric vehicles (EVs). The transition from fossil fuel-powered vehicles to EVs has introduced new challenges, one of which is the noise produced by these fans. This noise can cause discomfort and annoyance, especially when the vehicle is stationary.
The study focuses on the aeroacoustic analysis of a low-pressure axial fan, a common type of fan used in EVs. The operation of EVs heavily relies on their batteries, which generate significant heat during the fast-charging process. This heat needs to be managed effectively to prevent battery degradation and ensure optimal performance. Fan-based cooling systems, which work on the principle of forced convection, are commonly used due to their simplicity, cost-effectiveness, and easy integration. However, they also contribute to the noise problem.
The methodology employed for the analysis is Computational Aeroacoustics (CAA), a branch of acoustics that deals with the noise generated by the movement of the flow and its interaction with itself and the surroundings.
The goal of this thesis, conducted in cooperation with AVL LIST GmbH (AVL) and Polytechnic University of Turin, is to numerically predict the noise produced by an axial fan.
The study will also assist in the development of a computational aeroacoustic hybrid approach and investigate the ability of commercial software Star-ccm+ and FIRE M to capture acoustic phenomena through the use of the Perturbed Convective Wave Equation acoustic model.
The acoustic spectrum of a fan consists of broadband noise and tonal components, with the strongest source of noise usually being unsteady blade forces. This thesis explores these noise mechanisms and their contribution to the overall noise level.
In order to perform a CAA simulation with the Hybrid approach, the acoustic source terms have to be derived from the Computational Fluid Dynamic (CFD) simulation. Throughout this thesis the CFD results of the two software will be compared with a benchmark study. While in Star-ccm+ the acoustic solver is already implemented, in FIRE M the source terms have to be computed from the fluid-dynamic quantities mapped on the acoustic mesh. In order to perform those operations Python scripts have been developed. Finally, through the use of the open-source software OpenCFS, the PCWE simulation can be conducted.
While, due to time constraints, the simulation time of FIRE M was not enough to be able to capture the important frequencies with a Power Spectral Density analysis; with Star-ccm+ was possible to capture the tonal components due to interaction between turbulence structures and the blade on the far-field microphones with good accuracy. The Blade Passing Frequencies were captured by the wall pressure sensors.
The findings of this study will contribute to the ongoing research and development in this field, aiming to improve the thermal management of EVs during fast charging and enhance the overall user experience.

Acknowledgements

I would like to express my gratitude to Professors Avallone Francesco and D'Ambrosio Domenic, supervisors of this thesis project, for giving me trust and support during this work. In particular, to Prof. D'Ambrosio for giving me solid theoretical and practical knowledge which was immensely useful during this journey and to Prof. Avallone for his guidance and extreme availability and patience towards me.

I would like to thank my company's supervisor Tieber Johannes, for his unwavering support and assistance throughout this project. I also want to acknowledge and thank the confidence placed in my abilities by Skill Area Manager Ennemoser Andreas and Team Leader Machold Alexander.

Un Enorme ringraziamento alla mia famiglia, per essermi stati sempre vicino, di supporto e incoraggiamento, tutti i giorni della mia vita. In particolare, a mia sorella, per essere stata un esempio di forza, dimostrandomi come superare le difficoltà; a mia mamma, per l'amore incondizionato e il supporto infinito, ti ammiro tantissimo; e a mio padre, per essere stato un esempio di giustizia e diligenza impareggiabile.
È grazie al vostro affetto che sono giunto a questo obbiettivo.
Grazie a mia nonna, la tua forza e tenacia così come le tue preghiere e le tue polpette sono di sostegno per tutta la famiglia, in particolare per noi nipoti. Un grandissimo saluto anche a mio nonno.
Grazie anche a tutti i parenti vicini e lontani.

Un enorme grazie ad Edli, fantastica compagna di avventure, per essermi stata vicina nei momenti difficili e durante la fine di questo percorso e per avermi insegnato a vedere il mondo in maniera diversa.

E infine un grazie agli amici che mi hanno accompagnato in tanti anni di università, sport e non solo.

Table of Contents

List of Figures

List of Tables

Nomenclature

List of Symbols

Latin Symbols

$\bar{a}$	generic signal speed
a_{ij}	anisotropic tensor
A_c	acoustic correlation area
c_0	speed of sound
c_v	specific heat capacity at constant volume
c_p	specific heat capacity at constant pressure
C	generic constant
E	energy
e	specific energy
f	frequency
f	elliptic relaxation function in $k-\zeta-f$ turbulence model
$\mathbf{f}$	external force
f	net flux through a surface
f_{co}	cut-off frequency
$\boldsymbol{F}_{\mathbf{c}}$	vector of convective fluxes
F_{CSM}	function used in CSM turbulence model
F_1	blending function used in $k-\omega$ turbulence model
G	Green's function
$\mathcal{G}$	Spatial Filter in LES
H	Heavyside functions
I_{i}	Diffusive term in RANS
k	turbulent kinetic energy
t	thermal conductivity of a material
l	characteristic length
l_S	Smagorinsky length scale
l_m	mixing length scale
L	characteristic length
L_W	sound power level
L_P	sound pressure level
M	Mach number
M_Q	Torque
n	rotational speed
N	number of microphones
$\mathcal{N}$	number of blades
p	pressure
P_W	sound power
Pr	Prandtl number
P	generic production term
P_{SA}	surface acoustic power
$\boldsymbol{q}$	heat flow

Q_m	acoustic source term of mass
Q_w	acoustic source term of energy
r	radial coordinate
R	specific gas constant
Re	Reynolds number
s	entropy
S	generic surface
$\mathcal{S}$	strain tensor
t	time
t	delayed time
T	temperature
$\mathcal{T}$	length of the signal
T_{ij}	Lighthill tensor
u	velocity
V	volume
$\dot{V}$	volumetric flow rate
$\boldsymbol{W}$	vector of conservative variables
x	x coordinate
x	generic fluid-dynamic variable
X	generic signal
$\mathcal{X}$	generic field variable
y	y coordinate

Greek Symbols

α	constant of Proudman model
β	constant
γ	adiabatic index
δ	elementary Dirac delta impulse
δ_{ij}	Identity matrix in vectorial notation
Δ	filter dimension
ε	turbulence dissipation rate
ζ	damping function in $k - \zeta - f$ turbulence model
η	fan efficiency
θ	angular coordinate
κ	Von Karman constant
λ	volume viscosity
μ	dynamic viscosity
ν	kinematic viscosity
Π	turbulent kinetic energy production term
$\boldsymbol{\Pi}$	stress tensor
ρ	density
σ_{ij}	stress tensor is vectorial notation
σ_k	turbulent Prandtl number for k
σ_ω	turbulent Prandtl number for ω
$\sigma_{k\zeta f}$	$k - \zeta - f$ turbulence model parameter
τ	viscous stress term
τ_w	wall shear stress

τ_{ij}^{an}	anisotropic residual stress tensor
ψ^{a}	acoustic potential
φ	generic quantity
ω	specific dissipation rate
Ω	mean rate of rotation

Superscript Symbols

$'$	fluctuating variable based of temporal average
$''$	unresolved variable by LES
$^{+}$	dimensionless quantity normalized with the wall friction velocity
^{a}	acoustic

Subscripts Symbols

c	compressible
d	deformation
CSM	CSM turbulence model
i	directional index x-direction
j	directional index y-direction
k	directional index z-direction
$\hbar$	turbulent kinetic energy
$\hbar\zeta f$	$\hbar - \zeta -$ f turbulence model
m	mixing length
n	microphone number
N	computational cell node
rms	root mean square
ref	reference
S	Smagorisnky
SGS	subgrid scale
t	time derivation
turb	turbulence
WALE	WALE turbulence model
x	derivation by x
y	derivation by y
z	derivation by z

Chapter 1: Introduction

In the subsequent chapter, exploration into the motivation and background that form the foundation of this thesis is presented in *Section 1.1*. This is followed by *Section 1.2*, which introduces Electric Vehicles and discusses the challenges posed by electrification. The objectives of the thesis are articulated in *Section 1.3*. and finally, to conclude the chapter, *Section 1.4* provides an overview of the main physical phenomena investigated in this thesis.

1.1 Motivation and background

The cabin and external noise of modern vehicles is strongly affected by the sound generated by the movement of fluid outside and inside the vehicle. Specifically, when the vehicle is stationary, fans and outlets of the air conditioning/cooling system constitute the main sources of noise and can reduce the comfort of the occupants and passengers [1].
The noise generated by an axial fan is a complex phenomenon that varies considerably depending on whether the fan is in a duct or free.
The advent of electric vehicles (EVs) has revolutionized the automotive industry, paving the way for a sustainable future. The electrification of modern automobiles is driven by the necessity to reduce carbon emissions and combat climate change. However, as the transition from fossil fuel-powered vehicles to electric ones happens, new challenges arise that require innovative solutions.
One such challenge is the noise generated by cooling fans of electric vehicles during the fast-charging process. Fast charging is a crucial feature that makes EVs more practical for everyday use, significantly reducing the time it takes to recharge the vehicle's battery. However, this process generates a substantial amount of heat that needs to be dissipated to prevent damage to the battery and ensure optimal performance. This is typically achieved using cooling fans.
While these fans are effective in cooling the battery, they also generate noise, which can be a source of discomfort and annoyance to both the users and those in the offing. This is especially noticeable when the car is stationary with the engine off.
In numerous applications involving flow dynamics, the primary sources of noise are typically attributed to aerodynamic factors, such as variations in the pressure field due to turbulent motion. This branch of acoustics is referred as aeroacoustics. The aeroacoustic analyses conducted in this study are focused on a low-pressure axial fan benchmark, allowing for a comparison of the findings with actual measurements. The numerical methodology employed to address this issue is known as Computational Aeroacoustics (CAA), which is closely linked with Computational Fluid Dynamics (CFD) for the prediction of aerodynamic variables. Consequently, the initial objective of this study is to acquire CFD data that accurately depicts the flow field. It is crucial to note that the goal is to capture not just the aerodynamic variables, but also the fluctuations that generate sound.

1.2 Fan cooling system during EVs fast charging

The operation of each electric vehicle is dependent on its EV batteries; hence the progression of EV battery technology is intrinsically linked to the evolution of electric vehicles. It's incumbent upon today's electric vehicle manufacturers to equip their models with appropriate

EV batteries, as the performance of each vehicle is significantly influenced by its battery. A high-quality EV battery not only ensures that all the vehicle's features are adequately powered, but it also provides sufficient energy for the vehicle to cover the intended distance.
EV batteries have the role of powering every aspect of the vehicle, including the wheel movements and tractions, the features offered by the vehicle, the electrical systems and many others [2].
One of the critical challenges in the operation of EVs is the management of heat generated during the fast-charging process. Fast charging is a desirable feature in EVs as it reduces downtime and enhances the usability of the vehicle. However, it also leads to significant heat generation in the battery due to the high current flow. This heat, if not managed properly, can lead to battery degradation, reduced performance, and in extreme cases, safety hazards.
The primary function of a cooling system in an EV is to maintain the battery temperature within an optimal range, ensuring its longevity and performance. During fast charging, the rate of heat generation exceeds the battery's natural dissipation rate, necessitating an active cooling system. Fan-based cooling systems are a popular choice due to their simplicity, cost-effectiveness, and easy integration. They work on the principle of forced convection, where the airflow around the battery is increased, enhancing the heat dissipation rate. The air absorbs the heat from the battery cooling system and is then expelled out, thereby maintaining the battery temperature. Fan-based cooling systems are relatively easy to implement and maintain. They are also energy-efficient, as they only operate when the temperature exceeds a certain threshold. However, for extremely high charging rates or at high ambient temperatures, they are not able to cope with the heat production and they can be damaged.
As EVs continue to evolve, so will the methods to keep them running efficiently and safely. Fan-based cooling systems, with their simplicity and effectiveness, are expected to remain a vital component in the thermal management of EVs during fast charging. However, continuous research and development in this field is essential to meet the growing demands of fast charging and improved battery performance.

1.3 Aim of the Thesis

The aim of this thesis, in cooperation with AVL LIST GmbH (AVL) and Polytechnic University of Turin, will be the numerical prediction of the noise produced by an axial fan to develop noise mitigation strategies.
The target of this Master Thesis project is to perform CFD and CAA simulations with the objective being the study of acoustic characteristics of flow.
Furthermore, the company's development of a computational aeroacoustic Hybrid approach will be assisted.
And finally, the ability of the commercial software Star-ccm+ and FIRE M to capture acoustic phenomena will be investigated and juxtaposed, using the experimental results found in literature, obtained from the same benchmark fan as comparison.

1.4 Axial fans noise

The acoustic spectrum of a fan is made up of broadband noise and tonal components [3]. The lower limit of the Sound Pressure Level is determined by the ambient noise. At low speeds and low frequencies, the spectrum is dominated by steady blade forces. These forces, although constant on the rotating fan, create a rotating pressure field for the stationary observer.
Unsteady blade forces result in tonal components at the Blade Passing Frequency (BPF) and its higher harmonics. These can be caused by turbulent, non-uniform inflow or rotor-stator

interactions and are usually the strongest source of noise. The interaction of the upstream flow with the blades is strongest at the leading edges.
The noise mechanism investigated above belongs to the Loading noise contribute see eq. (2.35) in *Chapter 2.4.3*; regarding the Thickness noise, it appears to be influential only at transonic speeds.
Noise mechanisms of turbulent and laminar vortex shedding are found in the higher frequency range. If laminar shedding occurs, it can have a strong tonal characteristic. These noise mechanisms can occur independently of the upstream flow and are similar to airfoil noise.
In turbulent boundary layers, turbulent structures interact with the trailing edge and produce noise. If the trailing edge is blunt, a von Kármán vortex street can form behind the profile and generate vortex shedding noise. This results in broadband noise due to the less coherent interactions caused by turbulence in the boundary layer.
Vortex shedding noise can also occur on sharp trailing edges if the boundary layer is laminar, resulting in a distinct peak due to its more coherent nature. Broadband noise sources occur because of flow separation and stall at the blades or a rotating stall on the fan.
In airfoils, a tip vortex, which also generates noise, occurs. In the case of a ducted fan, this corresponds to the sound produced by the tip flow moving between the blade tip and the duct. The tip flow induces a secondary flow, which moves in a circumferential direction with a velocity lower than the rotational velocity of the fan. This secondary flow can interact with the following blades and produce noise at different frequencies than the BPF, commonly referred to as subharmonic tip noise in the literature.
As for a ducted fan, in general, only certain modes can propagate in a duct at a given frequency, but there is an exception: if the duct is short (less than an acoustic wavelength), the non-propagating modes can still reach the inlet and couple with the acoustic far field.

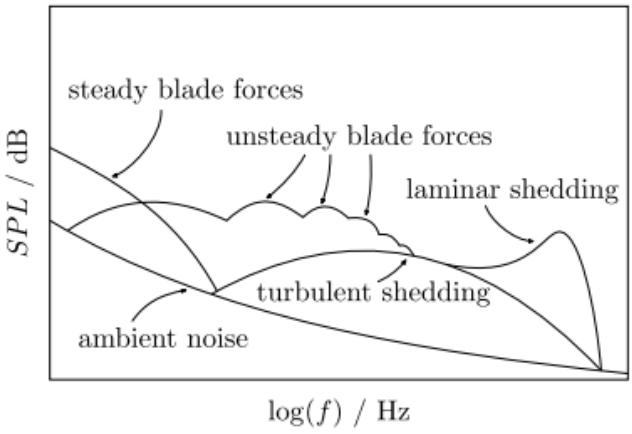

Figure 1.1: Acoustic spectrum of axial fans [4]

Chapter 2: Aeroacustics

To understand the complex phenomena that occur in the generation of noise from an axial fan, it is necessary to have a solid theoretical knowledge of the phenomenon under discussion. In this chapter the equations that govern aerodynamic and aeroacoustic phenomena will be discussed. In *Section 2.1* a brief introduction of the phenomena underlying sound generation will be made. In *Section 2.2* the conservation equations of fluid mechanics will be introduced up until arriving at the Navier Stokes equations, from them then, in *Section 2.3*, the focus will be directed on to the equations describing noise generation and finally, in *Chapter 2.4*, the acoustics analogies will be investigated.

2.1 Basic concepts of Acoustics

In this section, the basics for understanding acoustic and aeroacoustic phenomena will be introduced.

2.1.1 Sound

Sound describes oscillations in an elastic medium such as gas, liquid or solid.
In gases, these oscillations are associated with small fluctuations in pressure, density and velocity which propagate in the form of longitudinal waves which are associated with energy transport. In general, it is also possible to have transverse waves, but the reason why the longitudinal ones are prevalent in fluids, is because fluids cannot resist shear forces while at rest and transverse waves involve displacements and oscillations which are perpendicular to the direction of the wave propagation, that would mean that, in order to see those waves, a shear deformation of the material would be necessary.
Sound waves create zones of compression and expansion in the direction in which they propagate, the speed at which they propagate is called the speed of sound and the rate of expansion-compression defines the frequency of that particular sound wave.
The perception of sound is a response to physical stimulation of the ear in response to the change in pressure on the tympanic membrane. Humans are able to perceive a range of frequencies between 20 Hz and 20 kHz with a peak sensitivity in the 1000 Hz - 5000 Hz range [5].

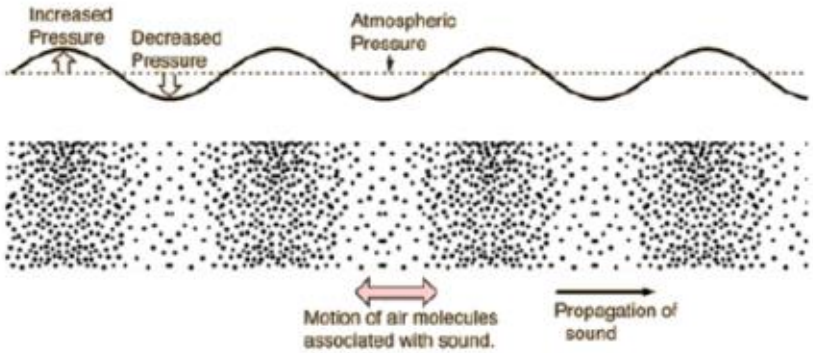

Figure 2.1: Sound pressure waves [5]

2.1.2 Sound speed

Sound is defined as an isentropic perturbation, where the speed of sound c_0 is defined as:

$$c_0 = \sqrt{\left(\frac{\partial p}{\partial \rho}\right)_s} \quad (2.1)$$

where p is the pressure and ρ is the density.
Modeling the fluid as an ideal gas, it is possible to obtain: $c_0 = \sqrt{\gamma RT}$, where γ is the adiabatic index, R is the specific gas constant and T is the temperature. The speed of sound is a function of temperature.
In standard conditions ($T = 15°$): $c_0 = 340\text{m/s}$.

2.1.3 Measurement of Sound

When studying acoustic phenomena, particular attention is generally paid to human sensitivity to noise.
Since Sound Power Levels (L_w) are included in an extremely wide range, it is necessary to use a measurement based on a logarithmic scale [5].
The Sound Power Level is defined in decibels:

$$L_w = 10\, log_{10}\left(\frac{P_w}{P_{w_{\text{ref}}}}\right) \quad (2.2)$$

where P_w is the sound power and $P_{w_{\text{ref}}}$ is the reference sound power.
Sound pressure $p'(t) = p(t) - \langle \text{p} \rangle$, is defined as the variation in pressure $p(t)$ compared to the temporal average value $\langle \text{p} \rangle$ of the same pressure signal, the latter is defined as follows:

$$\langle p \rangle = \frac{1}{\mathcal{T}} \int_{t_0}^{t_0+\mathcal{T}} p(t)dt. \quad (2.3)$$

where t_0 is the starting time and $\mathcal{T}$ is the length of the signal.
Sound pressure variations involve different orders of magnitude; therefore, they are commonly expressed on a logarithmic scale, the Sound pressure level (L_P) is defined as:

$$L_P = 10 \log_{10}\left(\frac{p'^2_{\text{rms}}}{p^2_{\text{ref}}}\right) = 20 \log_{10}\left(\frac{p'_{\text{rms}}}{p_{\text{ref}}}\right), \quad (2.4)$$

where p_{ref} corresponds to the sound level of the hearing threshold, which is directly linked to the pressure fluctuations associated with molecular agitation, for air $p_{\text{ref}} = 20$ μPa.
Referring to the root mean square p'_{rms} helps to better capture a significant change in the pressure value:

$$p'^2_{\text{rms}} = \langle \text{p} \rangle^2 = \frac{1}{\mathcal{T}} \int_{t_0-\mathcal{T}/2}^{t_0+\mathcal{T}/2} p'^2(t)dt. \quad (2.5)$$

When studying sound, it is better to move the problem to the frequency domain. This approach is preferable because the pressure variations are very rapid and are thus easier to study. Furthermore, studying the frequencies with which most of the energy is associated could provide information on the phenomenon of its generation or, from an engineering point of view, one could try to act on these frequencies to mitigate the noise.
By applying the Fourier transform, it is possible to transform a signal $X(t)$ from the time domain t to the frequency domain f:

$$X(f) = \int_{-\infty}^{+\infty} X(t) e^{-i2\pi f t} dt \qquad (2.6)$$

From a practical point of view, the Discrete Fourier Transform (DFT) is used: given a discrete signal x_k, it is sampled N times ($k = 0, 1, 2, \dots, N-1$) with a time step equal to $\Delta t = 1/f_s$, where f_s corresponds to the sampling frequency. The Fourier transform is calculated as:

$$X_m = \Delta t \sum_{k=0}^{N-1} X_k e^{-2\pi i t_k f_m}, \qquad (2.7)$$

in this way it is possible to calculate the contribution of each *m*-th frequency.

2.2 Governing Equations

In this section the equations underlying fluid dynamics will be introduced.
There are two possible mathematical formulations with which a system can be described: the Lagrangian formulation and the Eulerian formulation.
In the Lagrangian formulation, the movement of a single particle which has quantities such as mass, pressure, temperature and speed, is followed. The reference system moves together with the particle.
On the contrary, in an equation written with the Eulerian formulation, the reference system is fixed in space and a mass element, together with its quantities, is observed in space. Field variables such as the velocity, the density and the pressure field are taken into account.
Since it would be complex to track all the particles individually, the balance equations will be written in the Eulerian formulation.

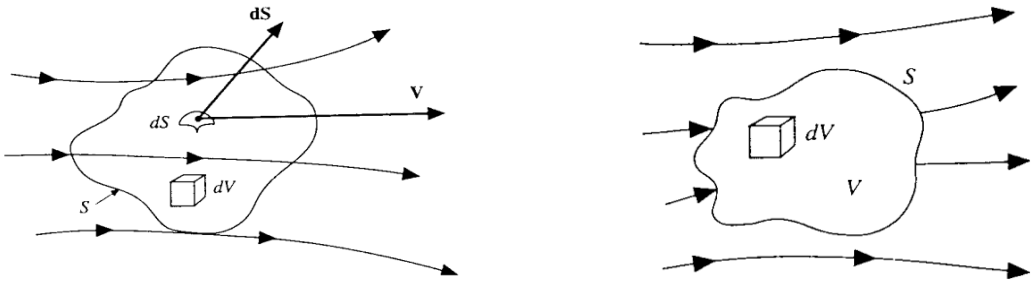

Figure 2.2: Eulerian (left) and Lagrangian (right) point of view [6]

2.2.1 Continuity equation

The continuity equation characterizes the mass balance on a fixed control volume in space.

$$\frac{d\rho}{dt} + \nabla \cdot (\rho \boldsymbol{u}) = 0, \tag{2.8}$$

where ρ represents the density, t the time and $\boldsymbol{u}$ the velocity vector.

2.2.2 Momentum equation

Conservation of momentum is achieved by applying Newton's second law on a moving fluid particle:

$$\frac{\partial(\rho \boldsymbol{u})}{\partial t} + \nabla \cdot (\rho \boldsymbol{u}\boldsymbol{u}) = \nabla \cdot \boldsymbol{\Pi} + \rho \boldsymbol{f}, \tag{2.9}$$

where $\boldsymbol{f}$ represents the external forces per unit volume and $\boldsymbol{\Pi}$ is the stress tensor, which is composed of an isotropic and an anisotropic component and its components in vectorial notation are σ_{ij}:

$$\boldsymbol{\Pi} = -\rho \boldsymbol{I} + \tau \rightarrow \sigma_{ij} = -p\delta_{ij} + \tau_{ij}, \tag{2.10}$$

where $\boldsymbol{I}$ is the identity matrix and δ_{ij} are its components.
The pressure p is the average value of the normal component of the stress tensor:

$$p = -\frac{1}{3}\sum_i \sigma_{ii}. \tag{2.11}$$

τ represents the viscous stress term, which in the case of Newtonian fluids is proportional to the shear stress:

$$\tau_{ij} = -\mu\left(\frac{\partial u_i}{\partial x_j} + \frac{\partial u_j}{\partial x_i}\right) + \frac{2}{3}\delta_{ij}\lambda\frac{\partial u_k}{dx_k}, \tag{2.12}$$

here λ represents the volume viscosity and, adopting the Stokes Hypothesis (which assumes that the mechanical pressure is equal to the thermodynamic pressure), takes the value $\lambda = -\frac{2}{3}\mu$ with μ being the dynamic viscosity.

2.2.3 Energy equation

The energy conservation equation is derived by multiplying the momentum equation by the velocity:

$$\frac{\partial(\rho E)}{\partial t} + \nabla(\rho E \boldsymbol{u}) = \nabla \cdot (\boldsymbol{\Pi} \cdot \boldsymbol{u}) - \nabla \cdot \boldsymbol{q} + \rho \boldsymbol{f} \cdot \boldsymbol{u}, \tag{2.13}$$

where E represents the total energy and is defined as $E = e + |u|^2/2$, with e being the internal energy defined as $e = c_v T$, where c_v is the specific heat capacity at constant volume; while $\boldsymbol{q}$ represents the heat flow which has been defined by Fourier's law as:

$$q_j = -\mathfrak{k}\left(\frac{\partial T}{\partial x_j}\right) = c_p \frac{\mu}{Pr}\left(\frac{\partial T}{\partial x_j}\right), \qquad (2.14)$$

with $\mathfrak{k} = -c_p \frac{\mu}{Pr}$ being the thermal conductivity of the material, c_p is the specific heat capacity at constant pressure and Pr is the Prandtl number.
Together, the three conservation equations make the Navier Stokes equations and govern all fluid dynamic phenomena.

2.2.4 Closing equations

To close the system, considering an ideal gas, the state equation of ideal gases can be written:

$$p = \rho R T. \qquad (2.15)$$

2.3 Acoustics Equations

In this section the basic equations of acoustics will be introduced. Specifically, the Wave equation is the equation that describes sound propagation.

2.3.1 Acoustic wave equation

In *Section 2.2.1* sound was defined as a small pressure perturbation. In the hypothesis that an acoustic wave propagates in the medium in an isentropic manner, the other quantities will also be small enough to allow the linearization of the equations.
From the equation of state for an isentropic flow, the relationship between density and pressure fluctuations can be obtained:

$$p' = \rho' c_o^2, \qquad (2.16) \qquad\qquad c_o^2 = \left(\frac{\partial p}{\partial \rho}\right)_s. \qquad (2.17)$$

To simplify the discussion, a homogeneous medium at rest is considered. With these hypotheses, the quantities that describe the propagation medium remain constant.
The quantities describing the fluid can be broken down into a temporal average contribution (identifiable by the angular brackets) and a fluctuation with respect to the average value (identifiable by the superscript):

$$\mathbf{u}(x,t) = \langle \mathbf{u} \rangle + \mathbf{u}'(x,t), \qquad (2.18.a)$$
$$\rho(x,t) = \langle \rho \rangle + \rho'(x,t), \qquad (2.18.b)$$
$$p(x,t) = \langle p \rangle + p'(x,t). \qquad (2.18.c)$$

As a further simplification, an inviscid medium will be considered. The so simplified Navier Stokes equations are called the Euler equation. By linearizing the Euler equations, equations (2.19) are obtained:

$$\frac{\partial \rho'}{\partial t} + \langle \rho \rangle \cdot \nabla \boldsymbol{u} = Q_{\mathrm{m}}, \qquad (2.19.a)$$

$$\langle \rho \rangle \frac{\partial u'}{\partial t} = -\nabla p' + \langle \rho \rangle \boldsymbol{f}_{\mathrm{m}}, \qquad (2.19.b)$$

$$\langle \rho \rangle \langle T \rangle \frac{\partial s'}{\partial t} = Q_{\mathrm{w}}. \qquad (2.19.c)$$

Q_{m} , $\boldsymbol{f}_{\mathrm{m}}$ e Q_{w} represent the acoustic source terms of mass, momentum, and energy.
To close the system, the caloric equation and the state equation are used:

$$dp' = c_0^2 \, d\rho' + \frac{\langle \rho \rangle}{c_v} ds, \qquad (2.20)$$

$$\frac{p'}{\langle p \rangle} = \frac{\rho'}{\langle \rho \rangle} + \frac{T'}{\langle T \rangle}. \qquad (2.21)$$

Combining all the equations together it is possible to obtain the wave equation:

$$\frac{1}{c_0^2} \frac{\partial^2 p'}{\partial t} - \nabla^2 p' = \frac{\partial}{\partial t} \left(Q_m + \frac{\gamma - 1}{2} Q_w \right) - \langle \rho \rangle \, \nabla \cdot \boldsymbol{f}_{\mathrm{m}}. \qquad (2.22)$$

2.4 Aeroacustics analogies

In *Section 2.3*, the linearized wave equation, capable of describing the generation of sound due to a disturbance resulting from a very specific movement of the source that produces it, was discussed.
In aeroacoustics, for example, taking into consideration the noise generated by a turbulent jet, very often there is neither a defined surface nor a precise movement of the same; therefore, the noise must be generated by another mechanism.
Turbulence noise is generated by the action of inertia and compressibility when turbulent structures are subject to rapid temporal variations.
When the turbulent structures are simply transported by the current, without there being any variations, then there is no emission of noise.
When the inertia of the motion varies suddenly, i.e. during the reorganization phase of the vortices, the corresponding variations in pressure and density generate acoustic emissions.
The main mechanisms that govern the phenomenon are:

- mutual induction between vortices: phenomenon mainly evident in regions of turbulent mixing where vortical structures collide and reassemble.
- interaction between vortices and the wall: where the geometric singularities have a characteristic length lower than the wavelength, noise is generated.

2.4.1 Green's functions formalism

The Green formalism can be used to obtain an integral solution of the wave equation when source terms are present.

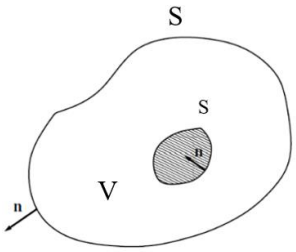

Figure 2.3: Green's formalism, reference volume V and surface S [5]

The Green kernel function G is the function which, associated with a linear differential operator $\mathfrak{L}$, produces the Dirac delta δ as a response:

$$\mathfrak{L}\big(G(\boldsymbol{x}-\boldsymbol{x}')\big)=\delta(\boldsymbol{x}-\boldsymbol{x}'), \tag{2.23}$$

where $\boldsymbol{x}-\boldsymbol{x}'$ is the position of the observer in respect to the source.
The Green's function G can therefore be defined as the solution of the inhomogeneous equation:

$$\frac{1}{c_0^2}\frac{\partial^2 G}{\partial t^2}-\frac{\partial^2 G}{\partial y_i^2}=\delta(\boldsymbol{x}-\boldsymbol{y})\delta(t-t). \tag{2.24}$$

The solution is of the type $G(\boldsymbol{x},t|\boldsymbol{y},t)$ where $\boldsymbol{x},t$ are defined with respect to the observer reference system and $\boldsymbol{y},t$ are defined with respect to the impulsive source that emits a sound impulse at time t called delayed time.

The Green's function has the following properties:

- Causality principle: $G=0$, $\frac{\partial G}{\partial t}=0$ for $t<t$ there cannot be a non-zero solution before the acoustic signal is issued.
- Reciprocity: $G(\boldsymbol{x},t|\boldsymbol{y},t)=G(\boldsymbol{y},-t|\boldsymbol{x},-t)$.
- Asymmetry: $\frac{\partial G}{\partial t}=-\frac{\partial G}{\partial t}$.

Considering the problem:

$$\frac{1}{c_0^2}\frac{\partial^2 p'}{\partial t^2}-\frac{\partial^2 p'}{\partial y_i^2}=q(\boldsymbol{y},t), \tag{2.25}$$

where p' is defined as:

$$p'(\boldsymbol{x},t)=\int_{t_0}^{t}\int_{V}p'(\boldsymbol{y},t)\delta(\boldsymbol{x}-\boldsymbol{y})\delta(t-t)d\boldsymbol{y}dt, \tag{2.26}$$

and where the Green's function in a free field, i.e. in the absence of walls, is defined as G_0:

$$G_0=\frac{1}{4\pi|\boldsymbol{x}-\boldsymbol{y}|}\delta\left(t-t-\frac{|\boldsymbol{x}-\boldsymbol{y}|}{c_0}\right), \tag{2.27}$$

After having carried out the appropriate mathematical steps, p' can be explained as a function of G:

$$p'(\boldsymbol{x},t) = \int_{t_0}^{t}\int_{V} q(\boldsymbol{y},\tau)G_0(\boldsymbol{x},t|\boldsymbol{y},\tau)d\boldsymbol{y}d\tau + \\ -\int_{t_0}^{t}\int_{S}\left(p'\frac{\partial G_0}{\partial y_i} - G_0\frac{\partial p'}{\partial y_i}\right)\boldsymbol{n}dSd\tau \qquad (2.28)$$

The first term describes the cumulative effect of the sources, the second takes into account the effect due to the diffusion of the walls.

2.4.2 Lighthill acoustic analogy

The Lighthill equation is an exact equation, it is not obtained from a linearization, but from a rearrangement of the terms of the Navier Stokes equation in order to get a wave equation for a homogeneous medium at rest or in uniform motion.
The aim is to obtain an approximate law that describes the acoustic generation of the current under examination, the flow must be known a priori.
Lighthill defines noise as the difference between the exact and approximate solutions.
Since the contribution of the turbulent terms would be lost due to linearization, the acoustic sources are described as a linear combination of simple fields (monopole, dipole and quadrupole).
Recombining the equations of fluid mechanics the Lighthill equation is obtained:

$$\frac{\partial^2\rho}{\partial t^2} - c_0^2\frac{\partial^2\rho}{\partial x_i^2}\delta_{ij} = \frac{\partial^2 T_{ij}}{\partial x_i \partial x_j}, \qquad (2.29)$$

where T_{ij} is the Lighthill Tensor and represents the source term that describes all noise generation phenomena, and has the form:

$$T_{ij} = \rho u_i u_j + (p' - c_0^2\rho')\delta_{ij} - \tau_{ij} \qquad (2.30)$$

The first term $\rho u_i u_j$ represents all the nonlinear convective forces described by the Reynolds stress tensor, $\Delta s = (p' - c_0^2\rho')$ represents an entropy source term, τ_{ij} are the viscous stresses. This term, which has a quadrupolar form, is still an exact solution of the equations of fluid mechanics.

To be noted that in the far field, which is the region, far from the source, where the wave front has become almost locally flat and there is no more interference from the near field:

- $c_0^2 \approx \frac{p}{\rho} \rightarrow \Delta s \approx 0$: there are no variations of entropy.
- $u_i u_j \approx 0$: oscillations are reduced to a minimum.
- $\tau_{ij} \approx 0$: outside the source the viscous effects are negligible.

It follows that, in the far field $T_{ij} \approx 0$.

Given the definition of Mach number as:

$$M = \frac{u}{c_0}, \qquad (2.31)$$

and the definition of Reynolds number as:

$$Re = \frac{\rho u L}{\mu}, \tag{2.32}$$

with L being the characteristic length of the studied phenomena. Lighthill observed that, at low Mach number the inertial effects dominate over the thermal ones and the flow can be considered incompressible; in addition, at high Reynolds number the viscous effects also lose importance. Consequently, with these simplifications, it is possible to introduce the Lighthill approximation:

$$T_{ij} \approx \rho_0 u_i u_j. \tag{2.33}$$

Sound generation due to the vortex component is the dominant mechanism.
T_{ij} is independent of the acoustic variables p', ρ', the turbulent current is decoupled from the acoustic oscillations.
Since, unlike the exact formulation, in the Lighthill approximation the variables p', ρ' no longer appear both on the right and on the left side of the equal sign, it is possible to apply Green's Formalism to solve the equation.

2.4.3 Curle acoustic analogy

Curle's formulation applies the Green's formalism to the Lighthill equation to consider the presence of solid bodies within the fluid.
The solution is an equation with the form:

$$\begin{aligned} \rho'(\boldsymbol{x},t) = \frac{1}{c_0^2}\int_{t_0}^{t}\int_{V}\frac{\partial^2 T_{ij}}{\partial y_i \partial y_j} G_0(\boldsymbol{x},t|\boldsymbol{y},\tau)d\boldsymbol{y}d\tau + \\ -\int_{t_0}^{t}\int_{S}\left(\rho'\frac{\partial G_0}{\partial y_i} - G_0\frac{\partial \rho'}{\partial y_i}\right)n_i dS d\tau. \end{aligned} \tag{2.34}$$

The wall S is considered both active, i.e. it generates noise by oscillating, and passive, i.e. it causes scattering. Note that the wall, being able to swing, can move.
Solving the integrals, with far field simplification, the Curle equation is obtained:

$$\begin{aligned} p'(\boldsymbol{x},t) = \frac{1}{4\pi c_0^2|\boldsymbol{x}|}\frac{x_i x_j}{|\boldsymbol{x}|^2}\frac{\partial^2}{\partial t^2}\int_V \left[T_{ij}\right]_{t^*} d\boldsymbol{y} \; + \\ -\frac{1}{4\pi|\boldsymbol{x}|}\frac{\partial}{\partial t}\int_S [\rho u_i n_i]_{t^*} dS + \\ -\frac{1}{4\pi c_0|\boldsymbol{x}|}\frac{x_j}{|\boldsymbol{x}|}\frac{\partial}{\partial t}\int_S \left[(\rho u_i u_j - \sigma_{ij})n_i\right]_{t^*} dS, \end{aligned} \tag{2.35}$$

where $t^* = \tau = t - \frac{|x|}{c_0}$ is the delayed time.
The solution has three terms:

- The first is a quadrupole term, which represents the noise generated by turbulent fluctuations and is proportional to Mach⁴.
- The second is a monopolar term, it is linked to the mass flow rate generated by the oscillations of the body itself. It is called Thickness noise, and it is proportional to Mach².

- The third term is a dipolar term, it represents the noise generated by the variation of aerodynamic forces. It is called Loading noise and is proportional to Mach³.

Since the acoustic intensity is directly proportional to the square of the pressure fluctuations, it is possible to obtain the intensity distribution as the Mach number varies for the different terms. It can be seen that at low Mach the most influential term is the monopolar one, while at high Mach the major contribution to the noise is given by turbulent fluctuations.

2.4.4 Ffowcs-Williams-Hawking acoustic analogy

The Ffowcs-Williams-Hawking (FWH) formulation is an alternative method for calculating the noise generated by a body immersed in a current, which takes into account the movement of the body.
The FWH theory aims to overcome the stationarity hypothesis of Curle's formulation. Solid bodies are replaced by an acoustic source immersed in an unlimited medium at rest.
Both the body and its possible fluctuations/oscillations must be contained within the source surrounded by the surface S, which must generate an effect equivalent to that of the body.
The sources are arbitrary and positioned on the surface S.
This is achieved through the use of heavyside functions, generalized functions whose derivative corresponds to the Dirac delta δ applied to the same function.

$$H(g) = \begin{cases} 0 \text{ if } g < 0 \text{ (inside } \sigma) \\ 1 \text{ if } g > 0 \text{ (outside } \sigma) \end{cases}$$

$$\frac{\partial H}{\partial g} = \delta(g). \qquad (2.36)$$

Inside the source the field, $H(g)$ is identically zero thanks to the Heavyside functions, outside, the approximate acoustic field is obtained.
At the surface $S,\ g = 0$ the source is not defined; this leads to the accumulation of the source terms on the surface.

This formalism is applied to the Navier Stokes equations, which are multiplied by $H(g)$, which when appropriately rearranged give rise to the FWH wave equations.

$$\frac{\partial^2[\rho' H(g)]}{\partial t^2} - c_0^2 \frac{\partial^2[\rho' H(g)]}{\partial x_i^2} = \\ = \frac{\partial}{\partial t}\big(Q_m \delta(g)\big) - \frac{\partial}{\partial x_i}\big(F_i \delta(g)\big) + \frac{\partial}{\partial x_i \partial x_j}\Big(T_{ij} \delta(g)\Big). \qquad (2.37)$$

This equation is solved through Green's formalism and the solution has the form:

$$p'(\boldsymbol{x}, t) = \frac{1}{4\pi c_0^2} \frac{x_i x_j}{r^3} \frac{\partial^2}{\partial t^2} \int_V \left[\frac{T_{ij}}{|1 - M_S \cos\theta|}\right]_{t^*} d\boldsymbol{y} + \\ + \frac{1}{4\pi r} \frac{\partial}{\partial t} \int_S \left[\frac{\big(\rho u_i + \rho(u_i - U_i)\big)}{|1 - M_S \cos\theta|}\right]_{t^*} n_i dS + \\ + \frac{1}{4\pi c_0} \frac{x_j}{r^2} \frac{\partial}{\partial t} \int_S \left[\frac{\big(\rho u_i (u_j - U_j) - \sigma_{ij}\big)}{|1 - M_S \cos\theta|}\right]_{t^*} n_j dS. \qquad (2.38)$$

In this equation, with θ being the angle between the observer's line of sight and the direction of motion of the noise source and M_S is the Mach number of the source, the term $|1 - M_S \cos\theta|$ accounts for the Doppler shift effect, a change in frequency and wavelength of a wave as observed by someone who is moving relative to the wave source.

Chapter 3: Numerical methods: CFD and CAA

This chapter is dedicated to Computational Aeroacoustics (CAA), a specialized branch of acoustics and Computational Fluid Dynamics (CFD) that plays a crucial role in the analysis and prediction of noise generated by aerodynamic flows.
CAA is a field that has seen significant advancements with the progression of computational capabilities. It involves the use of numerical methods and algorithms to solve and analyze problems that involve noise generation and propagation due to aerodynamic phenomena.
In the first part of this chapter, the fundamentals of CFD analysis will be discussed; after that an overview of the turbulence models, which are essential in order to perform a CAA simulation, will be performed; and finally, the focus will be shifted to the specific computational aeroacustics models.

3.1 Basic concepts of CFD

In this section, the main characteristics of Computational Fluid Dynamics will be introduced first and then the methodologies, that make it possible to use the formulas that model physical phenomena by the computer, will be described in more detail.
Computational fluid dynamics consists of the analysis of flows of various kinds using mathematical models. It is used in many engineering fields, such as aerodynamics, hydrodynamics and thermal engineering, to solve complex fluid-fluid or fluid-solid interaction problems [6].
A CFD numerical solver includes several components, the main ones are:

- Mathematical model: a set of differential or integro-differential equations that describes the physical phenomenon.
- Discretization methods: methods that can approximate the characteristic equations of the phenomenon to algebraic equations, in such a way that they can be used by the calculator. The most adopted discretization methods are finite differences, finite elements and finite volumes.
- Coordinate systems: typically, a CFD program allows to select several coordinate systems to suit most problems.
- Numerical grid or mesh: a subdivision of the domain into many elements of finite size called cells, to which the properties of the fluid are associated, and which can communicate with each other and exchange information.
- Finite approximation: after choosing the grid, generally the type of approximation to use for the discretization of the equations is chosen, generally a compromise choice must be made between speed to achieve convergence and accuracy of the solution.
- Solution method: the method with which the large nonlinear algebraic systems produced by discretization are solved.
- Convergence criteria: the type of criterion with which it is decided under which assumptions to stop the simulation.

It is important that the CFD solver has properties that allow it to obtain results that come as close as possible to reality, although the presence of errors due to approximation is unavoidable.
A numerical method is said to be stable if it does not amplify the errors that appear during the

numerical process. It is important that as the grid tends to zero the truncation error tends to zero, i.e. that the discretized equation tends to the exact solution as the grid thickens.

In the following sub-chapters, the methodologies of discretization of the equations in general will be addressed.

3.1.1 Finite differences

The idea of the finite difference method originates directly from the definition of derivative:

$$\left(\frac{\partial \varphi}{\partial x}\right)_{x_i} = \lim_{\Delta x \to 0} \frac{\varphi(x_i - \Delta x) - \varphi(x_i)}{\Delta x}. \qquad (3.1)$$

First, the geometric domain must be discretized, in finite differences the grid is generally structured.

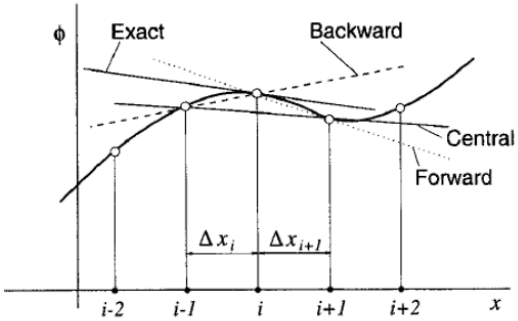

Figure 3.1: Differencing schemes [6]

It is possible to see from *Figure 3.1* how the slope of the curve can be approximated in three different ways:

- Backward difference: $\left(\frac{\partial \varphi}{\partial x}\right)_{x_i} = \frac{\varphi(x_i) - \varphi(x_{i-1})}{x_i - x_{i-1}} + O(\Delta x^1).$ (3.2.a)
- Forward difference: $\left(\frac{\partial \varphi}{\partial x}\right)_{x_i} = \frac{\varphi(x_{i+1}) - \varphi(x_i)}{x_{i+1} - x_i} + O(\Delta x^1).$ (3.2.b)
- Central difference: $\left(\frac{\partial \varphi}{\partial x}\right)_{x_i} = \frac{\varphi(x_{i+1}) - \varphi(x_{i-1})}{x_{i+1} - x_{i-1}} + O(\Delta x^2).$ (3.2.c)

The quality of the approximation depends on the spacing of the grid points and the type of approximation used.

3.1.2 Finite volumes

The finite volume method uses the integral form of the equations as a starting point.
Typically, the physical domain is discretized into volumetric cells which have a central node.

Approximation of surface integrals

The net flux through the control volume is the sum of the surface integrals enclosing the same volume:

$$\int_S \mathfrak{f} dS = \sum_k \int_{S_k} \mathfrak{f} dS_k, \qquad (3.3)$$

where ƒ represents the normal component with respect to the k-th surface, of an arbitrary control volume.
The simplest approximation that can be implemented involves approximating the value of the flux on the surfaces, with the average value at the center of the surface.
For example, considering the surface "e" it is possible to write:

$$\int_{S_e} \mathrm{f} dS_e = \bar{\mathrm{f}}_e S_e \approx \mathrm{f}_e S_e. \quad (3.4)$$

This last approximation is accurate to the second order.
Alternatively, the trapezoid rule (2nd order accuracy) shown in (3.5) or the Simpson's theorem (4th order accuracy) shown in (3.6) could be exploited:

$$\int_{S_e} \mathrm{f} dS_e \approx \frac{1}{2}(\mathrm{f}_{ne} - \mathrm{f}_{se}) S_e, \quad (3.5)$$

$$\int_{S_e} \mathrm{f} dS_e \approx \frac{1}{6}(\mathrm{f}_{ne} + 4\mathrm{f}_e + \mathrm{f}_{se}) S_e. \quad (3.6)$$

3.1.3 Upwind methods

Upwind methods exploit the direction of propagation of quantities and signals to choose the type of scheme to adopt. In the following chapter the general method for solving the Navier Stokes equations using upwind methods is shown.
To simplify the discussion, Euler's equations are used, which are rewritten in the form of a conservation law:

$$\frac{\partial}{\partial t}\int_V \boldsymbol{W} dV + \int_S \boldsymbol{F_c} \boldsymbol{n} dS = \frac{\partial}{\partial t}\int_V \boldsymbol{W} dV + \int_V \nabla \boldsymbol{F_c} dV = 0, \quad (3.7)$$

where $\boldsymbol{W}$ composes the vector of conservative variables and $\boldsymbol{F_c}$ composes the vector containing the convective fluxes:

$$\boldsymbol{W} = \{\rho, \rho u_i, \rho u_j, \rho u_k, E\}^T, \quad (3.8)$$

$$\boldsymbol{F_c} = \{\rho \boldsymbol{u}, p + \rho u_i \boldsymbol{u}, p + \rho u_j \boldsymbol{u}, p + \rho u_k \boldsymbol{u}, (E + p)\boldsymbol{u}\}^T. \quad (3.9)$$

Rewriting the equation in conservative form and noting that $\boldsymbol{F_c} = \boldsymbol{F_c}(\boldsymbol{W})$, it follows that:

$$\frac{\partial \boldsymbol{W}}{\partial t} + \frac{\partial \boldsymbol{F_c}}{\partial x} = \frac{\partial \boldsymbol{W}}{\partial t} + \frac{\partial \boldsymbol{F_c}}{\partial \boldsymbol{W}}\frac{\partial \boldsymbol{W}}{\partial x} = \frac{\partial \boldsymbol{W}}{\partial t} + \boldsymbol{A}\frac{\partial \boldsymbol{W}}{\partial x} = \boldsymbol{W}_t + \boldsymbol{A}\boldsymbol{W}_x = 0, \quad (3.10)$$

where $\frac{\partial \boldsymbol{F}}{\partial \boldsymbol{W}} = [\boldsymbol{A}]$ is a Jacobian matrix and a new notation for the derivatives is used.
The Euler equation written in integral form by introducing the 1D flow hypothesis is:

$$\frac{\partial}{\partial t}\int_{x_{N-\frac{1}{2}}}^{x_{N+\frac{1}{2}}} W dx + \mathrm{f}\left(W_{N+\frac{1}{2}}\right) - \mathrm{f}\left(W_{N-\frac{1}{2}}\right) = 0. \quad (3.11)$$

Integrating (3.11) over time and dividing by Δx, eq (3.12) is obtained:

$$\frac{1}{\Delta x}\int_{x_{N-\frac{1}{2}}}^{x_{N+\frac{1}{2}}} W(x,t+\Delta t)dx - \frac{1}{\Delta x}\int_{x_{N-\frac{1}{2}}}^{x_{N+\frac{1}{2}}} W(x,t)dx + \frac{1}{\Delta x}\int_{t}^{t+\Delta t} \mathfrak{f}\left(W\left(x_{N+\frac{1}{2}},t\right)\right)dt + \\ -\frac{1}{\Delta x}\int_{t}^{t+\Delta t} \mathfrak{f}\left(W\left(x_{N-\frac{1}{2}},t\right)\right)dt = 0 \qquad (3.12)$$

Writing is made easier by introducing the variables:

$$W_N^k = \frac{1}{\Delta x}\int_{x_{N-\frac{1}{2}}}^{x_{N+\frac{1}{2}}} W(x,t+\Delta t)dx, \qquad (3.13)$$

$$\mathfrak{f}_{N+\frac{1}{2}}^k = \frac{1}{\Delta t}\int_{t^k}^{t^{k+1}} \mathfrak{f}\left(W\left(x_{N+\frac{1}{2}},t\right)\right)dt. \qquad (3.14)$$

The 1D Euler equation can be rewritten, after being discretized, as:

$$W_N^{k+1} = W_N^k - \frac{\Delta t}{\Delta x}\left(\mathfrak{f}_{N+\frac{1}{2}}^k - \mathfrak{f}_{N-\frac{1}{2}}^k\right). \qquad (3.15)$$

In this example, an explicit scheme for temporal integration was adopted.
The goal of the upwind method is to calculate the flows at the interfaces.

Courant–Friedrichs–Lewy Condition

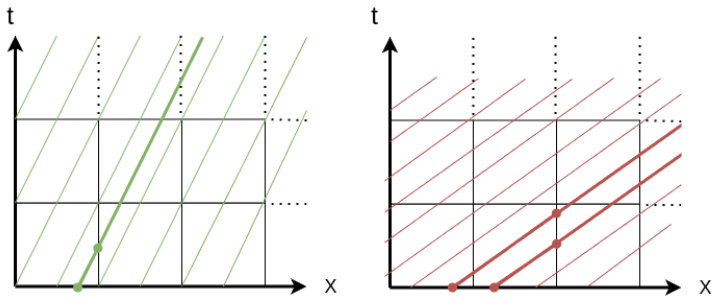

Figure 3.2: Signal propagation

In a space-time graph $\bar{a}$ represents the slope of the $W(x,t)$ curves.
From *Figure 3.2* it can be seen that, if the constraint is not respected: $\Delta t < \frac{\Delta x}{|\bar{a}|}$, in the end, more than one signal will arrive at a time and this condition would create instability and oscillations which could result in the divergence of the solution.
The Courant–Friedrichs–Lewy (CFL) condition is a criterion which, applied to explicit methods, guarantees the stability of the numerical method.

$$CFL = \frac{\Delta t}{\Delta x}|\bar{a}| < 1 \qquad (3.16)$$

Implicit methods are less prone to instability so a value of $CFL > 1$ is acceptable.

Finite differences approach

Imagining having a signal that moves at a speed $\bar{a} > 0$, considering keeping the value of W constant within a cell.
A geometric approach is implemented to calculate the signal at a later instant:
let $W_N^{k+1} = W(x_N, t^{k+1}) = W(x_N - \bar{a}\Delta t, t^k)$ it is possible to linearly interpolate the spatial value at a point x as:

$$\begin{aligned} W_N^{k+1} &= W(x_N - \bar{a}\Delta t, t^k) = \\ &= W_{N-1}^k + \frac{W_N^k - W_{N-1}^k}{\Delta x}(x_N - \bar{a}\Delta t - x_{N-1}) = \\ &= W_{N-1}^k + \frac{W_N^k - W_{N-1}^k}{\Delta x}(\Delta x - \bar{a}\Delta t) = \\ &= W_N^k - \frac{\bar{a}\Delta t}{\Delta x}\left(W_N^k - W_{N-1}^k\right) \end{aligned} \qquad (3.17)$$

$$W_N^{k+1} = W_N^k - \frac{\bar{a}\Delta t}{\Delta x}\left(W_N^k - W_{N-1}^k\right). \qquad (3.18)$$

Finite volumes approach

Considering the same signal as above but in a finite volume approach:
Starting from the definition of W_N^{k+1}:

$$W_N^{k+1} = \frac{1}{\Delta x}\int_{x_{N-\frac{1}{2}}}^{x_{N+\frac{1}{2}}} W(x, t^{k+1})dx, \qquad (3.19)$$

the integral is discretized as follows:

$$\begin{aligned} W_N^{k+1} &= \frac{1}{\Delta x}\left[W_{N-1}^k \bar{a}\Delta t + W_N^k(\Delta x - \bar{a}\Delta t)\right] = \\ &= W_N^k - \frac{\bar{a}\Delta t}{\Delta x}\left(W_N^k - W_{N-1}^k\right). \end{aligned} \qquad (3.20)$$

Wave propagation approach

Considering the signal at two successive instants, it is possible to define the jump quantities:

$$\Delta W_{N-\frac{1}{2}} = W_N - W_{N-1}, \qquad (3.21.a)$$

$$\Delta W_{N+\frac{1}{2}} = W_{N+1} - W_N. \qquad (3.21.b)$$

The jump penetrates each cell, altering its solution.

$$\bar{a} > 0: \; W_N^{k+1} = W_N^k - \frac{\bar{a}\Delta t}{\Delta x}\Delta W_{N-\frac{1}{2}} = W_N^k - \frac{\bar{a}\Delta t}{\Delta x}\left(W_N^k - W_{N-1}^k\right), \qquad (3.22.a)$$

$$\bar{a} > 0: \; W_N^{k+1} = W_N^k - \frac{\bar{a}\Delta t}{\Delta x}\Delta W_{N+\frac{1}{2}} = W_N^k - \frac{\bar{a}\Delta t}{\Delta x}\left(W_{N+1}^k - W_N^k\right). \qquad (3.22.b)$$

Upwind: general form

Considering the scalar equation $W_t + \bar{a}W_x = 0$, with $\mathfrak{f} = \bar{a}W$ e $\mathfrak{f}_x = \bar{a}W_x$, it follows that:

$$\begin{cases} \mathfrak{f}_{N+\frac{1}{2}} = \bar{a}W_N \\ \mathfrak{f}_{N-\frac{1}{2}} = \bar{a}W_{N-1} \end{cases} \text{ if } \bar{a} > 0 \quad \text{and} \quad \begin{cases} \mathfrak{f}_{N+\frac{1}{2}} = \bar{a}W_{N+1} \\ \mathfrak{f}_{N-\frac{1}{2}} = \bar{a}W_N \end{cases} \text{ if } \bar{a} < 0$$

$$\begin{cases} \mathfrak{f}_{N+\frac{1}{2}} = a^+W_N + a^-W_{N+1} \\ \mathfrak{f}_{N-\frac{1}{2}} = a^+W_{N-1} + a^-W_N \end{cases} \quad (3.23)$$

In general, it is possible to write the upwind equations as:

$$W_N^{k+1} = W_N^k - \frac{\Delta t}{\Delta x}\left(a^+\Delta W^k_{N-\frac{1}{2}} + a^-\Delta W^k_{N+\frac{1}{2}}\right). \quad (3.24)$$

Where $a^+ = \max(\bar{a}, 0)$ if $a > 0$ and $a^- = \min(\bar{a}, 0)$ if $a < 0$.
This way of writing the equations can be extended to Euler as long as the quantities inside the bracket are seen as unique entities representing signals which, upon entering the cell, involve jumps in flow. Therefore, it is possible to write:

$$W_N^{k+1} = W_N^k - \frac{\Delta t}{\Delta x}\left(A^+\Delta W^k_{N-\frac{1}{2}} + A^-\Delta W^k_{N+\frac{1}{2}}\right). \quad (3.25)$$

Godunov's method

The methods that are based on the concept seen above all originate from the Godunov method, also called Reconstruct-Evolution-Averaging (REA) algorithm.
These methods are based on three steps:

- Reconstruct: the solution is reconstructed using piecewise constant functions or with higher order polynomials
- Evolution: the evolution of the solution over time is studied. A possible method consists in solving the Riemann problem, which corresponds to following the evolution of an initial discontinuity, generally originating at the interface between one cell and another precisely from the process of reconstructing the solution, with the aim of obtaining the flows to the interfaces.
- Averaging: the solution which, after the temporal evolution, will most likely have assumed a non-constant distribution within the cell, is then averaged to obtain the cell value.

3.2 Turbulence models

In nature, a fluid can occur in a laminar or turbulent regime. Most phenomena in nature are characterized by the presence of turbulence.

Following, after a general introduction to the physical phenomena that govern the motion of turbulent flows, the most commonly used models for modeling this phenomenon will be analyzed. The statements in the following chapters are mostly found in [7].

3.2.1 Turbulence's properties

Turbulence is characterized by several properties:

- It is a random process: turbulent flows are characterized by time- and space-dependent characteristics with many degrees of freedom. Turbulence cannot be reproduced in detail, but its statistics can be reproduced.
- Contains a large number of scales: by visualizing the flow and the velocity distribution within it, it is possible to see how there is a continuum between different spatial and temporal scales. The dynamics of turbulence involves all scales, from the smallest to the largest. The small scales live inside the larger ones.
- Increases with Reynolds number: the transition to turbulence occurs above the critical Reynolds number. At high Reynolds numbers, the continuous process of smaller scales being produced by larger ones goes on incessantly.
- Energy dissipation: the process that governs turbulence is the energy cascade, i.e. the transfer of energy from larger to smaller scales. Large scales contain most of the turbulent kinetic energy, small scales dissipate due to viscosity.
- The continuum hypothesis applies: the size of the small scales is determined by the viscosity. But even at high Reynolds numbers, this dimension is still greater than the molecular mean free path, making the phenomenon describable under the continuum hypothesis.
- It is an intrinsically three-dimensional phenomenon: if a two-dimensional fluid is considered, the vorticity would be directed in a direction orthogonal to the plane and the vortex stretching phenomenon could not occur. Without this phenomenon, the inertial cascade could not occur and therefore, there would be no onset of turbulence.
- Turbulence is a highly diffusive phenomenon: the swirling motion of the eddy causes the transport of mass, momentum and energy. Consequently, in a turbulent regime, wall stress, energy dissipation, thermal transport and mass transport are significantly increased.

3.2.2 The energy cascade

In this section, the main phenomenon that governs turbulent flows will be analyzed: the energy cascade.
By eddy, it's called a region, within a turbulent flow, characterized by moderate coherence and an identifiable dimension. Larger eddies are characterized by a size L directly linked to the size of the environment in which the flow evolves. These vortices are characterized by high Reynolds numbers, the effect of viscosity is almost zero, inertial effects prevail; furthermore, they are unstable and have a tendency to break into smaller structures, to which they transfer energy. This process continues until the Reynolds number makes the motion of the structure stable and the viscosity begins to dissipate energy. The smallest scale physically possible is called the Kolmogorov scale, of dimension η, it is where dissipation converts all the energy into heat, consequently smaller structures cannot exist. The size of these structures is directly linked to viscosity.

In CAA, the resolution of turbulence through the use of high-resolution models is of primary importance. The most used models will be described below:

3.2.3 Direct Numerical Simulation

The Navier Stokes equations are solved up to and including the smallest scales. With the exception of approximations due to discretization, the result of a Direct Numerical Simulation (DNS) can be considered exact. The computational cost is very high and depends on the wanted resolution. The fluid dynamic domain must contain the larger structures, while the smaller cells must be able to resolve the Kolmogorov scale. The time step is constrained by the Courant number, generally assumed to be equal to 1/20. The computational cost grows approximately with the Reynolds number: Re_λ^6 or Re_L^3 (where λ refers to the local Reynolds number applied to the Kolmogorov scale, while L refers to the Integral scale). Precisely because of the computational cost, the DNS approach was not applicable until the 1970s and for most applications it is also not usable today.

3.2.4 Large Eddy Simulation

In every turbulent flow, provided that the Reynolds number is sufficiently high, a universal shape can be associated with the statistics of small scales.
The Large Eddy Simulation (LES) approach involves the separation of large scales from small ones through the use of a spatial filter; at this point the former are solved by the calculator while the latter are described by a model. The filtering operations consists in applying to every fluid-dynamic field, the convolution:

$$\widehat{\mathcal{X}}(\boldsymbol{x},t) = \int \mathcal{G}(\boldsymbol{r},\boldsymbol{x})\mathcal{X}(\boldsymbol{x}-\boldsymbol{r},t)d\boldsymbol{r}, \qquad (3.26)$$

where $\mathcal{X}$ indicates the generic field-variable. Which corresponds to taking an average over a region of size Δ around the point $\boldsymbol{x}$ considered.
This operation separates the velocity into two contributions:

$$u_i(\boldsymbol{x},t) = \widehat{U}_i(\boldsymbol{x},t) + u_i''(\boldsymbol{x},t), \qquad (3.27)$$

$\widehat{U}_i$ is called the filtered speed and is the component resolved by the CFD solver and u_i'' is called the Subgrid-Scale (SGS) component.
Note: This formulation differs from the Reynolds decomposition (see *Chapter 3.2.5*) infact $\widehat{U}_i$ does not represent the average velocity and u_i'' is not necessarily zero on average.
The filter $\mathcal{G}$ with size Δ cleans the solution from all floating components smaller than the dimension of the filter itself. From the Navier Stokes equations, considering for simplicity the incompressible case (3.28):

$$\frac{\partial u_i}{\partial x_i} = 0 \qquad (3.28.a)$$

$$\frac{\partial u_i}{\partial t} + u_i\frac{\partial u_i}{\partial x_j} = -\frac{1}{\rho}\frac{\partial p}{\partial x_i} + \nu\frac{\partial^2 u_i}{\partial x_i \partial x_j} \qquad (3.28.b)$$

by applying the filter to (3.28), equations (3.29) are obtained:

$$\frac{\partial \widehat{U}_i}{\partial x_i} = 0, \qquad \frac{\partial u''_i}{\partial x_i} = 0 \tag{3.29.a}$$

$$\frac{\partial \widehat{U}_i}{\partial t} + \frac{\partial \widehat{u_i u_j}}{\partial x_j} = -\frac{1}{\rho}\frac{\partial \widehat{P}}{\partial x_i} + \nu \frac{\partial^2 \widehat{U}_i}{\partial x_i \partial x_j} \tag{3.29.b}$$

where the product $\widehat{u_i u_j} = \tau_{ij} + \widehat{U_i U_j}$ contains both the contributions of the filtered and modeled velocities.
The anisotropic residual stress tensor is defined as:

$$\tau_{ij}^{\mathrm{an}} \equiv \tau_{ij} - \frac{1}{3}\tau_{ij}\delta_{ij}. \tag{3.30}$$

Substituting into the equation for the moment it is possible to obtain:

$$\frac{\partial \widehat{U}_i}{\partial t} + \widehat{U}_j \frac{\partial \widehat{U}_i}{\partial x_j} = -\frac{1}{\rho}\frac{\partial \widehat{P}_*}{\partial x_i} - \frac{\partial \tau_{ij}^{\mathrm{an}}}{\partial x_j} + \nu \frac{\partial^2 \widehat{U}_i}{\partial x_i \partial x_j}. \tag{3.31}$$

The isotropic residual stress was included in the pressure $\widehat{P}_* = \hat{P} = \frac{1}{3}\rho\tau_{ij}\delta_{ij}$.
The closure of the equations is obtained by modeling the tensor $\tau_{ij}^{\mathrm{an}}(\boldsymbol{x}, t)$.
The most commonly used models for closing subgrid equations are those that are based on filtered field variables:

$$\tau_{ij}^{\mathrm{an}} = -2\nu_{\mathrm{LES}}\hat{\mathcal{S}}_{ij}, \tag{3.32}$$

$$\hat{\mathcal{S}}_{ij} \equiv \frac{1}{2}\left(\frac{\partial \widehat{U}_i}{\partial x_j} + \frac{\partial \widehat{U}_j}{\partial x_i}\right), \tag{3.33}$$

where $\hat{\mathcal{S}}_{ij}$ represents the filtered rate of strain tensor. The turbulence modeling takes place on the term $\nu_{\mathrm{LES}}(\boldsymbol{x}, t)$ called Eddy viscosity.
For high Reynolds numbers the eddy viscosity can be modeled through the Smagorinsky model [8]:

$$\nu_{\mathrm{LES}} = l_s^2\, \hat{\mathcal{S}}_{ij}, \tag{3.34}$$

$$\hat{\mathcal{S}}_{ij} = \left(2\hat{\mathcal{S}}_{ij}\hat{\mathcal{S}}_{ij}\right)^{1/2}, \tag{3.35}$$

where l_{S} represents the Smagorisky length scale and is proportional to the length of the filter $l_{\mathrm{S}} = C_{\mathrm{S}}\Delta$ (where C_{S} is the Smagorimky coefficient and depends on the type of flow under consideration). By specifying l_{S} the Δ operator does not appear in any equation.
The negative aspects that emerge from adopting the Smagorinsky model are various:

- A single value of C_{S} is often insufficient to describe different flows or evolving flows.
- Subgrid-stresses do not vanish at solid surfaces, therefore, near-wall damping functions are required.
- Smagorinsky's model does not take into account backscatter, i.e. the phenomenon of re-transfer of energy from small to large scales.
- Near the wall, the anisotropy of small scales is not considered.
- Even for large density variations or in the case of rotating flow, the Smagorinsky model must be modified.

To overcome the limits of the Smagorinsky model, a collaboration between Professors Germano, Pionelli, Moin and Cabot proposed the use of a coefficient $C_S = C_S(x, y, z, t)$ which changes value dynamically based on the local structure of the flow.

WALE subgrid scale model

The Wall-Adapting Local-Eddy Viscosity (WALE) subgrid scale model is a more modern subgrid scale model that uses a novel form of the velocity gradient tensor in its formulation.
It provides the following mixing-length type formula for the subgrid scale viscosity:

$$\mu_{\mathrm{WALE}} = \rho \Delta^2 \mathcal{S}_w, \tag{3.36}$$

where ρ is the density, Δ is the length scale or grid filter width, and $\mathcal{S}_w$ is the deformation parameter. The length scale is defined in terms of volume as:

$$\Delta = \min\left(\kappa, C_w V^{\frac{1}{3}}\right), \tag{3.37}$$

here C_w is a model coefficient and κ is the von Karman constant.
The deformation parameter S_w is defined as:

$$\mathcal{S}_w = \frac{\boldsymbol{\mathcal{S}}_d : \boldsymbol{\mathcal{S}}_d^{\frac{3}{2}}}{\boldsymbol{\mathcal{S}}_d : \boldsymbol{\mathcal{S}}_d^{\frac{5}{4}} + \overline{\boldsymbol{\mathcal{S}}} : \boldsymbol{\mathcal{S}}_d^{\frac{5}{2}}}, \tag{3.38}$$

where the tensor $\boldsymbol{\mathcal{S}}_d$ is computed from the resolved velocity field:

$$\boldsymbol{\mathcal{S}}_d = \frac{1}{2}[\nabla \boldsymbol{u} \cdot \nabla \boldsymbol{u} + (\nabla \boldsymbol{u} \cdot \nabla \boldsymbol{u})^T] - \frac{1}{3} tr(\nabla \boldsymbol{u} \cdot \nabla \boldsymbol{u}) \boldsymbol{I} \tag{3.39}$$

And $\overline{\boldsymbol{\mathcal{S}}}$ is the mean strain rate sensor given by: $\overline{\boldsymbol{\mathcal{S}}} = 1/2(\nabla \overline{\boldsymbol{u}} + \nabla \overline{\boldsymbol{u}}^T)$ [9].

CSM subgrid scale model

The coherent structure model (CSM) [10] developed by Kobayashi, calculated the subgrid viscosity as follows:

$$\nu_{\mathrm{CSM}} = F_{\mathrm{CSM}} \Delta^2 \left|\tilde{S}\right|, \tag{3.40}$$

where Δ is the local filter width calculated as $\Delta = \mathrm{V}^{1/3}$, with V being the volume of the cell; the function F_{CSM} is calculated from the resolved quantities as follows:

$$\mathrm{F_{CSM}} = \frac{1}{22} \left|\mathrm{F_{CSM,CS}}\right|^{\frac{3}{2}} \mathrm{F_{CSM,\Omega}}, \tag{3.41}$$

where:

$$F_{CSM,CS} = -\frac{\frac{1}{2}\frac{\partial \tilde{u}_i}{\partial x_i}\frac{\partial \tilde{u}_j}{\partial x_j}}{\left(\frac{1}{2}\frac{\partial \tilde{u}_j}{\partial x_j}\right)^2}, \quad (3.42)$$

$$F_{CSM,\Omega} = 1 - F_{CSM,CS}. \quad (3.43)$$

Based on the SGS viscosity the turbulence kinetic energy $\hbar_{SGS}$ and the turbulence dissipation rate ε_{SGS} associated with the unresolved SGS-scale motion can be estimated as:

$$\hbar_{SGS} = \frac{\nu_{CSM}|\tilde{S}|}{\sqrt{C_{SGS,\mu}}}, \quad (3.44)$$

$$\varepsilon_{SGS} = \nu_{CSM}|\tilde{S}|^2, \quad (3.45)$$

where $C_{SGS,\mu}$ is a constant and $|\tilde{S}| = \sqrt{2\tilde{S}_{ij}\tilde{S}_{ij}}$.

3.2.5 Reynold Average Navier Stokes Methods

Following the approach of decomposing the velocity and pressure into a mean and a fluctuating component $u_i = \langle u_i \rangle + u_i'$, $p_i = \langle p_i \rangle + p_i'$, proposed by Reynolds [11], the Navier Stokes equations for the mean field are rewritten as follows:

$$\frac{\partial \langle u_i \rangle}{\partial x_i} = 0\,, \qquad \frac{\partial u_i'}{\partial x_i} = 0, \qquad \left(\frac{\partial u_i'}{\partial t} = 0\right), \quad (3.46)$$

$$\frac{\partial \langle u_i \rangle}{\partial t} + \langle u_j \rangle \frac{\partial \langle u_i \rangle}{\partial x_j} = -\frac{1}{\rho}\frac{\partial \langle p_i \rangle}{\partial x_i} + \nu \frac{\partial^2 \langle u_i \rangle}{\partial x_i \partial x_j} - \frac{\partial \langle u_i u_j \rangle}{\partial x_j}. \quad (3.47)$$

The Reynolds stress tensor represents an average flow of momentum due to turbulent fluctuations.
The closure of the system occurs by modeling the Reynolds stress tensor; there are various ways to model turbulence, the most used are:

<u>*Turbulent viscosity hypothesis:*</u>

This approach, proposed by Boussinesq in 1877 [12], involves, similarly to the approach adopted by Smagorinsky *in Section 3.2.4*, the modeling of the eddy viscosity ν_{turb}.

$$-\rho\langle u_i' u_j' \rangle + \frac{2}{3}\rho\hbar\delta_{ij} \equiv -\rho \cdot a_{ij} = \rho\nu_{turb}\left(\frac{\partial \langle u_i \rangle}{\partial x_j} + \frac{\partial \langle u_j \rangle}{\partial x_i}\right) \equiv 2\rho\nu_{turb}\bar{S}_{ij} \quad (3.48)$$

In (3.48) $\hbar$ represents the mean turbulent kinetic energy per mass unit, a_{ij} is the anisotropic tensor.
This model presents the strong hypothesis that the tensor a_{ij} is aligned with the mean rate of strain tensor $\bar{S}_{ij}$. Specifically, TVH produces less precise results in the case of highly vortical flows, flows with accentuated curvatures and complex flows in general.

It is advisable to use this model for simple flows with small gradients and variations.

Mixing length model:

Having adopted the turbulent viscosity hypothesis, it is necessary to find an expression for the eddy viscosity:

$$\nu_T = l_m^2\left(2\,\bar{S}_{ij}\bar{S}_{ij}\right)^{1/2} \equiv l_m^2\bar{S} \qquad \text{Smagorinsky, 1963} \qquad (3.49.a)$$

$$\nu_T = l_m^2\left(2\,\bar{\Omega}_{ij}\bar{\Omega}_{ij}\right)^{1/2} \equiv l_m^2\bar{\Omega} \qquad \text{Baldwin and Lomax, 1978} \qquad (2.49.b)$$

l_m represents the mixing length. Smagorinsky's approach is the same as what was seen in *Section 3.2.4* for the LES turbulence model, but as regards Baldwin and Lomax, $\bar{\Omega}_{ij} = \frac{1}{2}\left(\frac{\partial\langle u_i\rangle}{\partial x_j} + \frac{\partial\langle u_j\rangle}{\partial x_i}\right)$ represents the mean rate of rotation.
The disadvantage of the mixing length model is that $l_m(x, y, z)$ must be specified throughout the whole domain; therefore, the flow must be known to expect accurate results.

Turbulent kinetic energy model (one equation):

In analogy to the kinetic theory of gases, where the kinematic viscosity is written as the product of a velocity and a length, turbulent viscosity is modeled in the same way:

$$\nu_{\text{turb}}(\boldsymbol{x}, t) = u^*(\boldsymbol{x}, t)\cdot l^*(\boldsymbol{x}, t). \qquad (3.50)$$

In the case of a single equation model, $l^* = l_m$ and $u^* = C\mathcal{k}^{1/2}$ are assumed, where C is a constant and $\mathcal{k}$ represents the turbulent kinetic energy.
Kolmogorov and Prandtl suggested deriving $\mathcal{k}$ by solving a transport equation for turbulent kinetic energy:

$$\frac{\partial\mathcal{k}}{\partial t} + \langle u_i\rangle\frac{\partial\mathcal{k}}{\partial x_i} = \Pi - \varepsilon - \frac{\partial I_{\text{i}}}{\partial x_i}, \qquad (3.51)$$

in this equation Π represents a turbulent kinetic energy production term, ε represents a dissipative term, and I_{i} is modeled as a diffusive term.

$$\Pi = -\overline{u_i'u_j'}\frac{\partial U_i}{\partial x_j}, \qquad \varepsilon = C_D\frac{\mathcal{k}^{\frac{3}{2}}}{l_m}, \qquad I_{\text{i}} = -\frac{\nu_{\text{turb}}}{\sigma_{\mathcal{k}}}\frac{\partial\mathcal{k}}{\partial x_i}.$$

This model allows the resolution of multiple flows as long as l_m is known, it also allows a fair amount of adaptability thanks to the possibility of changing multiple parameters.

$\mathcal{k} - \varepsilon$ model (two equations):

It is one of the most used turbulence models, it is not required to specify l_m. The approach is the same as the previous case, however in this case the reference variables are slightly different: $u^* = \mathcal{k}^{1/2}$ and $l^* = \mathcal{k}^{3/2}/\varepsilon$. It follows that: $\nu_{\text{turb}} = C_\mu\frac{\mathcal{k}^2}{\varepsilon}$
Furthermore, unlike the previous model, in which ε was resolved exactly, the resolution of an empirical equation is chosen:

$$\frac{\partial \varepsilon}{\partial t} + \langle u_i \rangle \frac{\partial \varepsilon}{\partial x_i} = C_{\varepsilon 1} \frac{\varepsilon}{k} \Pi - C_{\varepsilon 2} \frac{\varepsilon^2}{k} + \frac{\partial}{\partial x_i} \left(\frac{\nu_{\text{turb}}}{\sigma_\varepsilon} \frac{\partial \varepsilon}{\partial x_i} \right), \quad (3.52)$$

in this case it is possible to act on 5 constants: C_μ, $C_{\varepsilon 1}$, $C_{\varepsilon 2}$, σ_ε, σ_k.
The $k - \varepsilon$ model has been adopted for a wide range of applications with satisfactory results. The accuracy is acceptable for simple flows, it becomes less precise for complex flows such as in the case of separation, high vorticity, recirculation zones and flows at low Reynolds numbers. Close to the wall it is necessary to make some changes. Thanks to the presence of multiple parameters, it can be adopted to describe a wide range of flows.
Finally, from a computational point of view, it is not very expensive especially when used together with wall treatments.

$k - \omega$ model:

The $k - \omega$ turbulence model is a two-equation model that solves transport equations for the turbulent kinetic energy k and the specific dissipation rate ω, which corresponds to the dissipation rate per unit of turbulent kinetic energy ($\omega \propto \varepsilon / k$), in order to determine the turbulent eddy viscosity [9].
The $k - \omega$ model is often favored over the $k - \varepsilon$ model due to its enhanced capabilities in handling boundary layers under adverse pressure gradients. A key benefit of the $k - \omega$ model is its applicability across the entire boundary layer, including the region dominated by viscosity, without needing any additional modifications. Moreover, the standard $k - \omega$ model can operate without the need to compute wall distance.
However, the $k - \omega$ model is not without its drawbacks. In its original form, the model's computations for boundary layers are highly sensitive to the values of in the free-stream. This results in a high degree of sensitivity to inlet boundary conditions for internal flows, an issue that is not present in the $k - \varepsilon$ models. To mitigate this issue, the variants of the $k - \omega$ model included in Star-ccm+ and other commercial software, have undergone modifications.
The eddy viscosity $\nu_{\text{turb}} = \mu_{\text{turb}} / \rho$, as needed in the RANS equations, is given by:
$\nu_{\text{turb}} = k / \omega$, while the evolution of k and ω is modelled as:

$$\frac{\partial (\rho k)}{\partial t} + \frac{\partial (\rho \langle u_i \rangle k)}{\partial x_i} = \frac{\partial}{\partial x_j} \left[\left(\mu + \frac{\mu_{\text{turb}}}{\sigma_k} \right) \frac{\partial k}{\partial x_j} \right] + P_k + P_b + \rho \varepsilon + S_k, \quad (3.53)$$

where P_k is the production of turbulent kinetic energy (TKE) due to mean velocity shear, P_b is the production of TKE due to buoyancy, S_k is a user-defined source and σ_k is the turbulent Prandtl number for k.
The transport equation for the turbulent dissipation rate ε is given by:

$$\frac{\partial (\rho \varepsilon)}{\partial t} + \frac{\partial (\rho \langle u_i \rangle \varepsilon)}{\partial x_i} = \\ = \frac{\partial}{\partial x_j} \left[\left(\mu + \frac{\mu_{\text{turb}}}{\sigma_\varepsilon} \right) \frac{\partial \varepsilon}{\partial x_j} \right] + C_1 \frac{\varepsilon}{k} (P_k + C_3 P_b) - C_2 \rho \frac{\varepsilon^2}{k} + S_\varepsilon, \quad (3.54)$$

where C_1, C_2, C_3, C_μ are model coefficients that vary within $k - \varepsilon$ turbulence models, S_ε is a user-defined source and σ_ε is the turbulent Prandtl number for ε.

Combining the last equation with the relation between the dissipation rate ε and the specific dissipation rate ω, $\varepsilon = C_\mu \hbar\omega$, equation (3.55) is obtained:

$$\frac{\partial(\rho\varepsilon)}{\partial t} + \frac{\partial(\rho\langle u_i\rangle\varepsilon)}{\partial x_i} = \frac{\partial}{\partial x_j}\left[\left(\mu + \frac{\mu_{\text{turb}}}{\sigma_\varepsilon}\right)\frac{\partial\varepsilon}{\partial x_j}\right] + \frac{\gamma}{\nu_{\text{turb}}}P_k - \beta\rho\omega^2 + \frac{2\rho\sigma_\omega^2}{\omega}\frac{\partial\hbar}{\partial x_j}\frac{\partial\omega}{\partial x_j} \quad (3.55)$$

Without the last term this equation represents the transport equation for the specific dissipation rate ω.

SST $\hbar - \omega$ model:

The $\hbar - \varepsilon$ model tends to show great results in the free stream region and the $\hbar - \omega$ model has a good accuracy in the boundary layer region close to the wall [13]. It is possible to combine the advantages of these two turbulence models using a blending function:

$$\frac{\partial(\rho\varepsilon)}{\partial t} + \frac{\partial(\rho\langle u_i\rangle\varepsilon)}{\partial x_i} = \\ = \frac{\partial}{\partial x_j}\left[\left(\mu + \frac{\mu_{\text{turb}}}{\sigma_\varepsilon}\right)\frac{\partial\varepsilon}{\partial x_j}\right] + \frac{\gamma}{\nu_{\text{turb}}}P_k - \beta\rho\omega^2 + (1-F_1)\frac{2\rho\sigma_\omega^2}{\omega}\frac{\partial\hbar}{\partial x_j}\frac{\partial\omega}{\partial x_j} \quad (3.56)$$

If F_1 is zero, the last term remains and thus the equation shown above is the transport equation for ε representing a $\hbar - \varepsilon$ turbulence model.
If F_1 is 1, the last term vanishes and thus the equation is the transport equation for ω representing a $\hbar - \omega$ turbulence model [13].

$\hbar - \zeta - f$ model

The $\hbar - \zeta - \mathrm{f}$ model is based on a non-linear eddy viscosity approach, where the eddy viscosity ν_{turb} is defined as [10]:

$$\nu_{\text{turb}} = C_{k\zeta\mathrm{f},\nu}\,\zeta\frac{\hbar^2}{\varepsilon} \quad (3.57)$$

and three different transport equations for k , ε and ζ written as:

$$\rho\frac{D\hbar}{Dt} = \rho(P_\hbar - \varepsilon) + \frac{\partial}{\partial x_j}\left(\left[\rho\left(\nu + \frac{\nu_{\text{turb}}}{\sigma_{\hbar\zeta\mathrm{f},k}}\right)\frac{\partial\hbar}{\partial x_j}\right]\right), \quad (3.58.a)$$

$$\rho\frac{D\varepsilon}{Dt} = \rho\frac{(C^*_{\hbar\zeta\mathrm{f},\varepsilon 1}P_\hbar - C_{\hbar\zeta\mathrm{f},\varepsilon 2}\varepsilon)}{t_{\hbar\zeta\mathrm{f}}} + \frac{\partial}{\partial x_j}\left(\left[\rho\left(\nu + \frac{\nu_{\text{turb}}}{\sigma_{\hbar\zeta\mathrm{f},\varepsilon}}\right)\frac{\partial\varepsilon}{\partial x_j}\right]\right), \quad (3.58.b)$$

$$\rho\frac{D\zeta}{Dt} = \rho\mathrm{f} - \rho\frac{\zeta}{\hbar}P_\hbar + \frac{\partial}{\partial x_j}\left(\left[\rho\left(\nu + \frac{\nu_{\text{turb}}}{\sigma_{\hbar\zeta\mathrm{f},\zeta}}\right)\frac{\partial\zeta}{\partial x_j}\right]\right), \quad (3.58.c)$$

are solved. The here appearing production term of the turbulence kinetic energy $P_\hbar$ is defined as:

$$P_\hbar = -\langle u_i' u_j'\rangle\frac{\partial\langle u_i\rangle}{\partial x_j} \quad (3.59)$$

The function $C^*_{\hbar\zeta\mathrm{f},\varepsilon 1}$ is used to dampen ε near solid walls by

$$C^*_{\hbar\zeta\mathrm{f},\varepsilon 1} = C_{\hbar\zeta\mathrm{f},\varepsilon 1}\left(1 + 0.045\sqrt{\frac{1}{\zeta}}\right). \quad (3.60)$$

The elliptic relaxation function f, occurring in equation, is obtained from the solution of equation:

$$\mathrm{f} - \ell^2_{\hbar\zeta\mathrm{f}}\frac{\partial^2 \mathrm{f}}{\partial x_i^2} = \left(C_{\hbar\zeta\mathrm{f},1} + C_{\hbar\zeta\mathrm{f},2}\frac{P_\hbar}{\varepsilon}\right)\frac{(2/3-\zeta)}{t_{\hbar\zeta\mathrm{f}}}, \quad (3.61)$$

where the timescale $t_{\hbar\zeta\mathrm{f}}$ and length-scale $\ell_{\hbar\zeta\mathrm{f}}$ are defined as:

$$t_{\hbar\zeta\mathrm{f}} = \max\left(min\left(\frac{\hbar}{\varepsilon}, \frac{0.6}{\sqrt{6}C_{\hbar\zeta\mathrm{f},\nu}|S|\zeta}\right), C_{\hbar\zeta\mathrm{f},t}\left(\frac{\nu}{\varepsilon}\right)^{\frac{1}{2}}\right), \quad (3.62.a)$$

$$\ell_{\hbar\zeta\mathrm{f}} = C_{\hbar\zeta\mathrm{f},\ell}\, max\left(min\left(\frac{\hbar^{\frac{3}{2}}}{\varepsilon}, \frac{\hbar^{\frac{1}{2}}}{\sqrt{6}C_{\hbar\zeta\mathrm{f},\nu}|S|\zeta}\right) C_{\hbar\zeta\mathrm{f},\eta}\frac{\nu^{\frac{3}{4}}}{\varepsilon^{\frac{1}{4}}}\right). \quad (3.62.b)$$

3.3 CAA models

A typical aeroacoustic simulation requires [9] the resolution of the Navier-Stokes equations using high-resolution turbulence models and the resolution of analytical or computational acoustic wave propagation models.
There are two main categories of numerical methods:

- Direct methods: the flow field and the aerodynamic field are solved simultaneously. The compressible Navier-Stokes equations are solved in the whole domain. Although it would be the most accurate method, the computational cost is high.
- Hybrid methods: the sound propagation and the sound generation are uncoupled. Usually, sound sources are computed from the CFD simulation and, starting from the computed sources, acoustic models are applied to get the solution of the acoustic wave propagation.

The noise can be tonal, i.e. with distinct peaks at a specific frequency, or broadband, the latter being chaotic in nature and characteristic of noise due to turbulence.
When carrying out an acoustic analysis it is important to capture the noise sources and frequencies relevant to the acoustic analysis.
Aeroacoustic models can mainly deal with three tasks:

- Prediction of near field noise using compressible Detached Eddy Simulation (DES) or LES models: these models do not work accurately in the far field, the fluctuations that generate noise are much smaller than the flow properties. If there isn't an adequate resolution across the entire domain, sound waves quickly dissipate as they move away from the source. To accurately resolve turbulence through these models would require meshes that are too dense and would be computationally too expensive. The commonly used solution is the exploitation of hybrid CFD/CAA models where the DES or/and LES are coupled to acoustic propagation models.

- Prediction of mid field noise through the use of acoustic wave equation, linearized Euler equation or acoustic perturbation equation: high fidelity DES or LES type models can be coupled with an acoustic propagation model, but not without problems.
- Prediction of far field noise using Ffwocs Williams Hawking (FWH): FWH methods allows for the superimposition of all noise sources (monopole, dipole, quadrupole) on a surface, enabling the calculation of the acoustic field in a mesh-less manner. The limitation is that FWH assumes that sound propagates in a free acoustic field; therefore, no other solid bodies can be present outside the source.

Among the acoustic models used by the most well-known commercial software are:

- Broadband model.
- Perturbed Convective Wave Equation (PCWE) model.

3.3.1 Broadband models

For near-field noise prediction, Star-ccm+ and other commercially available CFD solvers, offer a group of models capable of evaluating broadband noise sources. These sources consist of volumetric distributions of quadripolar source terms and surface distributions of dipolar source terms.
In the frequency domain, broadband noise has a continuous spectrum, the acoustic energy is distributed continuously among all the frequencies of a given range. This model calculates the position and intensity of these aerodynamically generated sources by exploiting the field quantities resulting from the RANS.

Curle noise source model

This model estimates the sound generated per unit area by dipolar-type terms.
Specifically, the model evaluates the noise generated by the turbulent boundary layer on a solid surface, assuming isotropic turbulence and low Mach number.
The noise is generated by surface pressure variations due to the presence of a solid body immersed in the fluid. Starting from the density fluctuations ρ':

$$\rho'(\boldsymbol{x},t) = \frac{1}{(4\pi c_0^3)} \int_S \left[\frac{(\boldsymbol{x}-\boldsymbol{y})}{r^2} \frac{\partial p}{\partial t}\left(\boldsymbol{y}, t - \frac{r}{c_0}\right) \right] \cdot \boldsymbol{n}\, dS(\boldsymbol{y}), \qquad (3.63)$$

by assuming small perturbations and adiabatic problem it follows that $p' = c_0^2 \rho'$, therefore:

$$p'(\boldsymbol{x},t) = \frac{1}{(4\pi c_0)} \int_S \left[\frac{(\boldsymbol{x}-\boldsymbol{y})}{r^2} \frac{\partial p}{\partial t}\left(\boldsymbol{y}, t - \frac{r}{c_0}\right) \right] \cdot \boldsymbol{n}\, dS(\boldsymbol{y}) \qquad (3.64)$$

In the far field $|\boldsymbol{x}-\boldsymbol{y}| \cdot n = \cos(\theta)$ and the acoustic intensity per unit of solid surface is approximated:

$$\overline{p'^2} \approx \frac{1}{(16\pi^2 c_0^2)} \int_S \left[\frac{(\cos\theta)^2}{r^2} \overline{\left[\frac{\partial p}{\partial t}\left(\boldsymbol{y}, t - \frac{r}{c_0}\right)\right]^2} \right] \cdot A_c(\boldsymbol{y}) dS(\boldsymbol{y}), \qquad (3.65)$$

where A_c represents the acoustic correlation area and θ is the angle between r (the distance between the source and the far-field observer) and the normal $\boldsymbol{n}$.

Surface Acoustic Power (P_{SA}) can be calculated as:

$$P_{\mathrm{SA}} = \frac{1}{\rho_0 c_0}\left[\int_0^{2\pi}\int_0^{\pi}\overline{p'^2}\, r^2 sin\theta\, d\theta d\gamma\right], \tag{3.66}$$

$$P_{\mathrm{SA}} = \frac{1}{(12\pi^2\rho_0 c_0^3)}\int_S \overline{\frac{\partial p^2}{\partial t}}\, A_c(\boldsymbol{y}) dS(\boldsymbol{y}) = \frac{1}{(12\pi^2\rho_0 c_0^3)}\cdot 4\pi^3\overline{\left(u'_{\mathrm{turb}}\right)^2}\,(p'_{\mathrm{w}})^2. \tag{3.67}$$

With:

- $\overline{\left(u'_{\mathrm{turb}}\right)^2} = \frac{2}{3}\max\left(k, \frac{3.3\tau_{\mathrm{w}}}{\rho_0}\right)$: mean square turbulent velocity.
- $p'_{\mathrm{w}} = \max\left(3\tau_{\mathrm{w}}, 0.7\rho_0 \cdot \frac{2}{3}k\right)$: wall pressure fluctuation.
- τ_{w}: wall shear stress.
- ρ_0: far field density.

Proudman noise source model

This model evaluates the acoustic power per unit of volume by calculating the sound generated by quadrupole sources.
In the Proudman model, under the hypothesis of isotropic turbulence, high Reynolds number and almost incompressible flow, the Acoustic Power (P_{AV}) per unit volume appears as:

$$P_{\mathrm{AV}} = \alpha\rho_0 \frac{u^3}{L}\frac{u^5}{c_0^5}. \tag{3.68}$$

Where:

- α: is a constant linked to the shape of the longitudinal velocity correlation.
- L: is the integral scale of the longitudinal velocity.

Mesh Frequency cutoff formulation

The mesh frequency cutoff analysis allows for the determination, starting from a steady solution, whether the grid used has sufficient resolution to capture the turbulent structures in the frequency range of interest.
Mendonça [14] discovered that given a cell size $L = D$ with turbulent kinetic energy k, the smallest structure that can be captured by the grid has $2D$ dimension, and its velocity fluctuation is $\sqrt{(2/3)k}$ therefore the maximum frequency that can be resolved by the grid is:

$$f_{co} = \frac{\sqrt{\left(\frac{2}{3}\right)k}}{2L}. \tag{3.69}$$

3.3.2 Perturbed convective wave equation model

The Perturbed Convective Wave Equation (PCWE) model applies a wave equation to the pressure calculated from the incompressible Navier Stokes equations. The acoustic/viscous splitting technique for the prediction of flow induced sound was first introduced by [15] and afterwards many groups presented alternative and improved formulations [1].

The fluid dynamic variables are divided into a medium, an incompressible and a compressible component:

$$p = \bar{p} + p_{\mathrm{ic}} + p_{\mathrm{c}} = \bar{p} + p_{\mathrm{ic}} + p^{\mathrm{a}}, \quad (3.70)$$

$$\boldsymbol{u} = \bar{\boldsymbol{u}} + \boldsymbol{u}_{\mathrm{ic}} + \boldsymbol{u}_{\mathrm{c}} = \bar{\boldsymbol{u}} + \boldsymbol{u}_{\mathrm{ic}} + \boldsymbol{u}^{\mathrm{a}}, \quad (3.71)$$

$$\rho = \bar{\rho} + \rho_1 + \rho_a. \quad (3.72)$$

The density is corrected to meet the following requirements:

- The acoustic field is a fluctuating field.
- The acoustic field is irrotational.
- The acoustic field requires a compressible medium and incompressible pressure fluctuations are not equivalent to acoustic fluctuations.

Consequently, it is possible to calculate the acoustic potential as a function of the incompressible field.
The PCWE wave equation solves the acoustic potential ψ^{a}, from which the pressure p^a, velocity u^a and acoustic density ρ^a can be derived:

$$\frac{1}{c_0^2}\frac{D^2\psi^{\mathrm{a}}}{Dt^2} - \nabla\cdot\nabla\psi^{\mathrm{a}} = -\frac{1}{\rho_0 c_0^2}\frac{Dp_{\mathrm{ic}}}{Dt}, \quad (3.73)$$

Where $\frac{D}{Dt}$ represents the material derivative, which computes the time rate of change of any quantity for a portion of a material moving with a velocity $\boldsymbol{u}$ and it's defined as follows:

$$\frac{D}{Dt}(x) = \frac{d}{dt}(x) + (\boldsymbol{u}\cdot\nabla)(x). \quad (3.74)$$

where the first term on the right end side is the Eulerian derivative (i.e. the rate of a change at a fixed point) and the second term is the advection term i.e. the rate of change associated with the movement of the fluid through the background field.

From the wave equation it is possible to see that the source term is the substantial derivative of the incompressible pressure considering the average flow [16].
This equation describes the acoustic sources generated by incompressible flow structures and the associated wave propagation.
Furthermore, since the calculator must calculate a single variable, the computational time is significantly reduced.
The acoustic pressure turns out to be the first derivative of the potential:

$$p^{\mathrm{a}} = \rho\frac{D\psi^{\mathrm{a}}}{Dt} \quad (3.75)$$

$$\rho^{\mathrm{a}} = \frac{p^{\mathrm{a}}}{c_0^2} + \rho \quad (3.76)$$

$$\boldsymbol{u}^{\mathrm{a}} = -\nabla\psi^{\mathrm{a}} \quad (3.77)$$

Edge conditions can be set as reflective or non-reflective. Assigning non-reflective conditions is important in regions not characterized by solid walls, to avoid the reflection of signals that would pollute the solution.
In practice, the calculator applies damping functions which eliminate the waves at the walls.

Chapter 4: Setup

In this chapter, the setup of the benchmark axial fan [17] studied for the following thesis will be described. In *Chapter 4.1* the experimental setup will be described, in *Chapter 4.2* the focus will be on the creation of the CAD model of the same setup, paying particular attention to the modifications and simplifications made to the geometry in preparation for the fluid dynamic analysis and finally in *Chapter 4.3* the focus will be on the creation of the fluid dynamic mesh.

4.1 Experimental setup

The experimental setup is described in [17]. The main subject of the experiment is an axial fan positioned in a duct which is in turn set in a wall. A scaffold supports the electric motor that powers the fan. Two sets of microphones are positioned to obtain far-field and near-field information at the blade tip. The first, composed of 7 microphones, is positioned at a radial distance of one meter from the fan nozzle, the second is located on the wall of the duct and is composed of a set of 15 pressure sensors.
Further information on the experimental setup can be found at [18].

The fan of the benchmark case was designed with the blade element theory for low solidity fans. In terms of size and operating conditions, it is a typical fan to be used in commercial applications. Since the fan was designed as a benchmark case, the reproduction of the geometry was a goal. Therefore, the fan was designed with zero blade skew and the design was not optimized for fluid dynamics or acoustic behavior. The blades consist of NACA 4510 profiles [17].

The National Advisory Committee for Aeronautics (NACA) was a United States federal agency founded to undertake, promote, and institutionalize aeronautical research. In the NACA four-digit wing sections, each digit of the number defines a characteristic of the profile: the first digit describes the maximum camber as percentage of the chord, the second digit describes the distance of maximum camber from the airfoil leading edge in tenths of the chord, the last two digits describe the maximum thickness of the airfoil as percent of the chord.

The measurements were made in a standardized anechoic inlet test chamber (see Figure 4.2) according to ISO 5801 [19], where ISO stands for International Organization for Standardization. The goal of this independent organization is to develop and publish international standards.

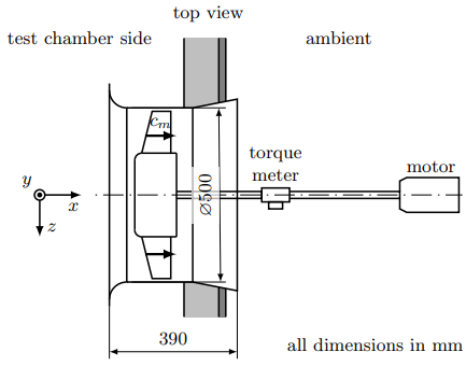

Figure 4.1: Experimental setup – detail view [17]

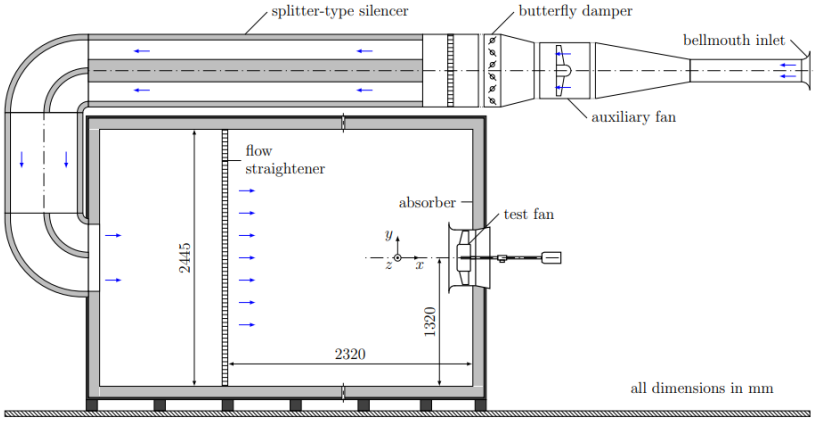

Figure 4.2: Standardized inlet test chamber [17]

Table 4-1: Fan parameters [17]

Fan diameter	495 mm
Hub diameter	248 mm
Tip clearance	2.5 mm
Blades	9
Volumetric flow	1.4 m^3/s
Total-to-static pressure difference	150 Pa
Rotational speed	1486 1/min
Circumferential velocity hub	19.4 m/s
Circumferential velocity tip	38.9 m/s
Chord length hub	103 mm
chord length tip	58 mm
Reynolds number hub	1.25 E5
Reynolds number tip	1.50 E5

In *Table 4.1* other parameters of the Fan are shown.
Considering the speed of the blade tip, in design conditions, of 38.9 m/s, which will probably be the highest speed reached by the fluid, it is possible to calculate the local Mach number equal to $M \approx 0.113 < 0.3$, therefore the hypothesis of an incompressible regime it's valid.

The volumetric flow $\dot{V}$ is adjusted by butterfly dampers and an auxiliary fan in the inlet section. The flow field is rectified in the first half of the inlet chamber by a flow straightener.

The measured pressure rise of the fan at the design point is $\Delta p = 126.5$ Pa. However, the design pressure difference is not completely reached due to unconsidered losses like tip flow [17].
At the design point the efficiency, according to:

$$\eta = \frac{\dot{V}\Delta p}{2\pi n M_Q}, \tag{4.1}$$

with M_Q being the torque and n the rotational velocity of the shaft, is $\eta = 53\%$.
The aeroacoustic results are obtained through the two sets of microphones briefly described previously and shown in *Figure 4.3* and *Figure 4.4*.
The signal sampling frequency is $f_\mathrm{s} = 48$ kHz while the data acquisition time is $T = 30\ s$.

Figure 4.3: Wall pressure transducers

Figure 4.4: Free field microphones

The sound power level is computed according to:

$$L_\mathrm{W} = \bar{L}_\mathrm{P} + 10\log\left(\frac{S_1}{S_0}\right)\ \mathrm{dB} \tag{4.2}$$

where $\bar{L}_\mathrm{P}$ represents the time averaged sound pressure level and the hull of the measurement aera is $S_1 = 6.28\ \mathrm{m}^2$ with $S_0 = 1\ \mathrm{m}^2$.
The time averaged sound power level for all microphones is computed as:

$$\bar{L}_\mathrm{P} = 10\log\left(\frac{1}{N}\sum_{n=1}^{N}\frac{1}{T}\int\frac{p_n^2}{p_\mathrm{ref}^2}dt\right)\ \mathrm{dB}. \tag{4.3}$$

With the reference pressure $p_\mathrm{ref} = 20$ µPa.

For a frequency range of 100 Hz to 10 kHz the measured sound power level is $L_W = 87.3$ dB. The spectrum of the sound power level is shown in *Figure 4.5*. The first Blade Passing Frequency (BPF) can be seen as a sharp peak at 223 Hz, the second BPF at 446 Hz and the third at 675 Hz. Broader peaks are around 340 Hz and 500 Hz that exceed the ones from the BPF. They are expected to result from the interaction of the tip flow with the blades. They are going to be referred to as the first and second visible subharmonic peak. Above 800 Hz, the spectrum consists of broadband noise [17].
The theoretical first blade passing frequency is calculated as follows:

$$BPF = \frac{n_{\mathrm{RPM}}}{60} * \mathcal{N} = \frac{1486}{60} * 9 = 223.9 \text{ Hz} \qquad (4.4)$$

where n_{RPM} is the rotational speed in rotation per minutes and $\mathcal{N}$ is the number of blades.

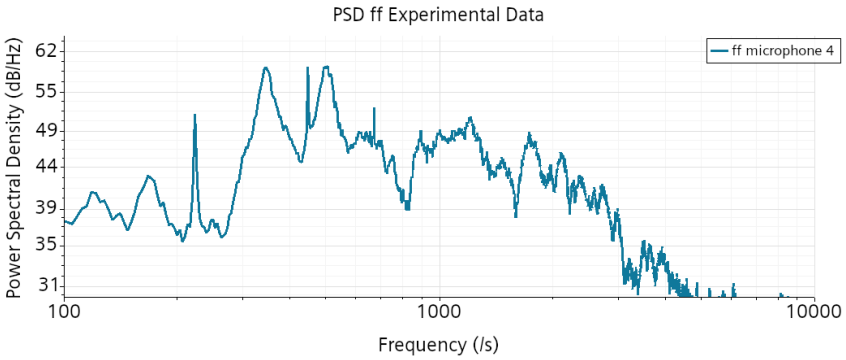

a: Microphone 4

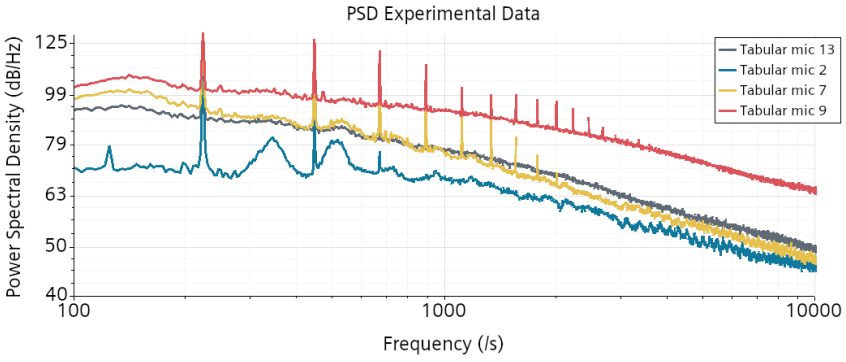

b: wall pressure sensors 2,7,9,13

Figure 4.5: Experimental PSD results

For a ducted fan, in general, only certain modes can propagate in a duct at a given frequency, but there is an exception: if the duct is short (less than an acoustic wavelength) the non-propagating modes can still reach the inlet and couple with the acoustic far field.
It follows that only if $f < \frac{c_0}{L_{\mathrm{DUCT}}}$ which, for the fan studied in this thesis, is $332/0.390 = 851$ Hz, the non-propagating modes can couple with the acoustic field, so it means that below this frequency the duct has no effect.

Looking at the experimental spectrum shown in *Figure 4.5* it can be concluded that the duct does not have an important effect for most of the frequencies generated by the fan studied in this thesis.

4.2 CAD

Computer-Aided Design (CAD) refers to the use of computers in the design process of objects. It's used to create precise tridimensional models, CAD modeling specifically refers to the process of creating digital representations of real-world objects or systems using CAD software. Starting from the file present in [18], simplifications to the geometry are implemented, both in view of the meshing operation and in order to reduce the computational cost of the CFD analysis. Note that the original CAD (*Figure 4.6*) presents the motor support structure and all the screw holes.

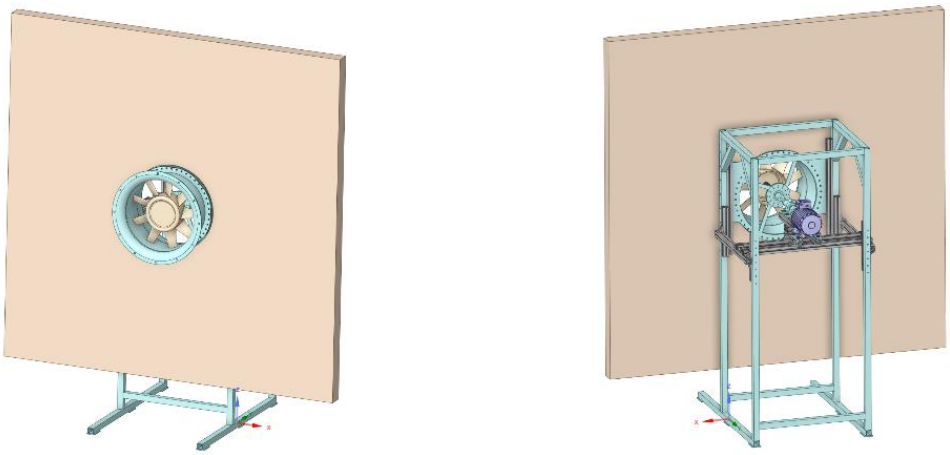

Figure 4.6: CAD with details

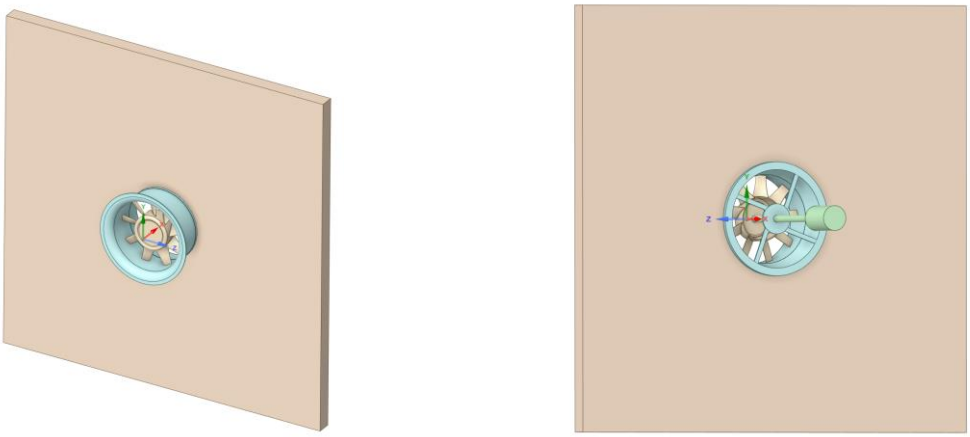

Figure 4.7: Simplified geometry

The simplification implemented consists in the removal of the support, the closing of the gaps and screw holes and a general simplification of the geometries (*Figure 4.7*). The motor and the shaft are replaced by cylindrical structures and even the back of the diffuser loses all the geometric complexities in favor of a circular structure. Starting from the geometry of the fan, the computational domain created is made up of three regions (*Figure 4.8*):

- Inlet: slightly smaller than the test chamber, measuring 2.32m x 2.4m x 2.4m, is the region positioned in front of the fan inlet.

- Fan: it is the circular region that houses the blades, the rotor and a small part of the shaft, with a radius of 250 mm and a length of 196 mm. Immediately before this region there is the fan nozzle and immediately after there is the diffuser.
- Outlet: it is the region that houses the diffuser, the shaft and the electric motor. Measuring 2.0m x 2.4m x 2.4m, the wake develops in this region.

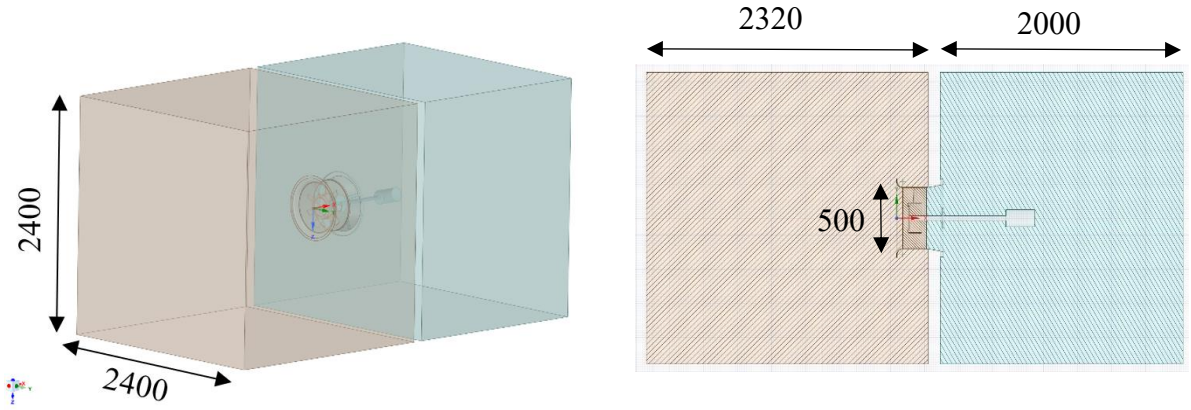

Figure 4.8: CFD domain

4.3 Workflow

In this chapter the aeroacoustic workflow for FIRE M and Star-ccm+ will be described.

4.3.1 FIRE M Workflow

Before describing the workflow, it is necessary to make a brief introduction to the structure adopted by FIRE M in writing the results. The results of a FIRE M simulation are found in the "simulation" folder within the project directory. The structure underlying "simulation" appears as in *Figure 4.9.*

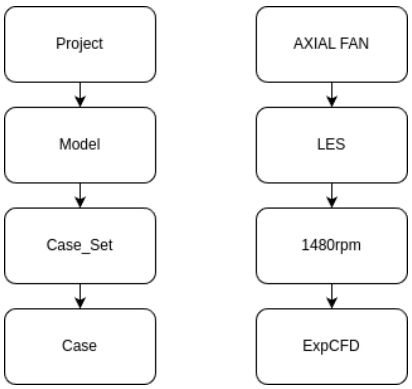

Figure 4.9: FIRE M project folder structure [20]

The *Project* group consists of the entire project, it can include one or more Models that correspond to the various modules available within the software, for example *FAME M, FIRE M* and *IMPRESS* are three models that deal respectively with mesh generation, numerical simulation and post processing. Each model can be divided into Case Sets which in turn can be divided into Cases. Within them, the results of the simulation are found. In the description of the workflow below, reference will be made to a structure of the *Model.Case_Set.Case* type to indicate the Model, the Case Set and the reference Case.
The FIRE M workflow consists of ten steps:

1. FAME M: creation of the CFD mesh and of the acoustic mesh.
2. FAME M (App): conversion of Acoustic mesh from *.flm2* format to *.cfs*.
3. FIRE M: *CARes.1480rpm.ExpCFD*: run of dummy model used from the software to target the acoustic mesh to use for mapping the parameters.
4. FIRE M: *STEADY.1480rpm.Conv*: used to get a converged steady-state solution.
5. FIRE M: *LES.1480rpm.Conv*: used to get a converged large eddy simulation solution.
6. FIRE M: *LES.1480rpm.ExpCFD*: runs a LES simulation and performs the mapping of the parameters on the targeted acoustic mesh.
7. FAME M (App): Calculation of the PCWE source term, temporal blending and set up of OpenCFS .xml files. All results are stored into *CARes.OpenCFS.PCWE/input.*
8. OpenCFS: run of *cfsdat* to calculate the nodal loads. It does the interpolation of the results from the cells to the nodes with the conservative cell centroid method.
9. OpenCFS: run of *opencfs* to get the first derivative of the acoustic potential on the entire domain and on the microphones position.
10. Postprocessing of the acoustic results.

4.3.2 Star-ccm+ Workflow

As regards Star-ccm+, the workflow is simpler, in fact five steps are simply carried out:

1. Import of the mesh created with FAME M which will be used for both the CFD and the CAA simulation.
2. Run of a Steady state RANS simulation to get the starting flow.
3. Run of LES simulation to get a converged unsteady flow.
4. Activation of PCWE model.
5. Postprocessing of the acoustic results.

Chapter 5: Computational Fluid Dynamics

This chapter will describe the fluid dynamic analysis of the axial fan carried out through the use of two software: FIRE M and Star-ccm+. The objective is to obtain a converged Large Eddy Simulation (LES), to be used as a starting point for the aeroacoustic simulation.

5.1 Mesh

Starting from the CAD model, through the use of the FAME M software, the fluid dynamic mesh is derived. As a starting point, the grid dimensions adopted in [21] were used. In this research, a fluid dynamic analysis is carried out through the Detached Eddy Simulation (DES) turbulence model. This model carries out a blending operation between the LES and the unsteady RANS, near the wall the turbulence is resolved by the RANS while, in the rest of the field, is resolved by the LES. This simplification allows for the reduction of the number of cells and the computational cost of the Detached Eddy Simulation, against a reduced accuracy of the turbulence, especially near the wall. On the paper, a mesh of constant size equal to 2mm is used in the rotating area. Downstream of the rotating area, for a length equal to 1.8 D (where D is the diameter of the rotating area), the mesh has a size of 8mm, to capture the fan's wake well. Upstream of the rotating zone, the same dimension is applied for 0.5 D. Outside the refinement zone, the grid size gradually increases up to the maximum size of 100mm.

In order to carry out a simulation with the large eddy simulation model, it is of primary importance to respect the criterion $y^+ \approx 1$. This imposition guarantees that the model is able to correctly capture the generation of wall turbulence. Specifically, the transition from the viscous layer to the developed layer is well resolved.
The non-dimensional wall distance y^+ is a parameter used in describing the velocity profile of the turbulent boundary layer. This quantity is given by the formula:

$$y^+ = \frac{yu^*}{\nu}, \qquad (5.1)$$

where u^* represents the friction velocity and can be calculated from the expressions:

$$u^* = \sqrt{\frac{\tau_w}{\rho}}, \qquad (5.2)$$

$$\tau_w = \mu \left(\frac{\partial u}{\partial y}\right)_{y=0}. \qquad (5.3)$$

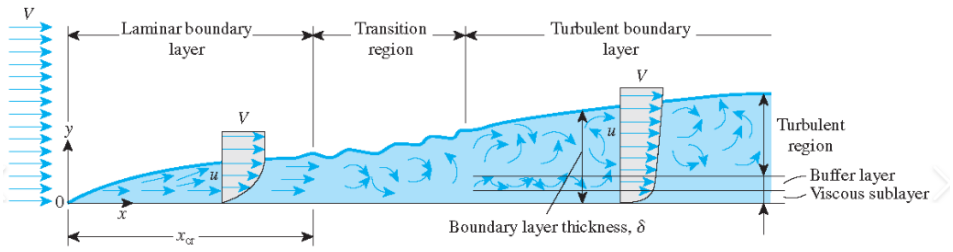

Figure 5.1: Turbulent boundary layer [22]

It has been demonstrated that within the viscous sublayer ($y^+ < 5$) the velocity profile has a linear trend $u^+ = y^+$, while in the turbulent region ($y^+ > 50$) it follows a logarithmic trend [7]

$$u^+ = \frac{1}{k} \ln y^+ + c$$

In order to meet the $y^+ \approx 1$ criterion in the rotating zone, various meshes are tested.

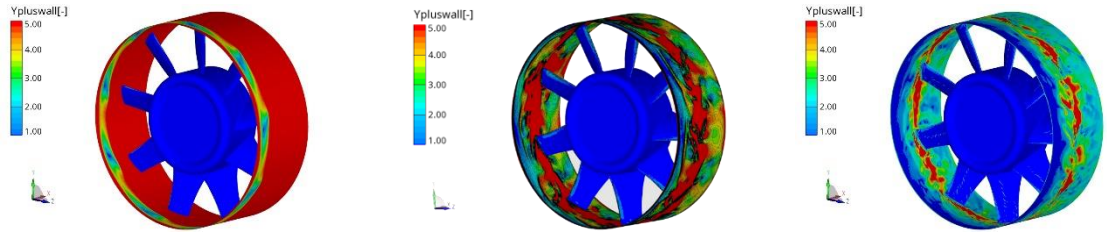

Figure 5.2: Different mesh resolution and change in y+

In Figure 5.2 it is possible to see three different meshes with a variable number of boundary layers, respectively from left to right:

- 10 layers on the fan and 3 layers on the external case, big spot with $y^+_{max} = 25$
- 10 layers on the fan and 5 layers on the external case, big spot with $y^+_{max} = 10$
- 10 layers on the fan and 6 layers on the external case, small spots with $y^+_{max} = 9$

The mesh on the right is chosen, which has small spots with $y^+ > 5$, i.e. outside the viscous sublayer, in the area between the blades, these small spots are considered acceptable.

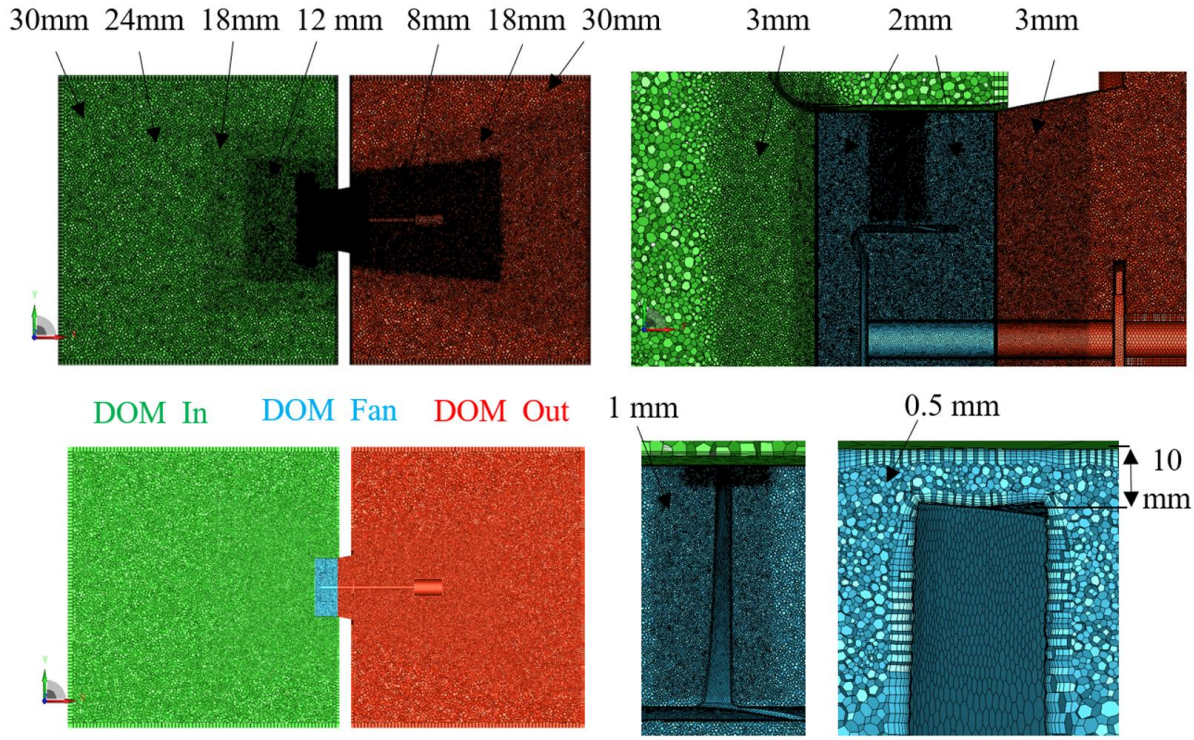

Figure 5.3: Mesh

The mesh, like the CAD, is divided into three regions (*Figure 5.3*):

- Fan (*DOM_Fan*): consists of the rotating region, in light blue. It has a base size of 2mm, a refinement, which reaches the size of 1mm, is applied around the blades and around the tip of the blade the size drops to 0.5mm. The number of boundary layers is equal to

10 around the fan region and 6 layers for the external case, both with growth rate equal to 1.4, the thickness of the boundary layer is equal to 2mm.

- Inlet (*DOM_In*): is the region upstream of the fan, in green. At the interface between the rotating region and the inlet, the size is equal to 2mm. Through the use of four cylindrical datum objects, a progressive refinement from 2mm up to the maximum size of 30mm, is applied. The size of the cells on the external surfaces also goes from 30mm, in the fluid regions, to progressively reduce along the solid walls to reach the size of 2mm in conjunction with the interface. The number of boundary layers is equal to 3 with a thickness equal to the size of the contiguous surface cell.
- Outlet (*DOM_Out*): this region, in red, located downstream of the fan, is characterized by the presence of the engine and is the area where the wake develops. Three conical datum objects are used to refine the grid, which progressively goes from 2mm up to the maximum size of 30mm. Similarly to the Inlet, the size of the surface cells progressively decreases to match the value present at the interface; the same considerations made for the Inlet also apply to the boundary layers.

It should be noted, in order to avoid misunderstandings, that in the language of FAME M the "boundary layers" do not only constitute the layers of cells that extend out from solid walls, but also the layers, made up of prismatic cells, that extend from fluid surfaces and correspond to the "prism-layers" of Star-ccm+. At the interfaces with the rotating region there are 3 layers per side, having QUAD type cells near the rotating interface helps in terms of stability, compared to polygonal cells which could give rise to instability phenomena.
The mesh generated through FAME M is used in both FIRE M and Star-ccm+.
In *Table 5.1.1* it is possible to view the number of cells making up the mesh.

Table 5-1: Cell count

Stationary region: Max cell size	[mm]	30
Stationary region: Min cell size	[mm]	2
Rotating region: Max cell size	[mm]	2
Rotating region: Min cell size	[mm]	0.5
Cells in Stationary domain	[Millions]	13.549
Cells in Rotating domain	[Millions]	20.044
Total Cell Count	[Millions]	33.593

5.2 CFD Simulation settings

This chapter will discuss the settings used to perform CFD simulation in FIRE M and Star-ccm+ and the differences between the two.
As seen in *Chapter 4.3.1*, before performing the unsteady simulation with the LES turbulence model, a steady-state simulation is carried out with the RANS turbulence model. This simulation is carried out on a coarser mesh than the one used for the LES, this grid is composed of 30 million elements and with a number of boundary layers equal to 3 in the entire domain. The RANS simulation is run for 10k iterations, at the end of which a good pressure and velocity profile is obtained and the quantities monitored on surfaces and points have reached convergence. The FIRE M steady simulation was performed with the $k-\zeta-f$ turbulence model while in Star-ccm+ $SST\ k-\omega$ model was used.
The unsteady simulation is set to FIRE M in "angle mode", which means that a constant rotation step equal to $\Delta\alpha = 0.1°$ is chosen from which, considering a rotation speed equal to 1486rpm, a time step equal to at $\Delta t = 1.1216 \cdot 10^{-6}$ s, this time step is the one used by Star-ccm+. The

number of inner iterations is set equal to 20 and the numerical scheme chosen is of type second order implicit unsteady.

5.2.1 Initial conditions

As regards the initial conditions, a pressure equal to atmospheric pressure and a temperature of 300K are applied throughout the domain, resulting in a density equal to 1.1766 kg/m^3 from the ideal gas law. The software default values are left for turbulence.

Table 5-2: Initial conditions

Parameter	Value
Pressure	101325 Pa
Temperature	300 K
Density	1.1766 kg/m^3
Velocity	0 m/s
Turbulent kinetic energy (FIRE M)	0.375 m^2/s^2
Turbulence length scale (FIRE M)	0.001 m

5.2.2 Boundary conditions

A correct choice of boundary conditions is the key criterion for obtaining a convergent CFD simulation. Mainly four types of boundary conditions are applied:

- Wall: this condition is applied to all solid walls of the domain and consists of a non-slip constraint.
- Mass Flow Inlet: at the Inlet a Mass flow type condition equal to 1,652 kg/s equivalent to 1.4 m^3/s in the axial direction is assigned.
- Pressure Outlet: at the Outlet a pressure value equal to 101325 Pa is assigned. In both FIRE M and Star-ccm+ it is possible to avoid the formation of flow recirculation zones near the wall through the application of
    - FIRE M: Method: Mixed.
    - Star-ccm+: Backflow Specification: Environmental.
- Symmetry: External fluid regions, where flow aligned with the surface is expected, are assigned a symmetry condition that is equivalent to a slip condition.

As regards walls with rotation, a different approach is used in the steady and unsteady simulation. In the first case, a moving reference frame is defined on the *DOM_Fan* region. This approach, suitable for stationary simulations, keeps the mesh stationary and numerically simulates the rotation through the application of source terms that mimic its movement.
In FIRE M, for all the surfaces that are part of the moving reference frame, a wall speed is assigned and, since the case surrounding the fan is part of this region and it should be stationary, to make sure that it doesn't move, it is necessary to impose a wall speed equal and opposite to the rotational speed assigned to the region. This is done through the use of a wall moving formula. As regards the shaft present in the Outlet region, it is possible to assign a rotation through a wall velocity formula.
In Star-ccm+, similarly, it is necessary to define, for each surface, which reference system to adopt and, to avoid the external case having non-zero speed, it will be sufficient to assign it the "Lab reference frame" which, in this case, is stationary.

As regards the unsteady simulation, however, a Mesh deformation or rigid body motion type approach is implemented, where the geometry is actually rotated by the solver. In this case, it is necessary to define the region that contains the geometry to be rotated and it will be sufficient to assign to the surfaces the mesh deformation characteristic for FIRE M and the rotating reference system for Star-ccm+.

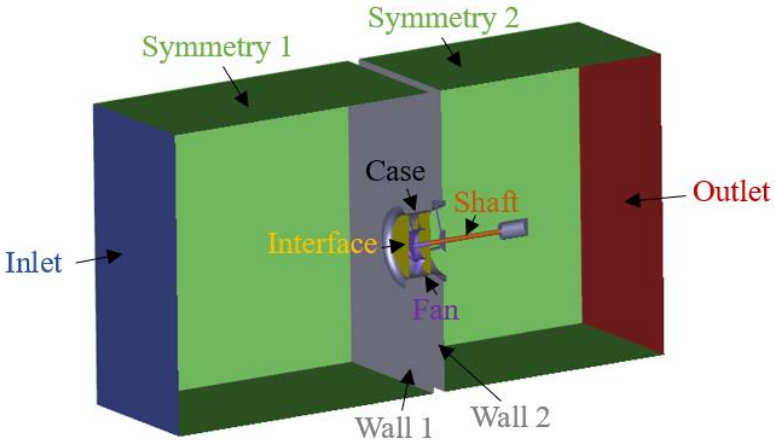

Figure 5.4: Boundary Conditions

5.2.3 LES: Solver Settings

This section describes the type of Solver used by the two software and highlights any differences. Both FIRE M and Star-ccm+ perform a second-order implicit unsteady LES simulation with a maximum of 20 inner iterations per time step.
In both cases, ideal, incompressible gas is used.

FIRE M

To calculate turbulence, FIRE M adopts the LES model with Coherent Structures Model (CSM) sub-model, this sub-grid model focuses on capturing coherent structures by locally determining the parameters on the basis of the latter [9].
The energy equation is set to *Initialization only*, which allows the user to set a temperature value which is kept constant throughout the whole simulation. The pressure-velocity coupling scheme is of type Simple/Piso and the gradients are calculated with the Least squared fit method.
In *Figure 5.5* it is possible to see the type of solver, the differencing scheme and the convergence criteria used for solving the continuity, momentum and turbulence equations.

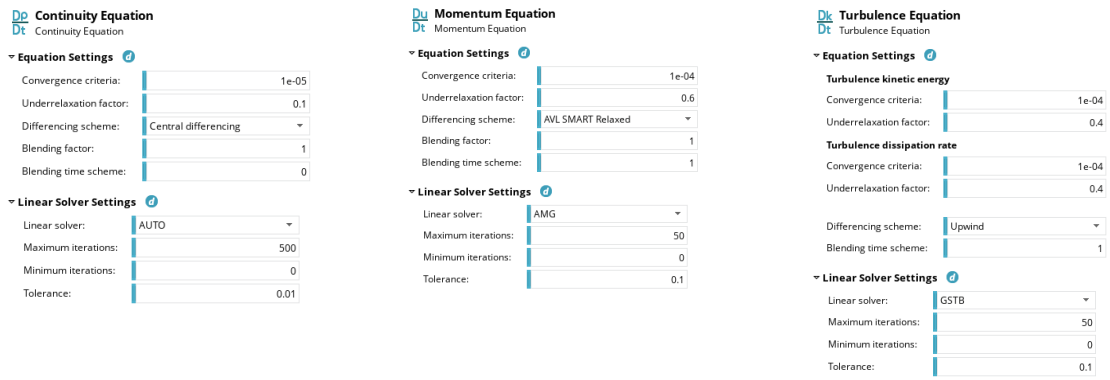

Figure 5.5: FIRE M Solver Control

Star-ccm+

To calculate turbulence, Star-ccm+ adopts LES with the Wall-Adapting Local Eddy-viscosity (WALE) sub-scheme, which adapts the eddy viscosity based on proximity to the wall. This model focuses on the flow behavior in the boundary layer [9].
The energy equation is decoupled from the continuity and momentum equations through the choice of the *Segregated Fluid Temperature* model, this solves the total energy equation with temperature as the solved variable. Enthalpy is then computed from temperature according to the equation of state.
The type of Solvers used by Star-ccm+ are AMG.
As regards the Segregated Flow, the Convection is calculated with a Bounded-Central scheme with upwind blending factor equal to 0.15 and adopts SIMPLE as the Implicit Scheme.
While as regards the Segregated Fluid Temperature model, the Convection is calculated at second order. In *Figure 5.7* it is possible to observe the properties of the AMG solver.

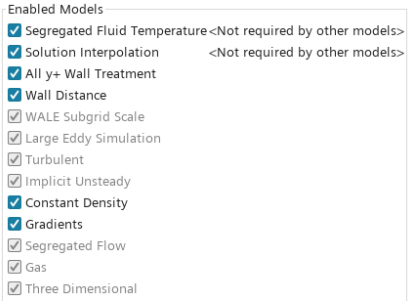

Figure 5.6: Star-ccm+ Continua

AMG Linear Solver - Properties

Properties		Properties		Properties	
Max Cycles	30	Max Cycles	30	Max Cycles	30
Verbosity	None	Verbosity	None	Verbosity	None
Convergence Tolerance	0.1	Convergence Tolerance	0.1	Convergence Tolerance	0.1
Cycle Type	Flex Cycle	Cycle Type	V Cycle	Cycle Type	V Cycle
Expert		Expert		Expert	
Enable Direct Solver	☐	Enable Direct Solver	☐	Enable Direct Solver	☐
Maximum Direct Solver Equations	32	Maximum Direct Solver Equations	32	Maximum Direct Solver Equations	32
Epsilon	0.0	Epsilon	0.0	Epsilon	0.0
Group Size Control	Auto	Group Size Control	Auto	Group Size Control	Auto
Group Size	4	Group Size	4	Group Size	4
Relaxation Scheme	Gauss-Seidel	Relaxation Scheme	Gauss-Seidel	Relaxation Scheme	Gauss-Seidel
Acceleration Method	None	Acceleration Method	Conjugate Gradient	Acceleration Method	None
Scaling	Disabled	Scaling	Auto	Scaling	Disabled

Figure 5.7: AMG Linear Solver Properties: from left to right Segregated Flow-Velocity, Segregated Flow-Pressure, Segregated Energy

5.3 CFD results

In this section the results of the CFD simulation will be analyzed and a comparison will be made between the two software.
The results were produced before the activation of the PCWE aeroacoustic model in Star-ccm+ and before activating the mapping operation in FIRE M.
Due to high workload of the simulation cluster and due to the fact that FIRE M Hybrid workflow was still in development while Star-ccm+ simulation was already running, for timing reasons, the export operations in FIRE M were started before reaching the same simulation time of Star-ccm+. The Star-ccm+ export operation was started after 10 rotation cycles while the FIRE M mapping operation was started after 9 rotation cycles.

5.3.1 Star-ccm+ fluid dynamics results

Instantaneous field

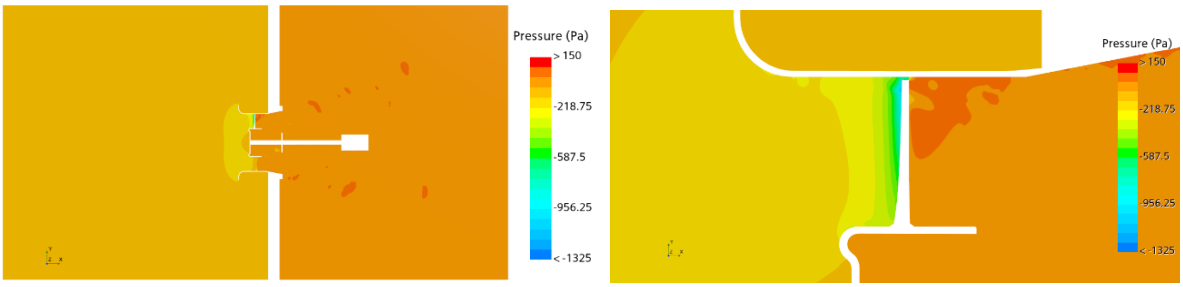

Figure 5.8: Instantaneous pressure field

From the instantaneous pressure field, the pressure rise across the fan, the low-pressure region on the top of the wing and the high-pressure region on the bottom, are well seen. For the purposes of the acoustic investigation, the gap between the blade and the external case will be particularly important. In this region, the flow is expected to recirculate towards the inlet and this area will be particularly important in the generation of the Blade Tip Vortex.

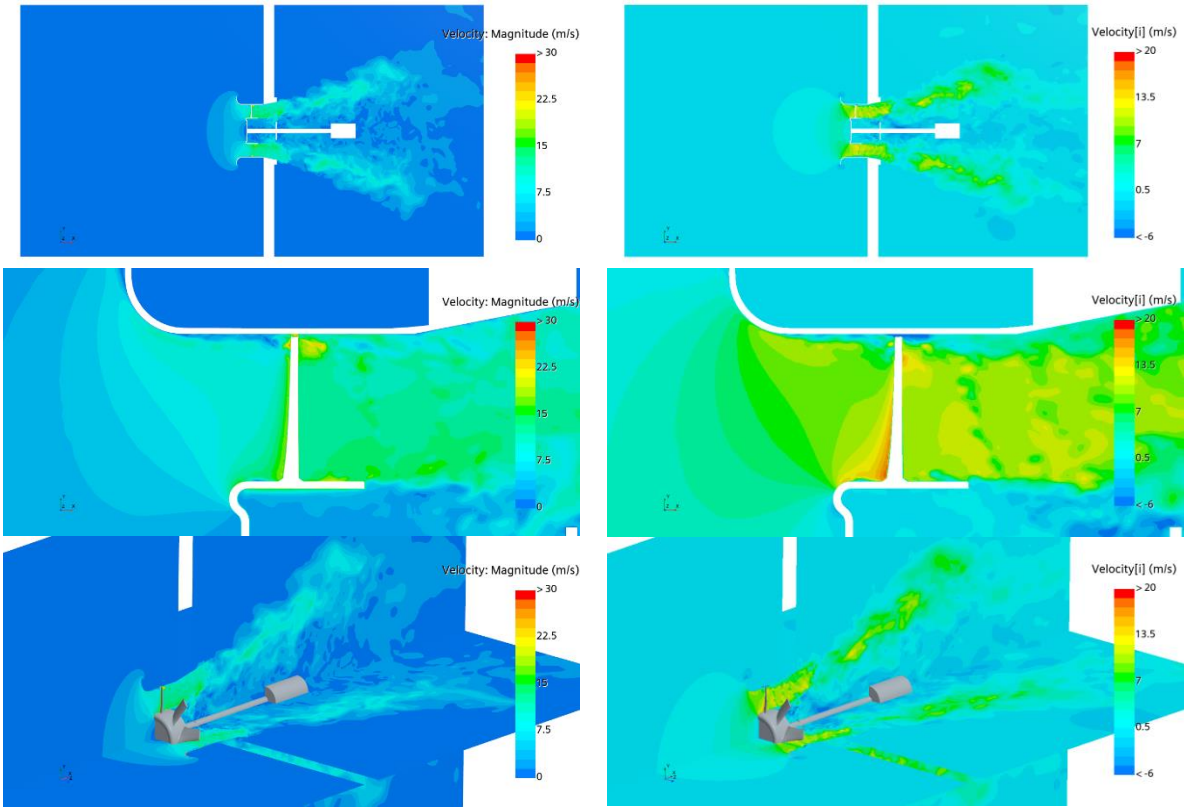

Figure 5.9: Velocity magnitude (left) and U-velocity (right) instantaneous fields

From the velocity field, it is possible to see the acceleration of the current at the inlet entrance and the further acceleration imposed by the fan. The extension of the wake and the turbulent structures are also clearly visible.
On the blade's top, the acceleration of the flow is visible. In the area immediately following the blade, the trails caused by the previous blade passages are visible from the U-velocity profile as regions of slightly lower speed. From the U-velocity field, it is also observable the

backflow occurring at the blade-case gap, this flow is caused by the very low-pressure region upstream of the fan.

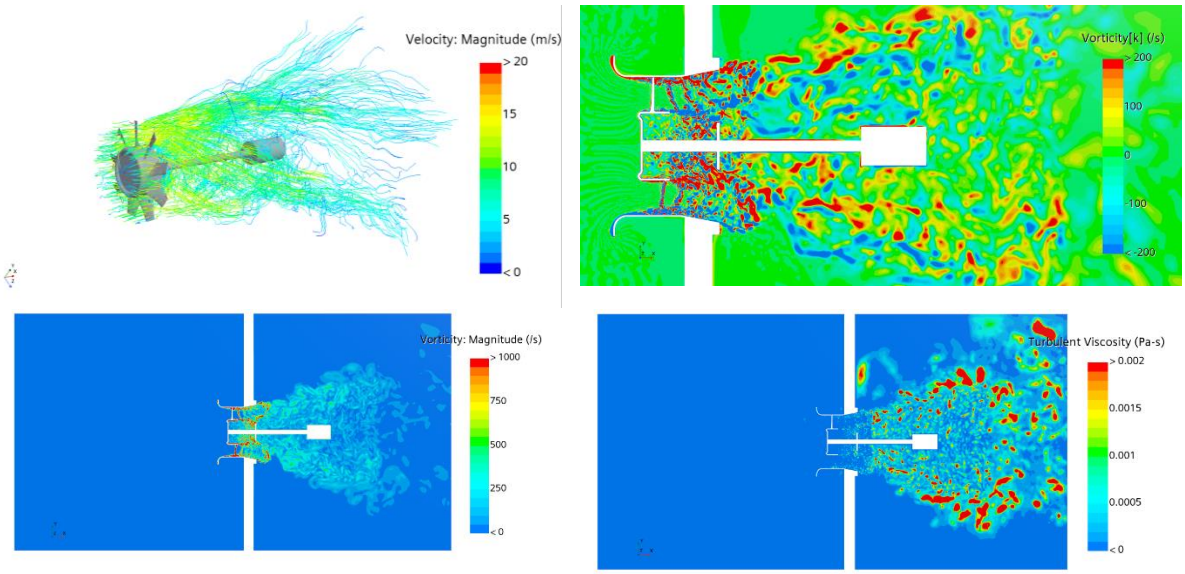

Figure 5.10: Streamlines, Vorticity magnitude, Z-Vorticity and Turbulent viscosity

In *Figure 5.10* it is possible to appreciate the characteristics of the wake. The rotationality of the flow is clearly visible from the streamlines, while the vorticity and turbulent viscosity highlight the vortical structures generated by the LES turbulence model. It is also seen that, at the end of the high refinement zone, the vorticity drops considerably since the mesh is no longer able to resolve the smallest turbulent structures.

Temporally averaged field

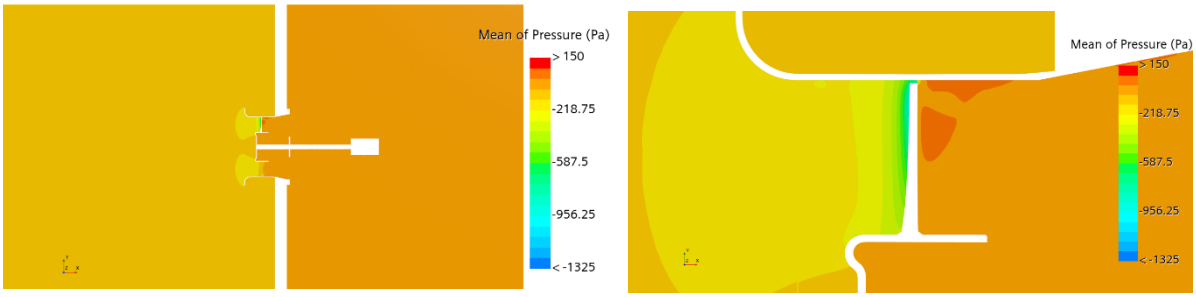

Figure 5.11: Pressure mean field

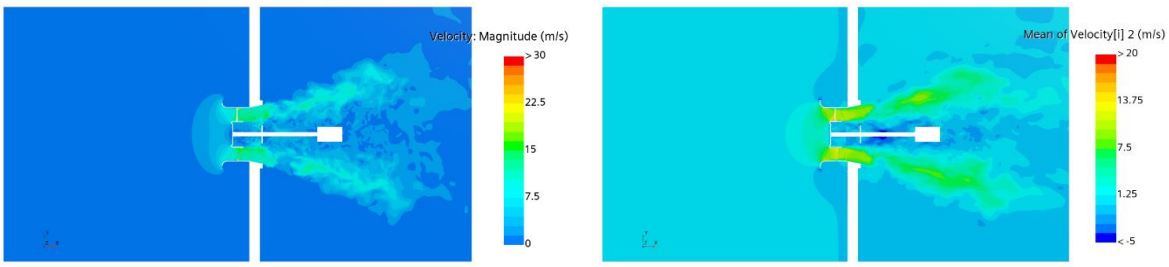

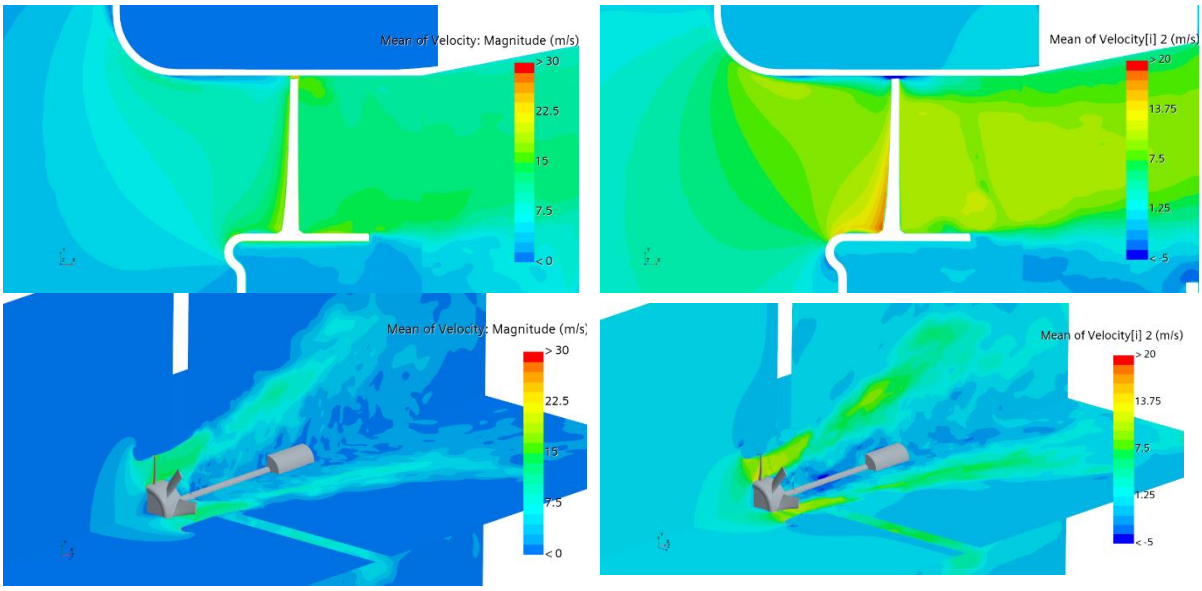

Figure 5.12: Velocity magnitude (left) and U-velocity (right) instantaneous fields

The same considerations made for the instantaneous flow remain valid.

5.3.2 FIRE M – Star-ccm+ Comparison

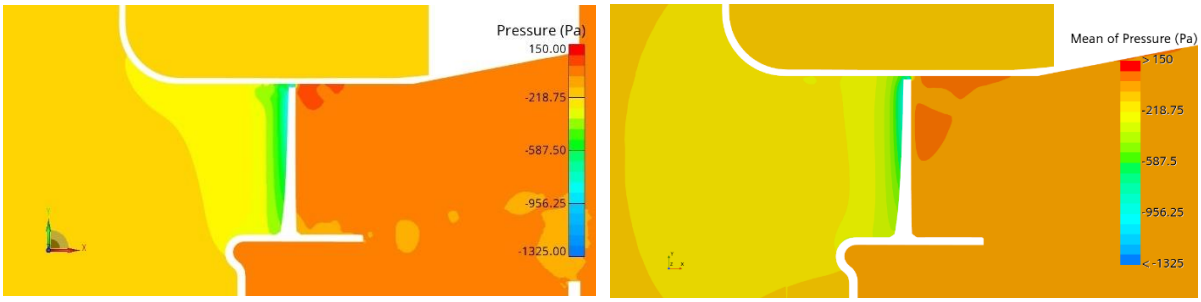

Figure 5.13: Mean pressure field (FIRE M left, Star-ccm+ right)

From *Figure 5.13* it is possible to see the similarity between the pressure field generated by FIRE M (left) and the one calculated by Star-ccm+ (right). In FIRE M, unlike Star-ccm+, the scale also allows to visualize regions of lower pressure, these are found at the interface between the flow moving at high speed and the flow coming from the center of the fan which has lower speed (see *Figure 5.14*). In this region, as well highlighted by the velocity field, there is shear flow which causes the generation of vortices and turbulence. FIRE M captures the low pressure due to the presence of these vortices.

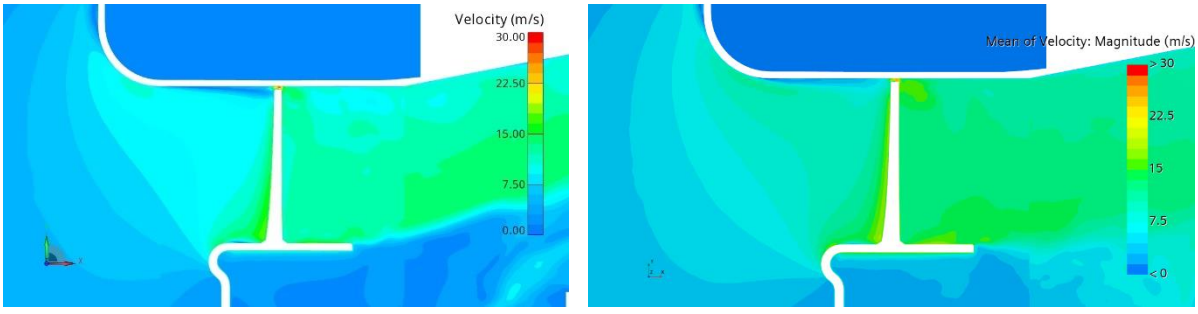

Figure 5.14: Mean velocity magnitude field (FIRE M left, Star-ccm+ right)

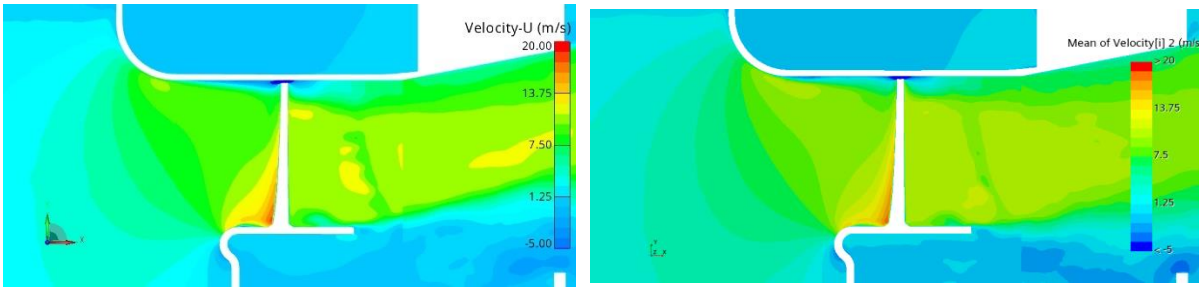

Figure 5.15: Mean U-velocity field (FIRE M left, Star-ccm+ right)

The similarity between the two flows is observed, they are almost identical from the flow acceleration zone to the wake. It is possible to notice the jump in the fluid dynamic quantities at the interface. The calculator will have to ensure that the disturbances generated by these gradients will not propagate in the domain so that they do not cause instability and do not pollute the solution.

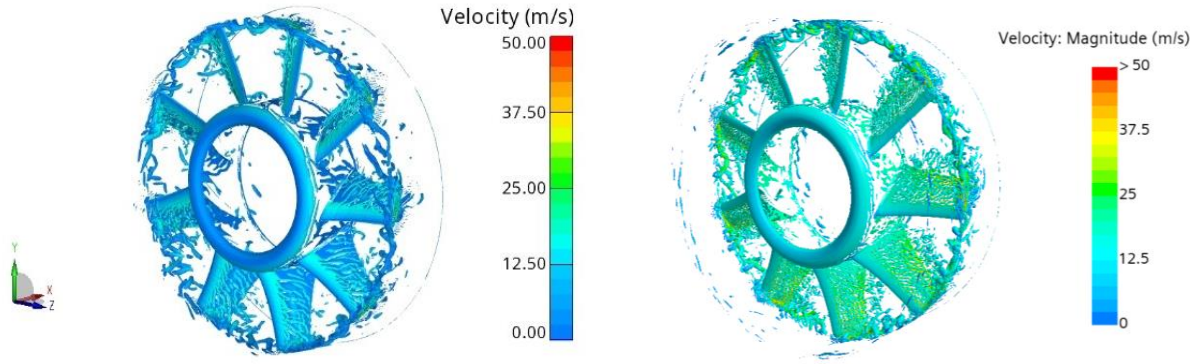

Figure 5.16: Q-criterion 2e6 (FIRE M left, Star-ccm+ right)

The Q-criterion is a tool for visualizing the coherent vortical structures of turbulence, Q is defined as the second invariant of the velocity gradient tensor:

$$Q = \frac{1}{2}(|\Omega|^2 - |S|^2) \qquad (5.4)$$

From this formula, it is possible to see that positive values of Q are indicative of areas in the flow-field where the vorticity dominates, and negative values of Q are indicative of strain rate or viscous stress dominated areas [23].
Although the general surface is roughly the same, the shape of the smaller structures as well as the magnitude of the velocity are different. Star-ccm+ resolves smaller structures and has an average higher speed value.
The different velocity value is probably due to the different model adopted in the calculation of the subgrid stresses, Star-ccm+ uses WALE and FIRE M uses CSM.

The mean flow looks very similar with the exception of the far field wake that in Star-ccm+ is more developed and compact opposed to FIRE M where it tends to develop outside, for this reason it was not included in the images.
The reason for the difference in the wakes is under investigation by the FIRE M development team, but it is not important for the purposes of the aeroacoustic investigation since, in the region used for the calculation of the source terms in FIRE M, the results are consistent with Star-ccm+.

5.3.3 Performance parameters

In this section the focus will be on the performance parameters which are mass flow, pressure rise total-to-static, thrust and torque.

Table 5-3: Performance parameters

		FIRE M	Star-ccm+
Volumetric Mass Flow	[m^3/s]	1.4	1.4
Δp total-to-static	[Pa]	120	136
Thrust	[N]	33.5	32.5
Torque	[Nm]	2.3	2.31

The experimental values of Thrust and Torque were not known, while the measured total to static pressure difference is equal to 126.5 Pa, which differs from the design pressure rise of 150 Pa.
The thrust, the torque and mass flow values are consistent between the two software. Due to the lack of information regarding the total pressure sensor position, the total pressure value was taken at the outlet and is equal to 0 Pa in both software, it is possible to conclude that the most important value for the calculation of the pressure rise is the static pressure at the inlet.
This value changes considerably depending on the position at which it is taken. In *Table 5-3* the same position of the probes used in the experimental setup is used, but approaching the fan inlet the pressure value increases considerably, reaching 140-150 Pa right at the nozzle, up to 180 Pa in the constant section of the duct. It is possible that the design point takes into consideration the pressure calculated at the nozzle's inlet.
In general, there is a good consistency between the values produced by FIRE M and those produced by Star-ccm+.

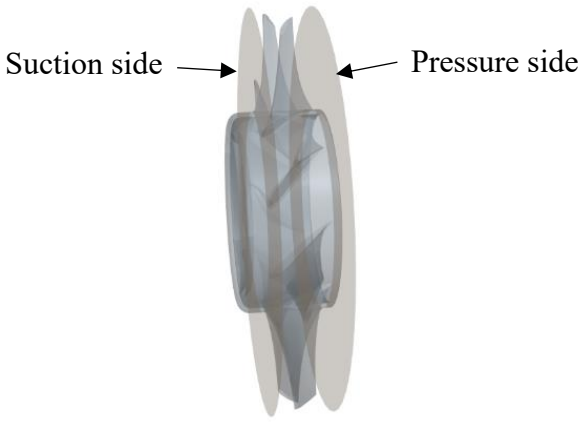

Figure 5.17: Pressure and Suction side positions

In the following section, the velocity and pressure profiles will be studied in two planes located in correspondence with the axial coordinate of the start and end of the blade (*Figure 5.17).* These sections are called suction side and pressure side.

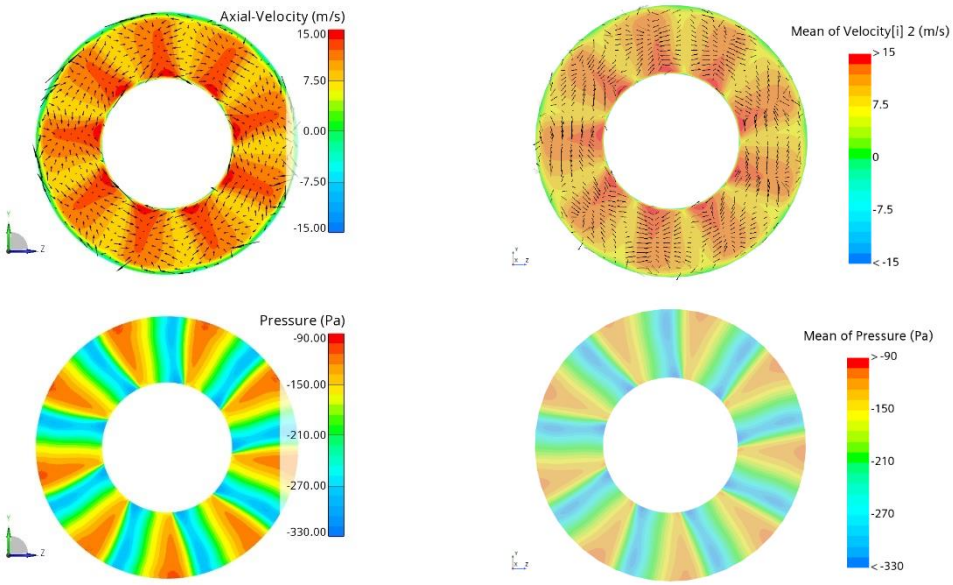

Figure 5.18: Performance Parameters: Suction Side (FIRE M left, Star-ccm+ right)

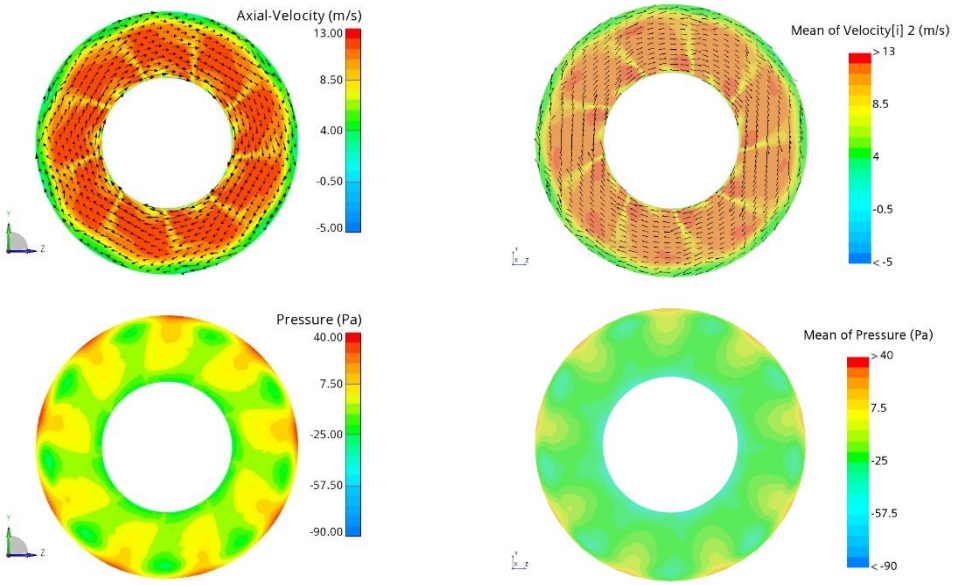

Figure 5.19: Performance Parameters: Pressure Side (FIRE M left, Star-ccm+ right)

In *Figure 5.18* and *Figure 5.19,* the contours of the mean meridional velocity and mean pressure distributions in correspondence with the suction and pressure sides, positioned as in *Figure 5.17,* are shown.
Once again, the consistency between the results of the two software is highlighted.
The flow acceleration zones at the leading edge, characterized by a low-pressure value and a high axial velocity value, are also visible. From the planar velocity vectors in the YZ plane it is possible to follow the three-dimensional movement of the flow, the displayed velocity vectors range from 0 to 3 m/s in the suction side and from 0 to 20 m/s in the pressure side. It is possible to see how, in the suction side, the flow is sucked towards the leading edge at around 50% of the blade radius, while in the pressure side the flow has a strong rotational component. From the contours in the pressure-side it is possible to notice the blade's wake and the vortices originating from the tip of the blade characterized by a lower velocity and pressure.

Figure 5.20: Line probes position for estimation of Axial velocity along the blade radius (FIRE M left, Star-ccm+ right)

In Figure 5.21, the mean meridional velocity distribution along the radius of the duct, calculated on the probe points shown in *Figure 5.20,* can be observed. As regards the suction-side, the flow accelerates in correspondence with the leading edge of the blade and then decreases following the radial coordinate. On the pressure side however, it remains mainly constant except near the walls where it tends to reach wall speed zero.
Having observed the exit speed profile, it is expected that the maximum speed is reached at 50% of the blade radius near the leading edge in the acceleration zone, where the YZ speed vectors on the suction side converge. The graph does not show this trend because the blade is tilted at an angle relative to the monitoring points, so the maximum velocity value is where the points are near the leading edge.
The speed profiles of FIRE M and Star-ccm+ are comparable. The speed profile on the pressure side is identical. Instead, on the suction side, FIRE M presents a flatter profile while Star-ccm+ shows greater variations in correspondence with the hub and a greater deceleration of the flow as the radius increases.

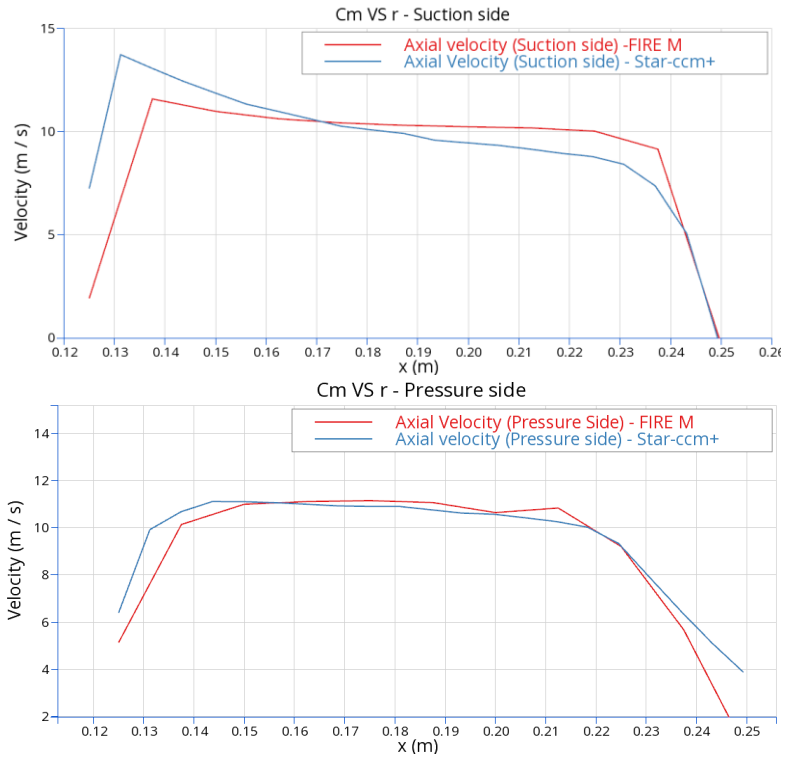

Figure 5.21: Axial velocity along the blade radius in the Suction side (top) and Pressure side (bottom)

In *Figure 5.22* it is possible to compare the results of the power spectral density calculated on the hydrodynamic pressure fluctuations, in a monitoring point located on the external case in correspondence with the point where the tip of the blade passes, in the same time interval. It is still observable that there is a good consistency between the results of FIRE M and Star-ccm+ which are practically identical.

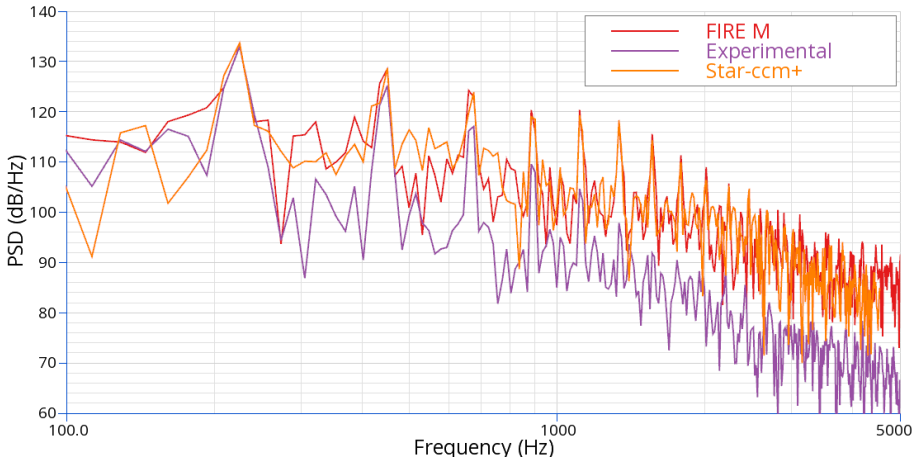

Figure 5.22: PSD of hydrodynamic pressure fluctuations on far-field microphone 4

5.3.4 Convergence

To verify the convergence status of the simulations, the focus is directed onto the values of the performance parameters. And it is noticed that all the results settle within 0.1 s as seen in *Figure 5.23*.
It can be stated with high confidence that upon activation of the aeroacoustic models the simulation has reached convergence in the area of interest.

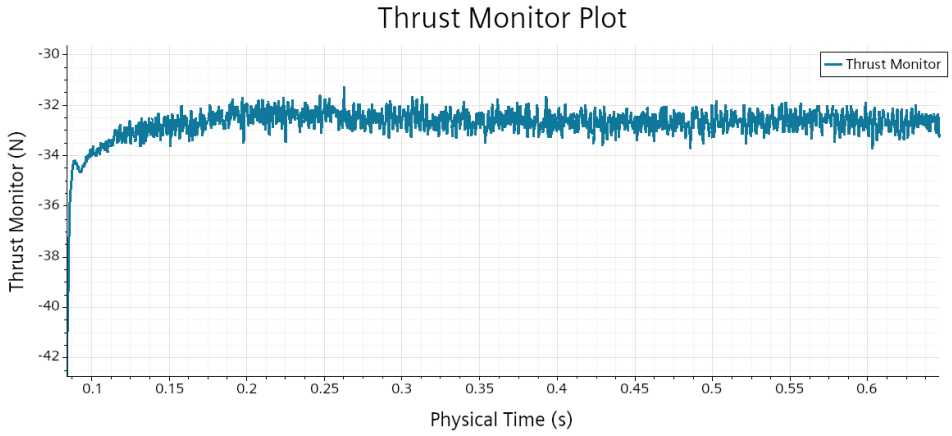

Figure 5.23: Star-ccm+ thrust graph on the fan surface

Chapter 6: Computational Aeroacustics

Aeroacoustic simulation is a crucial field for understanding and predicting noise generated by moving objects. In this chapter, the results obtained from the computational analysis will be reviewed and the main findings related to sound propagation from an aerodynamic source will be presented.
The model chosen for the CAA simulation is the Perturbed Convective Wave Equation model (PCWE) but, the results obtained through Star-ccm+'s broadband models for steady-state RANS and the spectrum resulting from the pressure fluctuations calculated from the CFD simulation will also be briefly illustrated.
The goal of our analysis is to be able to capture the two broader peaks of the spectrum caused by blade-wake interactions, and the blade passing frequency and its harmonics shown in *Figure 4.5*.
In order to capture the pressure variations corresponding to the position of the microphones, monitoring points are created in both software: 7 far-field microphones and 15 wall pressure sensors are positioned like in Figure 6.1 following the experimental setup layout.

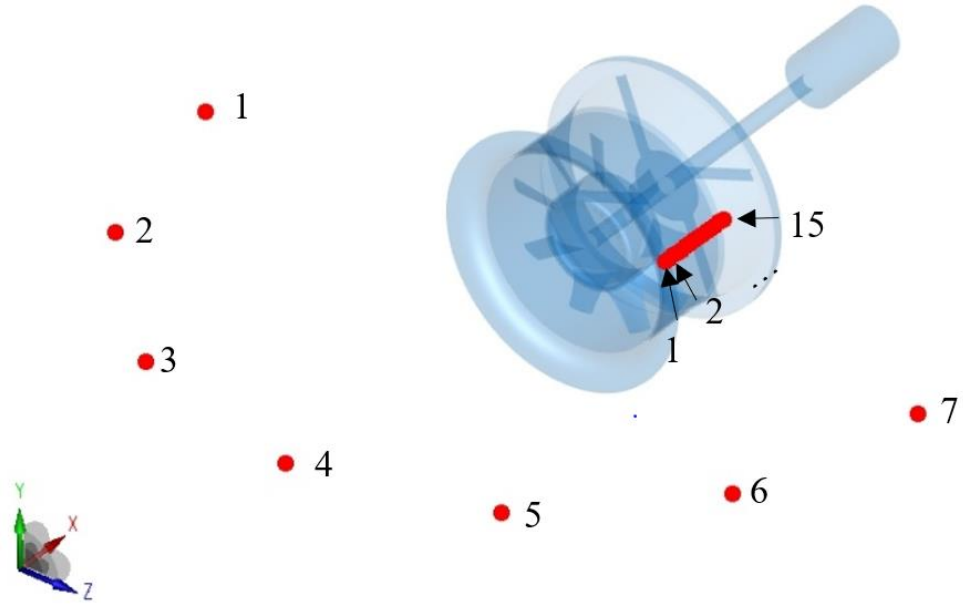

Figure 6.1: Far-field microphones and wall pressure sensors

6.1 Star-ccm+: Aeroacustic simulation setup

In Star-ccm+ the activation of the aeroacoustic perturbed convective wave model is very straightforward: it is sufficient to activate the model in the *Continua*, set some parameters shown in *Table 6-1* , and finally select the type of boundary conditions for dealing with the acoustic wave propagation.

Table 6-1: PCWE parameters

Reference speed of sound	332 m/s
Implicit solver: max number of iterations	20
PCWE solver: max number of iterations	10
Newmark Alpha Parameter	-1/3
Convergence Tolerance	1e-5

In Star-ccm+ the mesh used for the CAA simulation is the same as the one used for the CFD simulation.
To maintain the accuracy of the acoustic predictions, it is advised by the PCWE guidelines [9] to apply a criterion for points per wavelength (PPW) when generating the mesh.
PPW is defined as:

$$\mathrm{PPW}_{\Delta} = \frac{c/f}{\Delta x}, \qquad (6.1)$$

where c is the speed of sound and f is the highest frequency of the waves that the mesh is able to capture. The recommended PPW for a simulation using the Perturbed Convective Wave model is $PPW \geq 15$.
The same criterion applies for the time step:

$$\mathrm{PPW}_{t} = \frac{1/f}{\Delta t}. \qquad (6.2)$$

With a Δt of $1.1216 \cdot 10^{-6}$ it is possible to resolve up to 54 kHz, so the most restrictive parameter is the PPW_{Δ} calculated on the mesh.
Following the PPW_{Δ} criterion, the mesh should be able to capture up to 11 kHz in the wall pressure sensor region, where the cell size is 2mm, and up to 1 kHz in the far field microphone area, where the mesh size is 2cm. This should be sufficient to capture the blade passing frequency and the noise caused by wake-blade interaction.
From the PCWE guidelines it is also advisable to set Newmark alpha parameter equal to -1/3 in the case of rotating geometries.

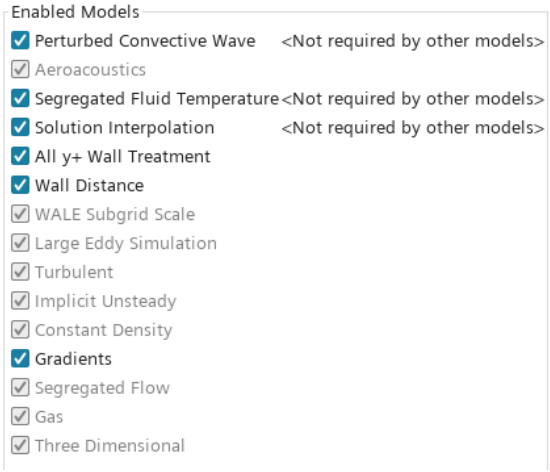

Figure 6.2: Star-ccm+ Aeroacustic model

6.1.1 Boundary conditions

When performing acoustic analysis over a restricted domain, acoustic waves may reflect off at the ends of the fluid domain, causing sound measurements to be artificially affected.
For this reason, particular attention must be paid to the definition of boundary conditions. Star-ccm+ automatically assigns the non-reflection condition in correspondence with mass flow inlet and pressure outlet, while a reflection condition is imposed on solid walls. Therefore, all that remains to be defined is the non-reflexivity condition on the symmetry boundaries.
As the name suggests, if the non-reflecting option is activated, then the solver dampens the acoustic potential on the surface, ensuring that no acoustic waves are reflected by the fluid boundaries.

6.2 Star-ccm+: Results

In this section the aeroacoustic results obtained by Star-ccm+ will be discussed.

6.2.1 Broadband model

An introduction to broadband models was carried out in *Chapter 3.3.1*, below the results of Curle surface acoustic power, Proudman acoustic power and mesh frequency cutoff will be illustrated.
These results are taken after 11k iterations from the steady-state RANS simulation used to initialize the flow field.

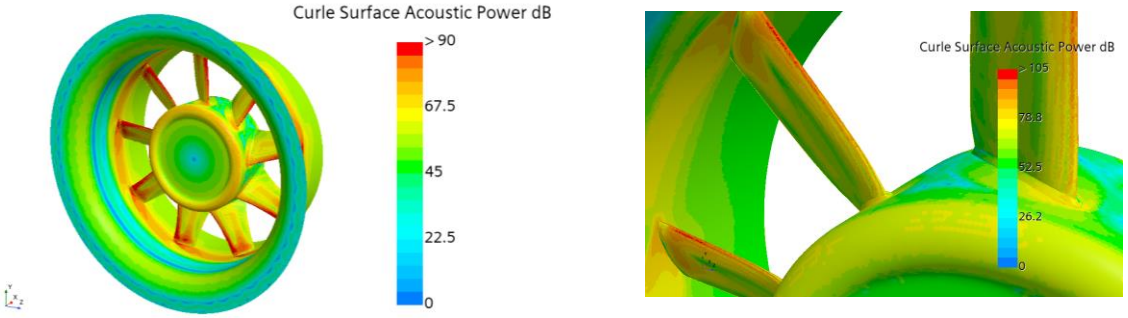

Figure 6.3: Curle surface acoustic power

The Curle acoustic power model, which assumes an isotropic turbulent flow field, computes the sound that dipole sources generate. This model therefore represents the fluctuating surface pressure with which the solid boundary acts on the flow. The plot displays the noise level that the turbulent boundary layer emits over a surface at low Mach number.
The noise sources are mainly located around the leading edge and around the blade tip. The maximum surface acoustic power value reached by the fan is 121 dB with 100 dB being the prevailing value around the blade's leading edge and 90 dB being the value at the blade tip.

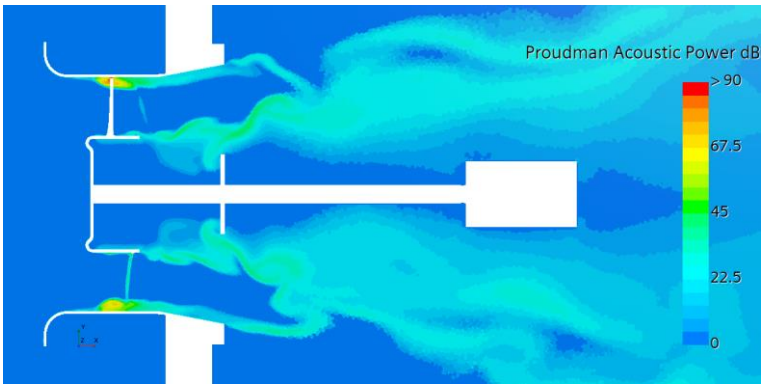

Figure 6.4: Proudman acoustic power

The Proudman acoustic power (in dB) estimates the local contribution of the quadrupole sources as generated by isotropic turbulence. It displays the acoustic power per unit volume as emitted by the turbulence structures generated by the fan.
It is observable again that the location where the acoustic power has the highest value is around the tip of the blade. The maximum value of acoustic power is 96 dB at the tip. This is the region where the backflow occurs and the tip vortices are created, it is precisely these vortices that represent the most important source of noise.

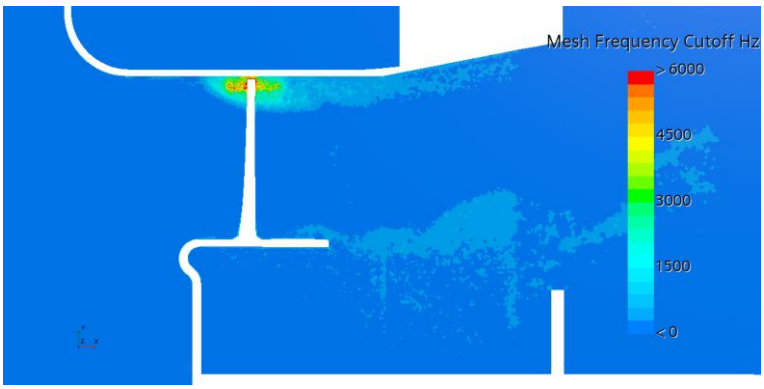

Figure 6.5: Mesh frequency cutoff

The mesh frequency cutoff analysis allows to determine whether the grid used has sufficient resolution to capture the turbulent structures in the frequency range of interest.
In the region where the most important noise sources are expected to be located, the mesh should be able to capture the noise generated by turbulence with frequencies up to 3000 Hz. The same function, in correspondence with the far field microphones, is equal to zero, but this only means that those microphones would not be able to capture the noise due to the turbulence generated in this case by the RANS model, but the acoustic waves can very well propagate from the fan, up to the listening points. As regards the wall pressure sensors, it is expected that those located in correspondence with the areas where the mesh frequency cutoff value is higher, are able to capture noise in a larger frequency range.

The results of the broadband model should not be taken as exact but merely indicative of the position of the main noise sources and the mesh's ability to capture them.

6.2.2 CFD results

In the simulation performed in this analysis, being the density constant, is not possible for the hydrodynamic pressure waves to propagate.

But, as shown below, it is still possible to gain some information from the hydrodynamic incompressible pressure.
The field function *pressure_fluctuation* is defined as $p' = p - \langle p \rangle$. With $\langle p \rangle$ being the mean pressure.
From *Figure 6.6* it is possible to see that there are no pressure waves in the inlet region, this is because the pressure fluctuations showed are hydraulic pressure fluctuations due to turbulence which are convected with approximately the mean velocity, so they can't be transported upstream. For this same reason, the spectra of the pressure signal at the far-field microphones locations appears to be flat, no signal reaches the far-field field.

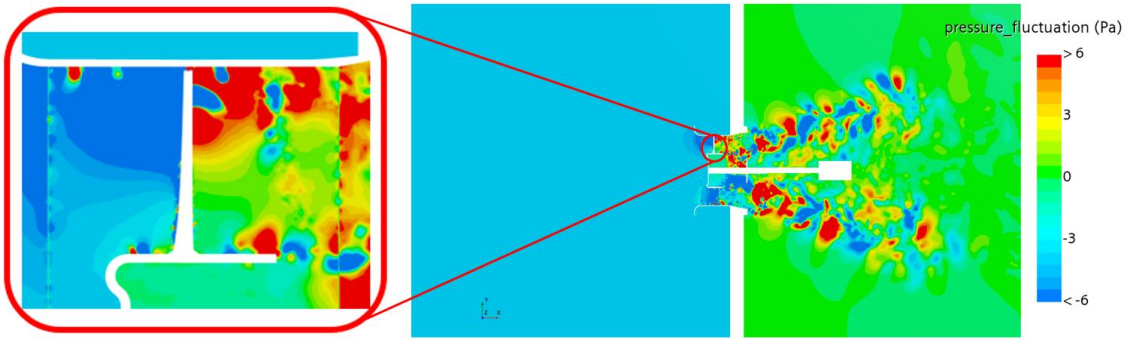

Figure 6.6: CFD pressure fluctuations

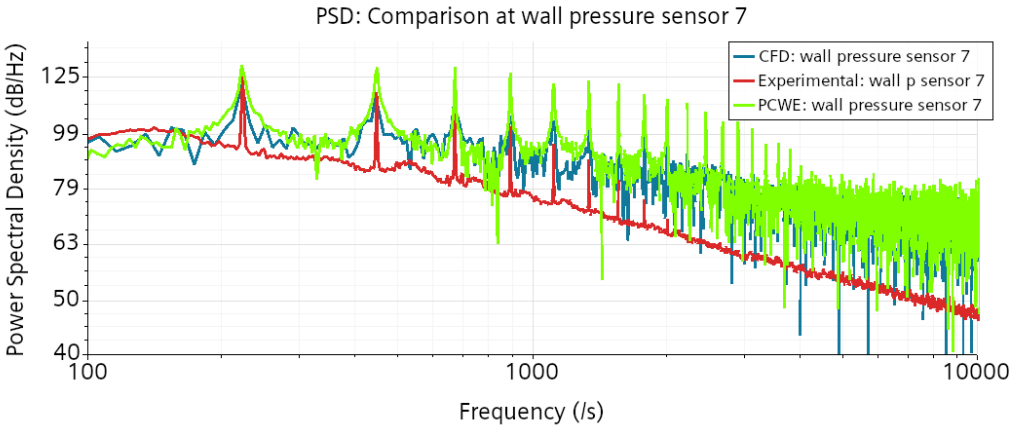

Figure 6.7: PSD Experimental data VS CFD

In the near region of a sound source, the hydrodynamic component dominates over the acoustic component at most frequencies. This is because in the near field, the pressure fluctuations (together with the velocity field) make up the local hydrodynamic flow. This is why, in the near field, the hydrodynamic pressure contribute can be higher than the acoustic one. However, moving away from the source, the hydrodynamic pressure fluctuations decrease dramatically while the acoustic counterparts decay slowly. This demonstrates that the hydrodynamic pressure fluctuations do not propagate, and that the acoustic fluctuations are the only ones to propagate to the far field [24].
Therefore, as shown by *Figure 6.7*, the CFD simulation is able to capture the blade passing frequency and its harmonics with excellent precision, up to the 9th harmonic, in correspondence with the wall pressure sensor 7.
From 2000 Hz onwards, the remaining spectrum is made up of broadband noise, in line with what was predicted by the mesh frequency cutoff analysis.
Wall pressure sensor 7 is located precisely in the region that in *Chapter 6.2.3* was identified as the one with the best capacity to capture the highest frequencies thanks to its mesh refinement.

The Power spectral density value of the first Blade Passing Frequency is 121 dB.
Figure 6.8 shows that the sensors furthest from the source are unable to capture the harmonics of order 2 and higher, this proves what was stated previously about the inability of hydrodynamic fluctuations to propagate away from the source. The only sensor that has high accuracy is wall pressure sensor 7 which is located in close proximity to the acoustic source.

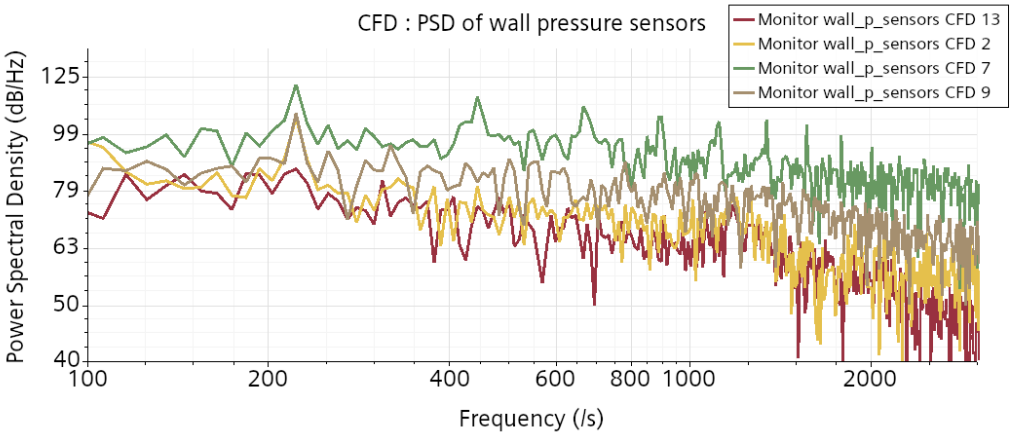

Figure 6.8: PSD of wall pressure sensors 2, 7, 9, 13

6.2.3 Perturbed convective wave

In this section the results of the simulation performed with the perturbed convective wave equation model will be discussed.

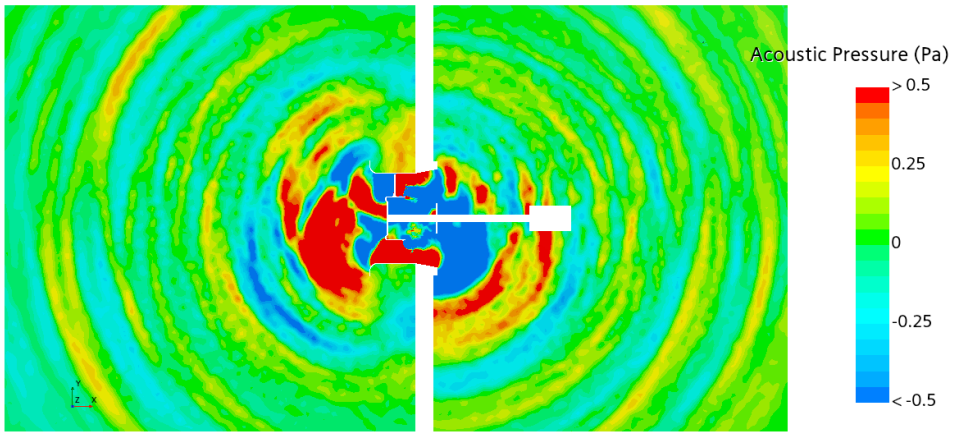

Figure 6.9: Acoustic pressure waves

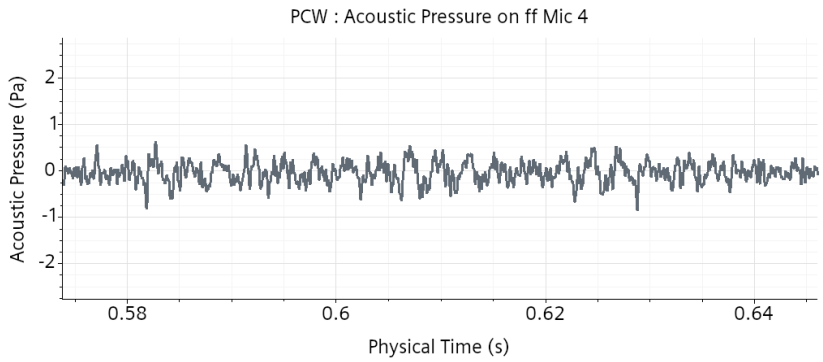

Figure 6.10: Acoustic pressure on far-field microphone 4

It is possible to see that the entity of the acoustic pressure is very high in the close proximity of the fan and then tends to decrease with $1/r^2$, being r the distance of the wave from its source. This is due to the expansion of the spherical wavefront as the sound propagates away from the source.
The acoustic waves in the microphone area mostly oscillate between -0.5 Pa and 0.5 Pa as shown by *Figure 6.10*.

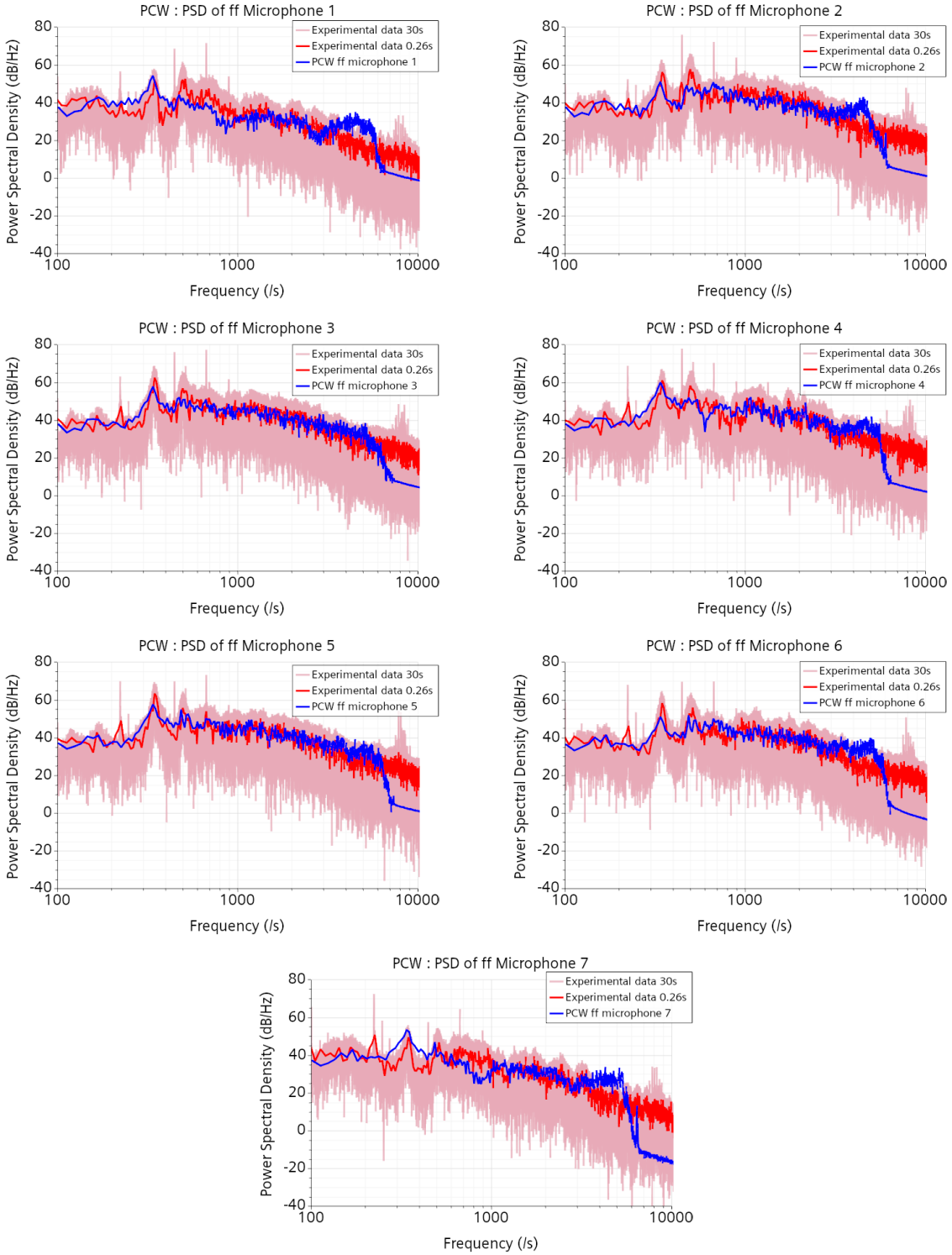

Figure 6.11: PSD of acoustic pressure on far-field microphones 1 to 7

In *Figure 6.11* the PSD values can be observed for the 7 far-field microphones: in pink the values derived from the experimental data for a total signal duration of 30 seconds, calculated through the point-time Fourier transform function of Star-ccm+, with 1 analysis block and overlap factor equal to 0; in red the values deriving from the experimental data, calculated at the same time interval as the aeroacoustic simulation, with analysis block set equal to 2 and overlap factor equal to 0.5; finally, in blue the values deriving from the PCWE with again 2 analysis blocks and overlap factor equal to 0.5.
If the number of analysis blocks is set to 1, the full signal is accounted for the computation of the FFT, else if the number of analysis blocks is set to $n > 1$ signal is subdivided into n parts of equal time length, the FFT is then computed for each signal fragment and the final FFT is obtained through an averaging process. By increasing the number of analysis blocks, a smoother spectrum can be obtained, but the minimum frequency resolution will be decreased since the number of samples of the signals associated with each block is lower if compared to the full signal. However, the number of the Analysis Blocks can also be increased without reducing the length of the associated signal fragments. This can be obtained by using an Overlap Factor different from zero, which is usually recommended. Usually, it is advisable to compare the SPL with the same frequency resolution, otherwise the comparison would be meaningless [25].
However, in this particular scenario, presenting the experimental data within a single Analysis block provides us with an understanding of the expected range for these values.
Looking at *Figure 6.11* it is possible to see that the first blade passing frequency is not captured, the simulation time is too little to be able to capture this information as shown by the red curve. But the first broad peak of the spectrum, which is probably caused by the turbulent structures originating near the tip of the blade, is well reproduced. The second peak is slightly recorded by microphone number 5. A timid attempt to capture the second peak is carried out by microphones 4, 6, 7 but is not well distinguishable by the broadband noise.
Above 600 Hz the spectrum consists of broadband noise which is contained inside the pink curve. Above 6000 Hz there is a drop in PCW predictions probably given by the mesh resolution not able to resolve the higher frequencies.

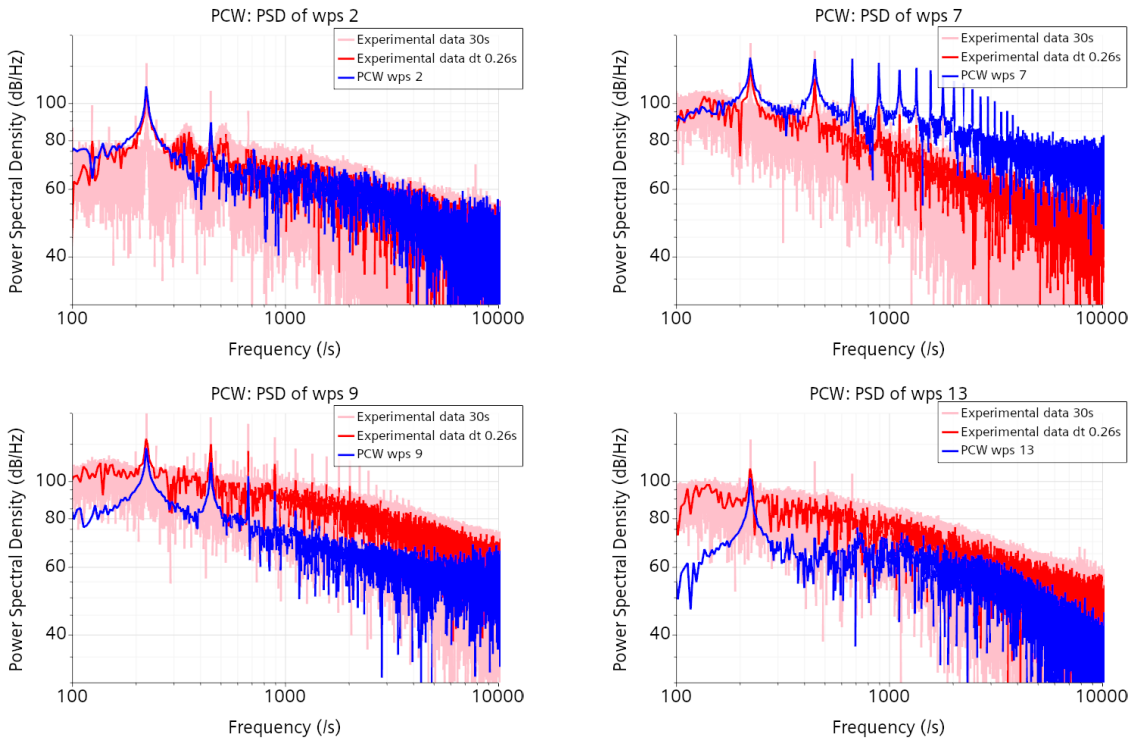

Figure 6.12: PSD of acoustic pressure on wall pressure sensors 2, 7, 9, 13

In *Figure 6.11* the PSD values can be observed for wall pressure sensor number 2, 7, 9, 13: in pink, the values derived from the experimental data for a total signal duration of 30 seconds; in red, the values derived from the experimental data, calculated at the same time interval as the aeroacoustic simulation; in blue, the values deriving from the PCWE. All data are captured with 1 analysis block and overlap factor 0.
From the wall pressure sensors, as stated in *chapter 6.2.2,* it is possible to gain information about the blade passing frequency, which is perfectly reproduced. With the first BPF being at 223 Hz and its harmonics nicely shown by sensor 7 and 9. Differently from the CFD, the PCW model is able to get information on the blade passing frequency also away from the source because the acoustic waves propagate in the whole domain while the hydrodynamic pressure can only be transported by the current. It is shown that the amplitude is a bit underestimated, this is probably due to too little simulation time, because the experimental data taken at the same intervals have the peaks at approximately the same height.

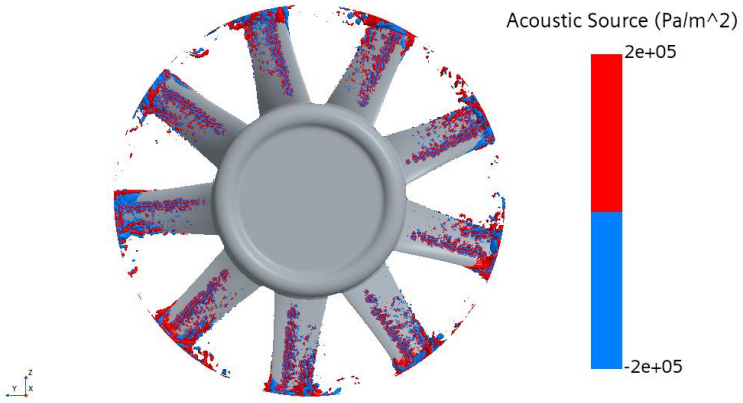

Figure 6.13: Isosurfaces of acoustic sources of the PCWE at an instantaneous time

In *Figure 6.13* the perturbed convective wave equation acoustic source is shown, this corresponds to the right end side of the equation and is computed as: $-\frac{1}{\rho c_0^2}\frac{Dp_{ic}}{Dt}$.
From this image, it is possible to have a more complete picture of the position of the noise sources.
It is possible to note that the most important sources are found at the tip of the blade, in the trailing edge, in the acceleration region and in the region in which the blade interacts with the blade tip vortex of the one preceding it. The strongest sources are expected to give rise to the blade passing frequency, which constitutes the tonal noise component of the considered fan. The two broader peaks could possibly be originated near the blade tip wake, where the rapid changes in pressure, due to the assembly and disassembly of the vortices, typically give rise to noise and it can happen that, if the bigger vortices have a not-too-random behavior that repeats itself, this could originate the two broader peaks found in the spectrum at low frequency.
It is possible to hypothesize that the region where the largest turbulent vortices are found and also subject to a certain periodicity, is in correspondence to where the next blade hits the detachment vortex from the previous one. To prove what has been said, it would be necessary to carry out a spectral analysis of the source term.

6.3 FIRE M: Aeroacustic workflow

As anticipated in the *Chapter 4.3.1* the aeroacoustic workflow of FIRE M in combination with OpenCFS consists of a series of actions that can be briefly summarized in a few steps:

- creation of the acoustic mesh and format conversion via app.
- mapping of results on the acoustic mesh.
- calculation of the PCWE source term and writing of the *.xml* files used by OpenCFS to perform the simulation via app.
- OpenCFS simulation.
- Postprocessing.

6.3.1 Aeroacustic mesh

The main idea as well as the objective of the workflow is to map the quantities of interest onto the acoustic mesh and then run the simulation with the perturbed convective wave model in the open-source program OpenCFS.
Since, just like in Star-ccm+, in OpenCFS it is possible to define boundary conditions that avoid the formation of reflections by waves incident on fluid surfaces, it is possible to reduce the size of the aeroacoustic mesh to the region of interest. In this way the computational cost is significantly reduced.

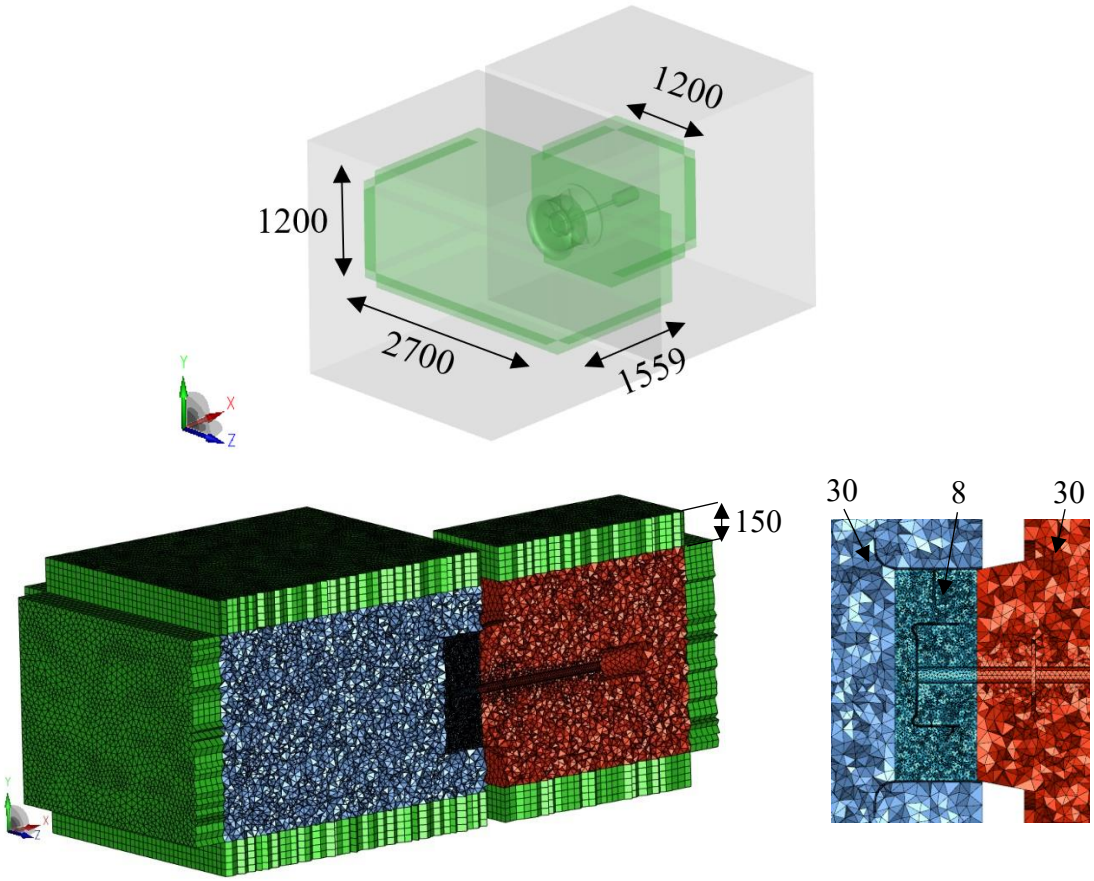

Figure 6.14: Aeroacoustic mesh

From *Figure 6.14* it is possible to view the 3 domains: *DOM_Fan*, *DOM_In* and *DOM_Out,* which together make up *DOM_1_Fluid* and the external region, in green, correspond to the perfectly matched layer (PML).
In this last region, damping functions are applied which eliminate the acoustic waves, avoiding reflection phenomena.
In OpenCFS, the non-reflectivity of waves incident on surfaces can be managed in two ways: through the application of a perfectly matched layer (PML) or through the application of an absorbing boundary condition (ABC). The latter is effective when there are orthogonally impinging waves since, being composed only of superficial elements, it has a low computational cost, PML is always effective but has a higher computational cost.
The PML is chosen instead of an absorbing boundary condition because, having carried out a reduction in the volume, it is expected that the incident wave condition parallel to the surface required by the ABC will not be respected. The OpenCFS documentation [26] recommends using 4 layers.

Mesh converter App

FIRE M mesh is stored in *.flm2* format while OpenCFS requires a *.cfs* mesh file in order to work. For this reason, during the course of this thesis, a Python script that converts the mesh from one format to another has been developed.
In *Figure 6.17.b* it is possible to see the structure of the *.cfs* file after the conversion.
An *.hdf5* or *.cfs* file [27] is made of groups and subgroups which can contain datasets and can have attributes. The acoustic mesh file is made of 2 major groups, which are *Mesh* and *Results*. *Mesh* contains all the information regarding the mesh such as cell and node position (see *Figure 6.16*), the connectivity matrix, which defines how the cells are communicating with each other, and the nodes and elements defining each boundary and volumetric region in the computational domain. The *Results* group contains information about the fluid dynamic quantity associated with each cell at each time-step.

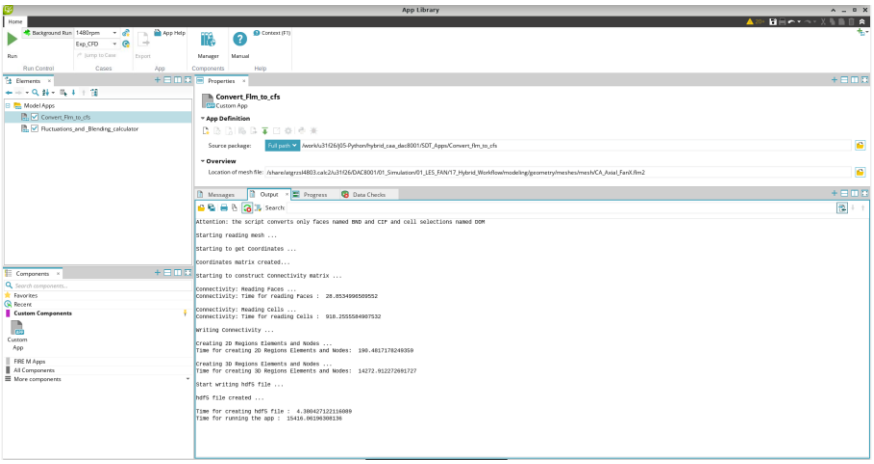

Figure 6.15: Mesh converter app - user interface

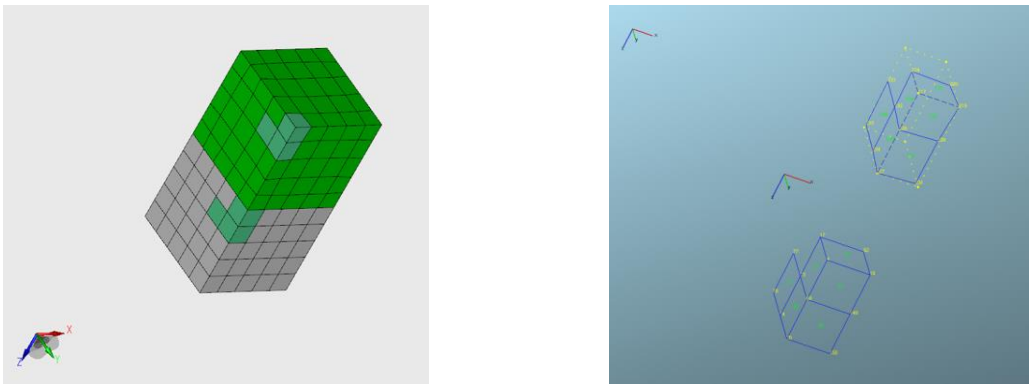

Figure 6.16: Example of cell number and node number

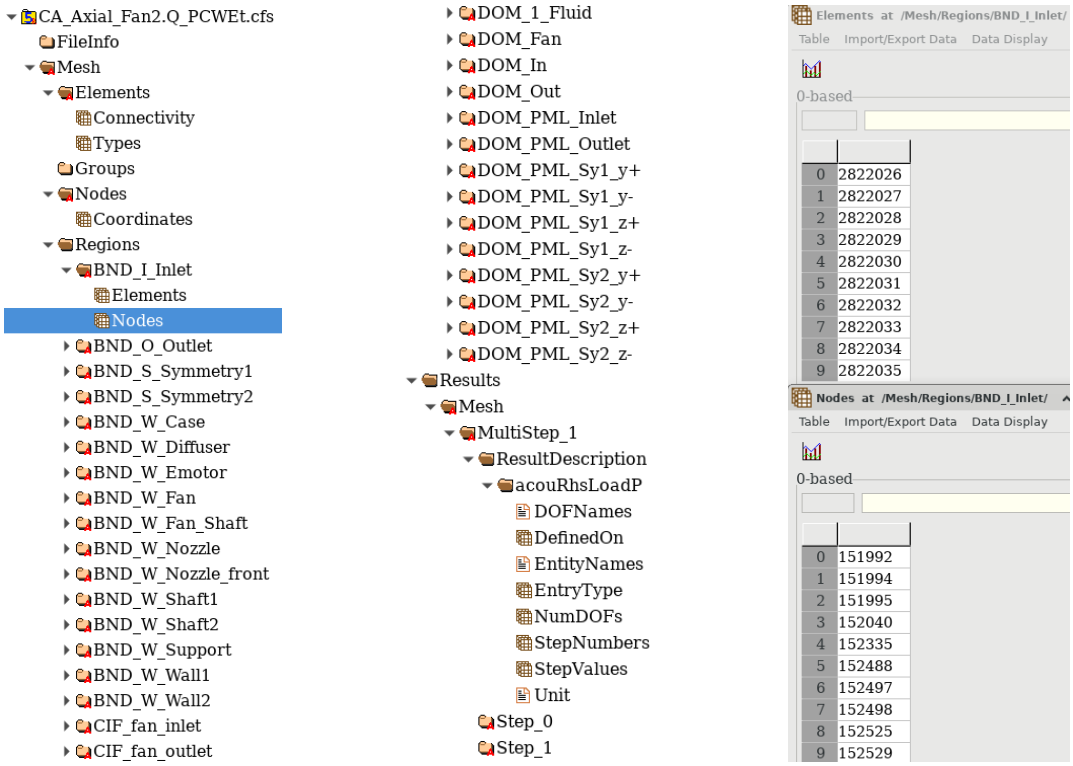

Figure 6.17: cfs mesh file structure displayed with hdfview [28]

6.3.2 Mapping

Through interpolation procedures explained in literature [10], during the simulation the program is capable of mapping the quantities of interest onto the acoustic mesh.
In *Figure 6.18* the mapped values of relative pressure on the acoustic mesh are shown.
It is important to notice that in OpenCFS only the rotating region will be set as the source region, so it is in this region that a good mapping of the quantities is needed.

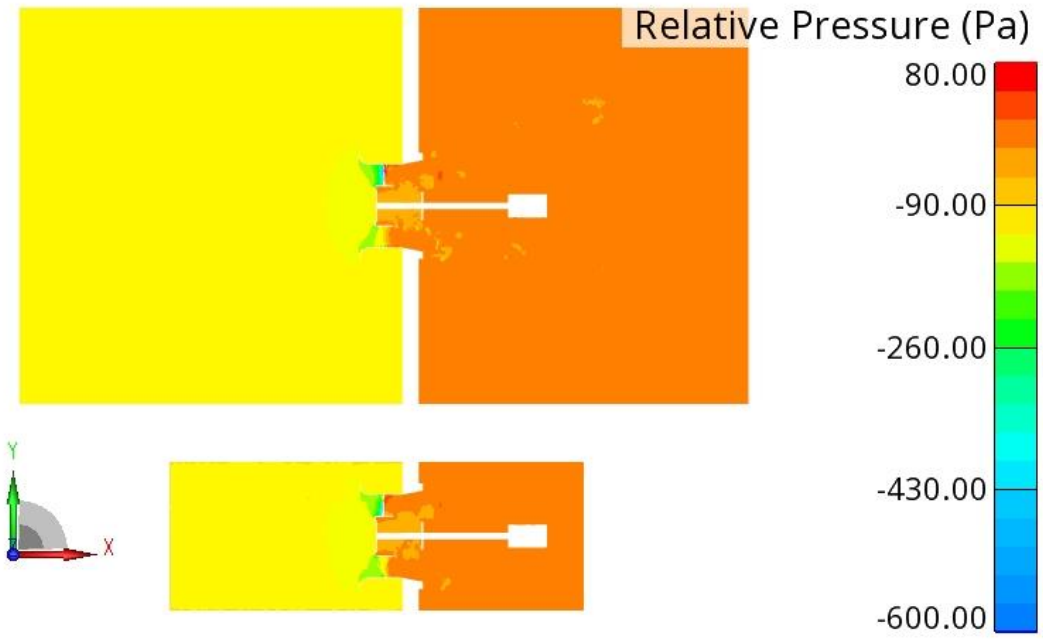

Figure 6.18: Pressure on the CFD mesh (top) and mapped pressure on the acoustic mesh (bottom)

From the mapped pressure it is possible to calculate the source term of the perturbed convective wave equation model.
Strictly speaking, the right-hand side of the equation consists in the material derivative of the incompressible pressure, but as studied in [10], it is shown that the convective part of the equation can be ignored without causing any loss of important information.
Therefore, through the use of another app, also developed during this thesis using Python, the source terms that OpenCFS uses as inputs are calculated. Through the application visible in *Figure 6.19* it is possible to define a set of parameters such as sound speed, reset average quantities (which defines the time instant at which to start calculating the average values) and the blending duration, which indicates the number of time steps to which to apply the blending function assigned below. It is also possible not to assign blending by leaving this value equal to zero. In the section below, the *Case_set* and *Case* from which to take the files written during the mapping phase, must be selected. Finally, it is possible to choose the acoustic model and the type of blending function between sin^2, e and e^2 see *Figure 6.20*. The Custom Factor is by default set as $1/\rho c_0^2$ to reflect the factor present in front of the right end side of the equation but it is also possible to set it equal to 1 to obtain the pure values of the time derivative as outputs.

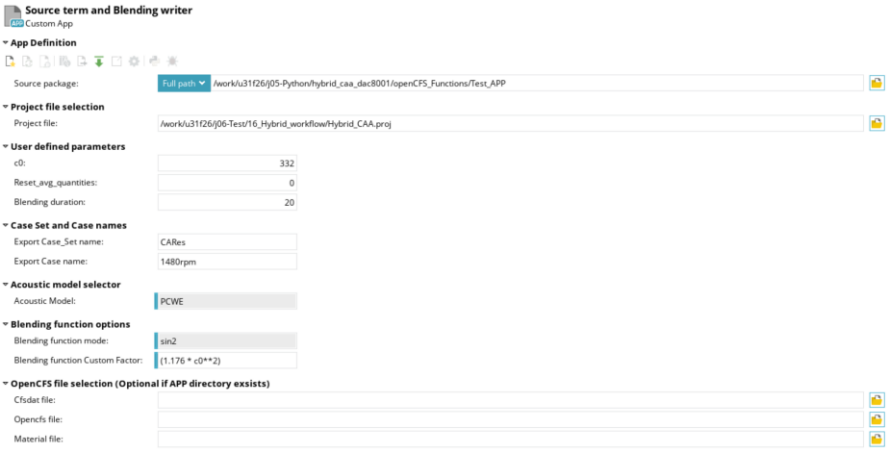

Figure 6.19: Source term and blending application

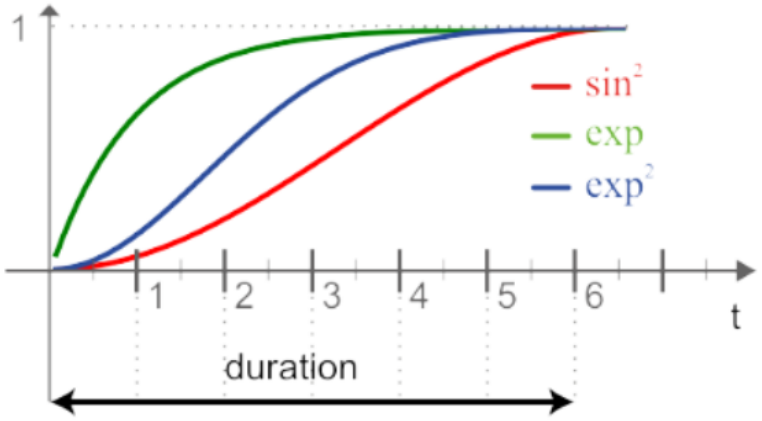

Figure 6.20: Blending functions implemented via app [29]

6.3.3 OpenCFS

OpenCFS (Coupled Field Simulation) is a finite element-based multi-physics modelling and simulation tool [29]. With about 20 years of research-driven development, the core of OpenCFS is used in both scientific research and industrial applications. The modelling strategy of OpenCFS focuses on physical fields and their respective couplings.
OpenCFS is free and open source under the MIT license, which means it can be used by anyone, even for commercial purposes. It offers state-of-the-art features ranging from capabilities for various physical fields and their couplings, non-conforming grid techniques, and structural optimization, to flexible data exchange with third-party software, scriptable XML input, and powerful built-in third-party libraries.
The software is quick to learn with an extensive set of examples from user documentation and an extensive test suite. Furthermore, OpenCFS is used in several university courses, and learning material is freely available.
Members range from university researchers at TU Wien, FAU Erlangen–Nuremberg, TU Graz over individuals and students to companies applying OpenCFS to industrial problems [29].

OpenCFS does not have a graphical user interface (GUI) but the parameters for the simulation are set through the use of *.xml* files.
As regards the acoustic workflow, the PCWE solver requires the source terms to be in the form of nodal loads. The CFSdat module is used to transfer values from the cell's center to the nodes. The *.xml* file used by CFSdat can be found in *Appendix A*.
In the first part the transient information such as starting time, number of steps and time interval, are passed. In the following part it is possible to choose a source mesh and a target mesh for the interpolation of the acoustic quantities. During the mapping operation all the results are mapped on a single cell selection containing all the cells: *DOM_1_Fluid*. By selecting to interpolate from *DOM_1_Fluid* to *DOM_Fan, DOM_In* and *DOM_Out,* the source term will be splitted in three different domains making it easier to define the rotating region in OpenCFS.
In the last part the name of the output file and the compression in chosen.
The interpolation type is set to conservative cell centroid. This approach conserves the energy globally but approximates the local energy conservation of the FE right-hand side by

$$F_i^a = \int_{E_a} N_i^a(\xi) f^a d\xi \approx \sum_{k \in M^f} N_i^a\left(\xi_{E_k^f}\right) F_k^f$$

where E_k^f denotes the cell of the flow grid, $\xi_{E_k^f}$ the local coordinate, M^f the number of flow cells, N_i^a the FE basis function on acoustic grid and the subscript i the node number on the CAA grid. To preserve the acoustic energy, the loads F_k^f of the fine flow grid are interpolated to the coarser acoustic grid (see *Figure 6.21*) [30].

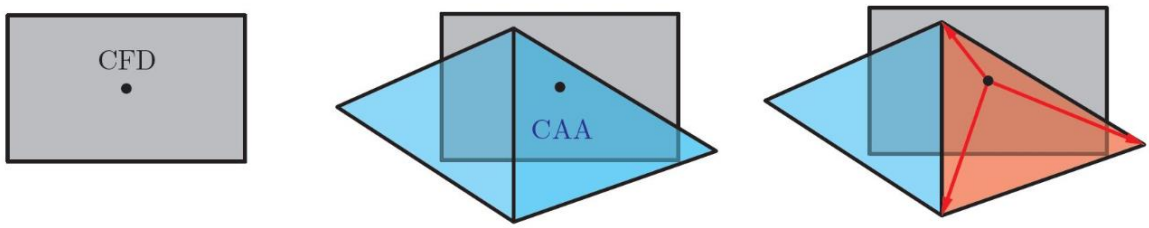

Figure 6.21: Cell centroid conservative interpolation [31]

Once the acoustic sources are interpolated, the OpenCFS simulation can be performed.
In *Appendix B* the *.xml* file used to perform the Acoustic simulation is shown. In order to perform the simulation, the CFSdat output file is used as input, subsequently the regions constituting the computational domain must be defined and a material, read from the file *mat.xml,* must be assigned to each region. Then the sliding interfaces, the position of the microphones and wall pressure sensors, the solver simulation parameters such as simulation time, time step and acoustic formulation, the definition of the PML regions, the definition of the source terms and their position and finally the outputs must be defined.
As formulation type the perturbed convective wave equation corresponds to *acouPotential*.

Blending functions

A temporal blending function is especially important for transient simulations, to smoothly introduce, at the beginning of the simulation, the source terms and avoid numerical instabilities. The spatial blending function is especially important when non-conforming interfaces are used. Directly at the non-conforming interface no source terms should be applied [16]. The chosen function for both blending was $1 - cos(x)$.

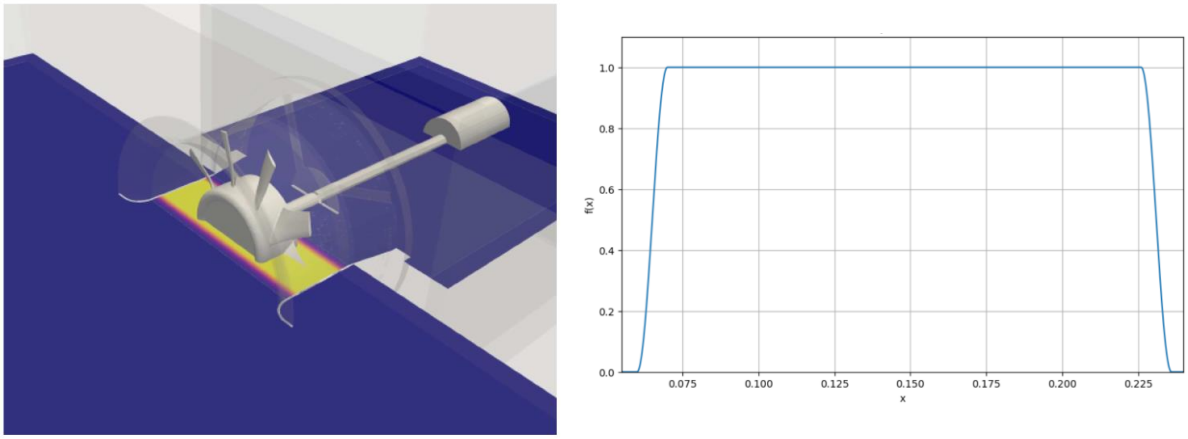

Figure 6.22: Spatial blending function

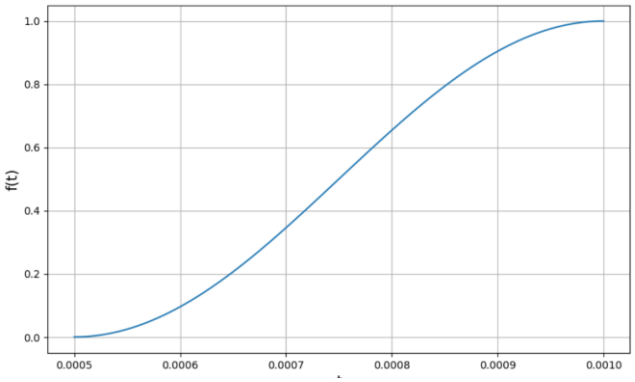

Figure 6.23: Temporal blending function

6.4 FIRE M: Partial results

Due to time constraints and low availability of the cluster due to a high workload, it was not possible to respect the same simulation parameters adopted with Star-ccm+. In order to get some results in a small amount of time, it was necessary to decrease the time step and increase the mesh size. For this reason, the comparison makes little sense. For completeness, and to demonstrate the capabilities of the FIRE M workflow, the results of the aeroacoustic simulation carried out with OpenCFS are reported.
The main differences between the software are:

- Difference in time step: $\Delta t_{\text{OpenCFS}} = 2 \cdot 10^{-5}$ s while $\Delta t_{\text{Star}} = 1.1216 \cdot 10^{-6}$ s.
- Difference in mesh-size Δ: from *Figure 5.3* and *Figure 6.14* it is possible to observe the different mesh sizes. For example, in the blade-tip region: $\Delta_{\text{OpenCFS}} = 0.5$ mm while $\Delta_{\text{Star-ccm+}} = 8$ mm.
- Difference in elements type: in the mesh used by Star-ccm+ polyhedral elements and quad type boundary layers elements are used, while the acoustic mesh adopted for OpenCFS has tetra and wedge elements only.
- In the FIRE M Hybrid workflow, the right end side of the PCWE equation was computed from the total derivative while Star-ccm+ uses the substantial derivative that also includes the convective effects.

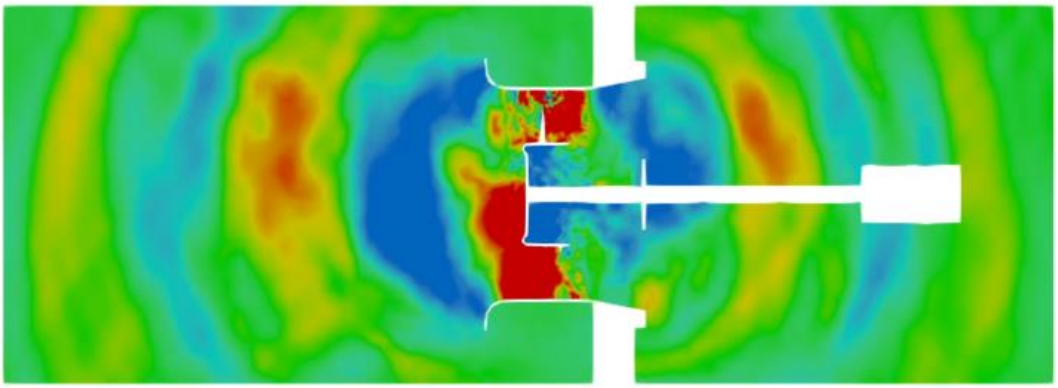

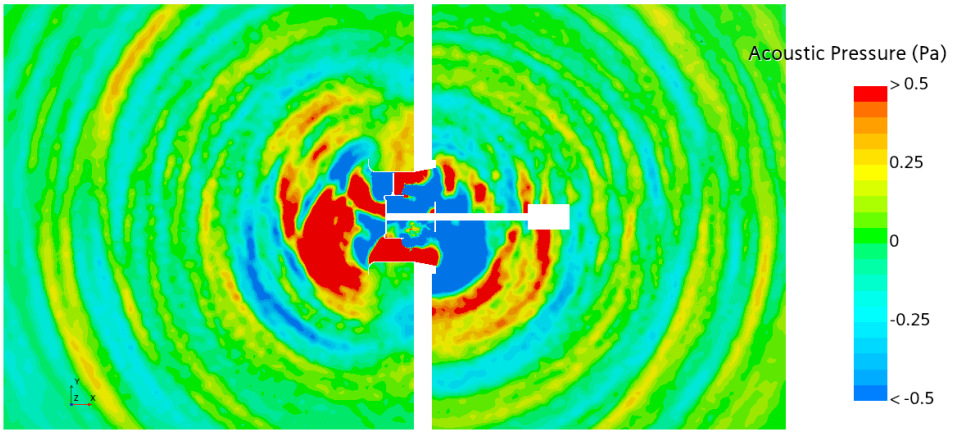

Figure 6.24: Acoustic pressure calculated by OpenCFS (top) and by Star-ccm+ (bottom)

In Figure 6.24 it is possible to observe the results of the OpenCFS simulation with the PCWE acoustic model, compared to the results of Star-ccm+ PCWE module. The acoustic pressure seems consistent between the two software and the width of the waves is comparable.

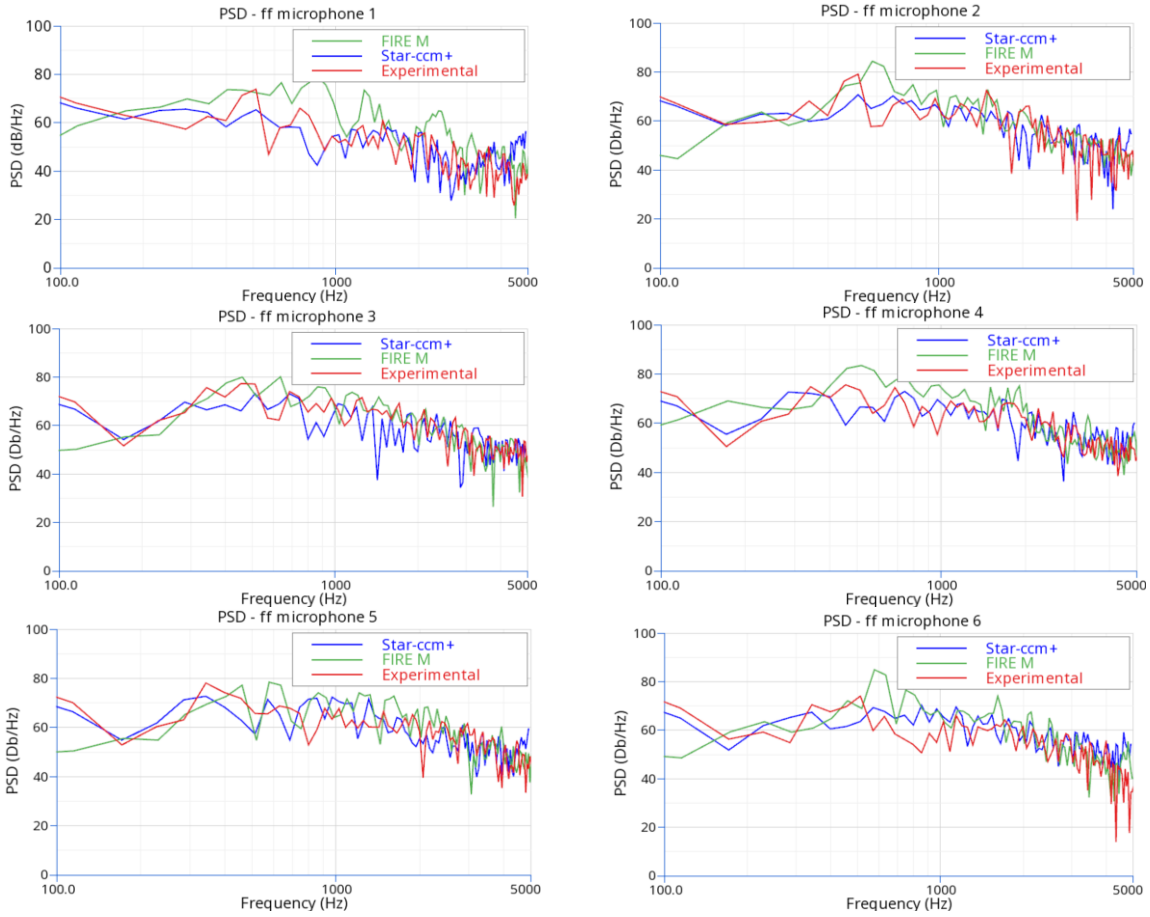

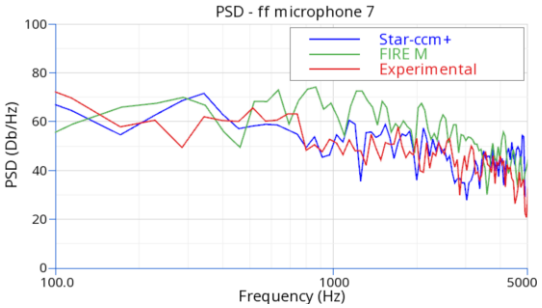

Figure 6.25: PSD of acoustic pressure on far-field microphones 1 to 7

In *Figure 6.25* it is possible to see the results of the Power Spectral Density (PSD) computed on the acoustic pressure evaluated on the far-field microphones. The signal length is too short to be able to see any meaningful frequency on the spectrum, but, once again, it is possible to observe some consistency in the results provided by Star-ccm+ and FIRE M.

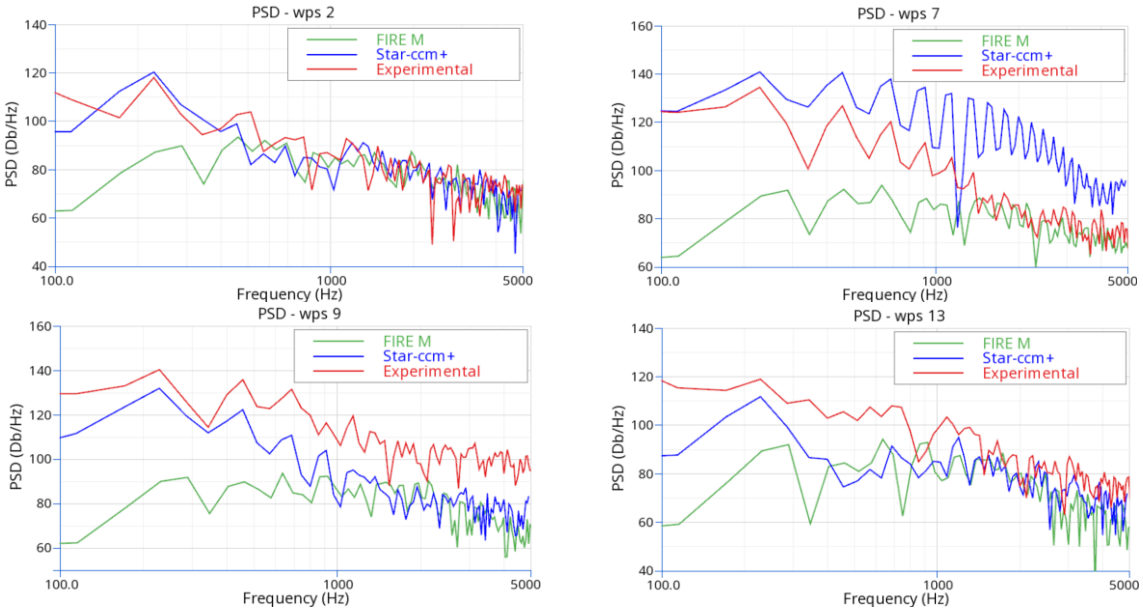

Figure 6.26: PSD of acoustic pressure on wall pressure sensors 2, 7, 9, 13

In *Figure 6.26* it is still possible to see the consistency in capturing the Blade Passing Frequency and its harmonics. Some differences are found in the amplitude of the graphs: doing a comparison with the experimental results, it is shown that the lower frequencies of the spectrum are better resolved by Star-ccm+ while the higher frequencies are better resolved by FIRE M. Two possible explanations for this behavior are:

- The time signal is too short in order to capture the correct Power Spectral Density value.
- The convective term of the substantial derivative of the right-end-side of the PCWE equation $-\frac{1}{\rho c_0^2}\frac{Dp_{ic}}{Dt}$, which in FIRE M was ignored, in the blade tip area where the flow speeds as well as the spatial pressure gradients are great, has an important contribution to the noise. Therefore, the OpenCFS results are under-estimated.

It is therefore possible to validate the Hybrid acoustic workflow developed in FIRE M.

Chapter 7: Conclusions

This chapter will provide some concluding remarks on the work conducted for this thesis. *Section 7.1* will present the conclusions drawn from the results obtained throughout this research. Following that, *Section 7.2* will offer some insights into potential future developments related to this work.

7.1 Conclusions

Throughout this report, it has been shown that the use of the Perturbed Convective Wave Equation model in Star-ccm+ is able to capture the key frequencies of the axial fan with good accuracy.
Using the Large Eddy Simulation turbulence model, it is possible to compute the turbulent structures that originate the noise. Keeping the $y^+ \approx 1$ criterion is necessary in order not to rely on wall treatments which were not available in FIRE M. Furthermore, by ensuring that the criterion is satisfied, it is possible to count on the fact that the turbulence in the near wall region, in particular in the viscous sublayer, is correctly modelled.
From the Power Spectral Density (PSD), it is possible to see that, 6,5 complete rotations of the fan, equal to 0.26 seconds of simulation time, have to be completed in order to be able to see the two tonal peaks created by the turbulence on the far-field microphones. But, with the performed simulation time, only far-field microphones number 5, 6 and 7 are able to capture it. The same simulation time is not enough to capture the First Blade Passing Frequency and its harmonics on the same microphone.
From the wall pressure sensors, it is possible to see that the Blade Passing Frequency is correctly captured in the near blade region. In this position, it is also possible to investigate the behavior of the hydrodynamic pressure in respect to the acoustic pressure. The first one, which can be only transported by convection, is not able to originate any signal on the sensors which are located away from the noise source; on the other end, the acoustic pressure waves are able to propagate in the whole domain and can be detected by all pressure sensors.
The comparation between FIRE M and Star-ccm+ acoustic result is not possible because, due to force majeure, the available simulation time in FIRE M is too little to be able to see the important frequency on the spectrum well resolved.
From the little data available it is still possible to validate the acoustic workflow developed during the course of this thesis.
From the CFD results a slight difference between the two software is expected. The fluid-dynamic quantities are consistent, especially in the region where the source terms are located.
Looking at the Q-criterion, in both cases, even if the velocities are slightly different, it is possible to see that the shape of the vortices, especially in the blade-tip region, are very similar. Therefore, a similar output for the PSD is expected.
Looking at the partial results obtained by FIRE M with OpenCFS, it is possible to conclude that the Hybrid workflow and the apps developed during this thesis work as intended. Unfortunately, it is not possible to capture the 2 subharmonic peaks of the spectrum because the simulation time is too short.

7.2 Future Work

In order to validate the results and finalize the comparison between FIRE M and Star-ccm+, the same simulation time and time-step is needed.
Further efforts can also be made in the selection of the models and solvers, so that the differences between the two software, especially during the CFD simulation, are minimal. Other differences also reside in the mesh used, in fact in the acoustic mesh used by FIRE M the type and size of the cells is different from those of the mesh adopted by Star-ccm+.
Finally, two more differences lie in the selection of the region where to apply the source terms: in the case of Star-ccm+, being included in the entire CFD domain, the sound sources that are created in the wake are also captured, whereas for FIRE M only the rotating region is selected as source, therefore the effects of the wake in the outlet region are lost.
In the source term of the PCWE computed in the FIRE M workflow, the convective term of the material derivative should be added.

Performing a Large Eddy Simulation (LES) is computationally demanding. Therefore, doing a comparison with Detached Eddy Simulation (DES) and/or Partially Averaged Navier-Stokes (PANS) turbulence models, would be beneficial. Indeed, these last two models are less computationally demanding. If a study comparing the reduction in simulation time to the loss of information reveals that the trade-off favors these two models, then it might be worthwhile to consider replacing LES simulations with them.

Appendix A

Cfsdat simulation setup file

```
<cfsdat xmlns="http://www.cfs++.org/simulation"
xmlns:xsi="http://www.w3.org/2001/XMLSchema-instance"
xsi:schemaLocation="http://www.cfs++.org/simulation  https://opencfs.gitlab.io/cfs/xml/CFS-
Dat/CFS_Dat.xsd">
    <pipeline>
        <stepValueDefinition>
            <startStop>
              <startStep value="0" />
              <numSteps value="10000" />
              <startTime value="0" />
              <delta value="0.00002" />
              <deleteOffset value="no" />
            </startStop>
        </stepValueDefinition>

        <meshInput id="input" gridType="fullGrid">
            <inputFile>
                <hdf5 fileName="Axial_Fan_AC.Q_PCWEt_Source.cfs" />
            </inputFile>
        </meshInput>

        <interpolation type="FieldInterpolation_Cell2Node" id="interpolation" inputFilterIds="input">
            <targetMesh>
                <hdf5 fileName="CA_Axial_Fan_AC.Q_PCWEt_Target.cfs" />
            </targetMesh>
            <singleResult>
                <inputQuantity resultName="acouRhsLoadP" />
                <outputQuantity resultName="acouRhsLoad" />
            </singleResult>
            <regions>
                <sourceRegions>
                    <region name="DOM_1_Fluid" />
                </sourceRegions>
                <targetRegions>
                    <region name="DOM_Fan" />
                    <region name="DOM_In" />
                    <region name="DOM_Out" />
                </targetRegions>
            </regions>
        </interpolation>

    <meshOutput id="PCWEt_nodal_loads" inputFilterIds="interpolation">
            <outputFile>
                <hdf5 extension="cfs" compressionLevel="6" externalFiles="no" />
            </outputFile>
            <saveResults>
                <result resultName="acouRhsLoad">
                    <allRegions />
                </result>
            </saveResults>
        </meshOutput>
    </pipeline>
</cfsdat>
```

Appendix B

OpenCFS simulation setup file

```
<cfsSimulation xmlns="http://www.cfs++.org/simulation"
xmlns:xsi="http://www.w3.org/2001/XMLSchema-instance"
xsi:schemaLocation="http://www.cfs++.org/simulation
https://opencfs.gitlab.io/cfs/xml/CFS-Simulation/CFS.xsd">
    <fileFormats>
        <input>
            <hdf5 fileName="results_hdf5/PCWEt_nodal_loads.cfs" />
        </input>

        <output>
            <hdf5 id="hdf5" />
            <text />
        </output>
        <materialData file="mat.xml" format="xml" />
    </fileFormats>

    <domain geometryType="3d" printGridInfo="no">
        <variableList>
            <var name="c0" value="332" />
        </variableList>

        <regionList>

            <region name="DOM_Fan" material="air" />
            <region name="DOM_In" material="air" />
            <region name="DOM_Out" material="air" />
            <!-- <region name="PML" material="air"/> -->
            <region name="DOM_PML_Inlet" material="air"/>
            <region name="DOM_PML_Outlet" material="air"/>
            <region name="DOM_PML_Sy1_y+" material="air"/>
            <region name="DOM_PML_Sy1_y-" material="air"/>
            <region name="DOM_PML_Sy1_z+" material="air"/>
            <region name="DOM_PML_Sy1_z-" material="air"/>
            <region name="DOM_PML_Sy2_y+" material="air"/>
            <region name="DOM_PML_Sy2_y-" material="air"/>
            <region name="DOM_PML_Sy2_z+" material="air"/>
            <region name="DOM_PML_Sy2_z-" material="air"/>

        </regionList>

        <surfRegionList>
            <surfRegion name="CIF_inlet_fan" />
            <surfRegion name="CIF_fan_inlet" />
            <surfRegion name="CIF_fan_outlet" />
            <surfRegion name="CIF_outlet_fan" />
        </surfRegionList>

        <ncInterfaceList>
            <ncInterface name="INT_Fan_Inlet" masterSide="CIF_inlet_fan" slaveSide="CIF_fan_inlet">
                <rotation rpm="1486.0" movingSide="slave" coordSysId="rotating" />
            </ncInterface>
            <ncInterface name="INT_Fan_Outlet" masterSide="CIF_outlet_fan" slaveSide="CIF_fan_outlet">
                <rotation rpm="1486.0" movingSide="slave" coordSysId="rotating" />
            </ncInterface>
        </ncInterfaceList>

        <nodeList>
            <!-- far field microphones-->
            <nodes name="ff1">
                <coord x="0.0" y="0.0" z="1.0" />
            </nodes>
            <nodes name="ff2">
                <coord x="-0.500" y="0.0" z="0.86602540378" />
            </nodes>
            <nodes name="ff3">
                <coord x="-0.86602540378" y="0.0" z="0.500" />
            </nodes>
            <nodes name="ff4">
                <coord x="-1.0" y="0.0" z="0.0" />
            </nodes>
            <nodes name="ff5">
                <coord x="-0.86602540378" y="0.0" z="-0.500" />
            </nodes>
            <nodes name="ff6">
                <coord x="-0.500" y="0.0" z="-0.86602540378" />
            </nodes>
```

```
            <nodes name="ff7">
                <coord x="0.0" y="0.0" z="-1.0" />
            </nodes>

            <!-- wall p sensors -->
            <nodes name="wps2">
                <coord x="0.080" y="0.06470476127563019" z="0.2414814565722671" />
            </nodes>
            <nodes name="wps7">
                <coord x="0.155" y="0.06470476127563019" z="0.2414814565722671" />
            </nodes>
            <nodes name="wps9">
                <coord x="0.185" y="0.06470476127563019" z="0.2414814565722671" />
            </nodes>
            <nodes name="wps13">
                <coord x="0.245" y="0.06470476127563019" z="0.2414814565722671" />
            </nodes>
        </nodeList>

        <coordSysList>
            <cylindric id="rotating">
                <origin x="0" y="0" z="0" />
                <zAxis x="1.0" y="0.0" z="0.0" />
                <rAxis x="0.0" y="1.0" z="0.0" />
            </cylindric>
        </coordSysList>

    </domain>

    <sequenceStep index="1">
        <analysis>
            <transient>
                <numSteps>10000</numSteps>
                <deltaT>0.00002</deltaT>
            </transient>
        </analysis>

        <pdeList>
            <acoustic formulation="acouPotential">
                <regionList>
                    <region name="DOM_Fan" />
                    <region name="DOM_In" />
                    <region name="DOM_Out" />
                    <region name="DOM_PML_Inlet"  dampingId="dampPML_Inlet"/>
                    <region name="DOM_PML_Outlet" dampingId="dampPML_Outlet"/>
                    <region name="DOM_PML_Sy1_y+" dampingId="dampPML_Sy1_y+"/>
                    <region name="DOM_PML_Sy1_y-" dampingId="dampPML_Sy1_y-"/>
                    <region name="DOM_PML_Sy1_z+" dampingId="dampPML_Sy1_z+"/>
                    <region name="DOM_PML_Sy1_z-" dampingId="dampPML_Sy1_z-"/>
                    <region name="DOM_PML_Sy2_y+" dampingId="dampPML_Sy2_y+"/>
                    <region name="DOM_PML_Sy2_y-" dampingId="dampPML_Sy2_y-"/>
                    <region name="DOM_PML_Sy2_z+" dampingId="dampPML_Sy2_z+"/>
                    <region name="DOM_PML_Sy2_z-" dampingId="dampPML_Sy2_z-"/>

                </regionList>

                <ncInterfaceList>
                    <ncInterface name="INT_Fan_Inlet" formulation="Nitsche" nitscheFactor="40" />
                    <ncInterface name="INT_Fan_Outlet" formulation="Nitsche" nitscheFactor="40" />
                </ncInterfaceList>

                <dampingList>
                    <!-- 1 -->
                    <pml id="dampPML_Inlet">
                        <propRegion>
                            <direction comp="x"     min="-1.240"    max="-1.150"/>
                            <direction comp="y"     min="-0.450"    max="0.450"/>
                            <direction comp="z"     min="-1.200"    max="1.200"/>
                        </propRegion>
                        <type>inverseDist</type>
                        <dampFactor>1.0</dampFactor>
                    </pml>
                    <!-- 2 -->
                    <pml id="dampPML_Outlet">
                        <propRegion>
                            <direction comp="x"     min="1.359"     max="1.449"/>
                            <direction comp="y"     min="-0.450"    max="0.450"/>
                            <direction comp="z"     min="-0.450"    max="0.450"/>
                        </propRegion>
                        <type>inverseDist</type>
                        <dampFactor>1.0</dampFactor>
                    </pml>
                    <!-- 3 -->
                    <pml id="dampPML_Sy1_y+">
                        <propRegion>
                            <direction comp="x"     min="-1.150"    max="0.259"/>
                            <direction comp="y"     min="0.450"     max="0.540"/>
                            <direction comp="z"     min="-1.200"    max="1.200"/>
```

```
                        </propRegion>
                        <type>inverseDist</type>
                        <dampFactor>1.0</dampFactor>
                    </pml>
                    <!-- 4 -->
                    <pml id="dampPML_Sy1_y-">
                        <propRegion>
                            <direction comp="x"     min="-1.150"    max="0.259"/>
                            <direction comp="y"     min="-0.540"     max="0.450"/>
                            <direction comp="z"     min="-1.200"    max="1.200"/>
                        </propRegion>
                        <type>inverseDist</type>
                        <dampFactor>1.0</dampFactor>
                    </pml>
                    <!-- 5 -->
                    <pml id="dampPML_Sy1_z+">
                        <propRegion>
                            <direction comp="x"     min="-1.150"    max="0.259"/>
                            <direction comp="y"     min="-0.450"     max="0.450"/>
                            <direction comp="z"     min="1.200"    max="1.290"/>
                        </propRegion>
                        <type>inverseDist</type>
                        <dampFactor>1.0</dampFactor>
                    </pml>
                    <!-- 6 -->
                    <pml id="dampPML_Sy1_z-">
                        <propRegion>
                            <direction comp="x"     min="-1.150"    max="0.259"/>
                            <direction comp="y"     min="-0.450"     max="0.450"/>
                            <direction comp="z"     min="-1.290"    max="-1.200"/>
                        </propRegion>
                        <type>inverseDist</type>
                        <dampFactor>1.0</dampFactor>
                    </pml>
                    <!-- 7 -->
                    <pml id="dampPML_Sy2_y+">
                        <propRegion>
                            <direction comp="x"     min="0.359"      max="0.1359"/>
                            <direction comp="y"     min="0.450"    max="0.540"/>
                            <direction comp="z"     min="-0.450"   max="0.450"/>
                        </propRegion>
                        <type>inverseDist</type>
                        <dampFactor>1.0</dampFactor>
                    </pml>
                    <!-- 8 -->
                    <pml id="dampPML_Sy2_y-">
                        <propRegion>
                            <direction comp="x"     min="0.359"      max="0.1359"/>
                            <direction comp="y"     min="-0.540"    max="-0.450"/>
                            <direction comp="z"     min="-0.450"   max="0.450"/>
                        </propRegion>
                        <type>inverseDist</type>
                        <dampFactor>1.0</dampFactor>
                    </pml>
                    <!-- 9 -->
                    <pml id="dampPML_Sy2_z+">
                        <propRegion>
                            <direction comp="x"     min="0.359"      max="0.1359"/>
                            <direction comp="y"     min="-0.450"    max="0.450"/>
                            <direction comp="z"     min="0.450"   max="0.540"/>
                        </propRegion>
                        <type>inverseDist</type>
                        <dampFactor>1.0</dampFactor>
                    </pml>
                    <!-- 10 -->
                    <pml id="dampPML_Sy2_z-">
                        <propRegion>
                            <direction comp="x"     min="0.359"      max="0.1359"/>
                            <direction comp="y"     min="-0.450"    max="0.450"/>
                            <direction comp="z"     min="-0.540"   max="-0.450"/>
                        </propRegion>
                        <type>inverseDist</type>
                        <dampFactor>1.0</dampFactor>
                    </pml>
                </dampingList>

                <!-- the Sources are defined in this section -->
                <bcsAndLoads>
                    <rhsValues name="DOM_Fan">
                        <grid>
                            <defaultGrid quantity="acouRhsLoad" dependtype="GENERAL">
                                <globalFactor>
((x lt 0.060) ? 0 : (x lt 0.070)? 1/2*(1-cos((x-0.060)*pi/((0.070-0.060)))) : (x gt 0.226)? 1/2*(1-
cos((0.236-x)*pi/((0.236-0.226)))) : (x gt 0.236) ? 0 : 1)</globalFactor>
                                <globalFactor>
((t lt 1e-3)? 1/2(1-cos((t-5e-4)*pi/(1e-3-5e-4))) : (t lt 5e-4)? 0 : 1)</globalFactor>
                            </defaultGrid>
                        </grid>
```

```
                    </rhsValues>
                </bcsAndLoads>

                <!-- here it is possible to add the mean field (velocity) -->
                <!-- <flowList>
                    <flow name="MeanFlowField">
                        <grid dofs="all">
                            <defaultGrid quantity="acouRhsLoad" dependtype="CONST"
snapToCFSTimeStep="true" sequenceStep="1">
                                <globalFactor>1</globalFactor>
                            </defaultGrid>
                        </grid>
                    </flow>
                </flowList> -->



                <storeResults>
                    <nodeResult type="acouPotentialD1">
                        <allRegions />
                        <nodeList>
                            <nodes name="ff1" outputIds="txt" />
                            <nodes name="ff2" outputIds="txt" />
                            <nodes name="ff3" outputIds="txt" />
                            <nodes name="ff4" outputIds="txt" />
                            <nodes name="ff5" outputIds="txt" />
                            <nodes name="ff6" outputIds="txt" />
                            <nodes name="ff7" outputIds="txt" />
                            <nodes name="wps2" outputIds="txt" />
                            <nodes name="wps7" outputIds="txt" />
                            <nodes name="wps9" outputIds="txt" />
                            <nodes name="wps13" outputIds="txt" />
                        </nodeList>
                    </nodeResult>

                    <!-- debugging: check if spatial blending is applied-->
                    <nodeResult type="acouRhsLoad">
                        <allRegions />
                    </nodeResult>

                    <surfRegionResult type="acouPower">
                        <surfRegionList>
                            <surfRegion name="BND_I_Inlet" />
                            <surfRegion name="BND_O_Outlet" />
                        </surfRegionList>
                    </surfRegionResult>
                </storeResults>

            </acoustic>
        </pdeList>
    </sequenceStep>
</cfsSimulation>
```

Bibliography

[1] M. Kaltenbacher, Computational Acoustics, Springer, 2018.

[2] "All You Should Know About EV Battery Charging Station and Its Cooling Fan System," [Online]. Available: https://coolingfans.net/cooling-fan-system-in-electric-vehicle-charging-stations/.

[3] S. Glegg and W. Devenport, Aeroacustics of low mach number flows.

[4] S. Wright, The acoustic spectrum of axial flow machines, 1976.

[5] A. Renzo, Slides di Aeroacustica, Torino, 2021.

[6] D. D'Ambrosio, Slides di Fluidodinamica Computazionale - Computational Fluid dynamics.

[7] T. Daniela, Slides del corso di Flussi Turbolenti (Politecnico d Torino).

[8] J. Smagorinsky, General circulation experiments with the primitive equations: I. The basic experiment., Monthly Weather Review, 1963.

[9] "Simcenter STAR-CCM+ 2306 User Guide," SIEMENS, [Online]. Available: file:///app/starccm+/18.04.009-R8/STAR-CCM+18.04.009-R8/doc/en/online/STARCCMP/GUID-F22B59CB-90C2-45AD-BAF3-D20134833EBE.html.

[10] J. Tieber, Aeroacoustic sound sources in internal turbulent flows computed from Large-Eddy Simulation, Graz, 2018.

[11] Reynolds and Osborne, On the Dynamical Theory of Incompressible Viscous Fluids and the Determination of the Criterion, London, 1895.

[12] J. Boussinesq, Essai sur la th´eorie des eaux courantes, M´emoires pr´esent´es par divers savants `a l'Acad´emie des Sciences XXIII, 1877.

[13] "K-Omega Turbulence Models," [Online]. Available: https://www.simscale.com/docs/simulation-setup/global-settings/k-omega-sst/.

[14] F. Mendonça, A. Read, S. Caro, K. Debatin and B. Caruelle, Aeroacoustic Simulation of Double Diaphragm Orifices in an Aircraft Climate Cooling System, AIAA-2005-2976, 2005.

[15] D. Pope and J. Hardin, "An acoustic/viscous splitting technique for computational aeroacoustics," 1994.

[16] "AcousticPDE," [Online]. Available: https://opencfs.gitlab.io/userdocu/PDEExplanations/Singlefield/AcousticPDE/.

[17] Z. Florian, J. Clemens, K. Manfred and B. Stefan, "A Benchmark Case for Aerodynamics and Aeroacoustics of a Low Pressure Axial Fan," 2016. [Online]. Available: https://saemobilus.sae.org/papers/a-benchmark-case-aerodynamics-aeroacoustics-a-low-pressure-axial-fan-2016-01-1805.

[18] K. Florian, J. Clemens, B. Stefan, K. Manfred, C. Felix and S. Stefan, "Benchmark-Dataset FAN-01: Low pressure Axial Fan in a short Duct," [Online]. Available: https://zenodo.org/records/10787093.

[19] ISO 5801:2007, Fans — Performance testing using standardized airways, 2007.

[20] "SDT API Documentation : Simulation Desktop API R2023.2 documentation," [Online]. Available: https://ast-services.avl.com/sdt_api/R2023.2/getting_started/results.html.

[21] S. Schoder, C. Junger and M. Kaltenbacher, Computational aeroacoustics of the EAA benchmark case of an axial fan, 2020.

[22] [Online]. Available: https://physics.stackexchange.com/questions/281281/about-the-definition-of-boundary-layer.

[23] "Q-criterion for Vortex Visualization," [Online]. Available: https://www.m4-engineering.com/q-criterion-for-vortex-visualization/.

[24] S. Li, D. E. Rival and X. Wu, Sound source and pseudo-sound in the near field of a circular cylinder in subsonic conditions, Cambridge University Press, 2021.

[25] J. R. Ferrini, Development of CFD simulation methods, 2021.

[26] "Perfectly Matched Layer (PML)," [Online]. Available: https://opencfs.gitlab.io/userdocu/Tutorials/Features/pml/#usage-of-the-pml.

[27] "The HDF5 library and file format," [Online]. Available: https://www.hdfgroup.org/solutions/hdf5/.

[28] "hdfgroup: hdfview," [Online]. Available: https://www.hdfgroup.org/downloads/hdfview/.

[29] "openCFS," [Online]. Available: https://opencfs.org/.

[30] A. W. C. J. M. W. C. F. K. R. M. K. Stefan Schoder, Application Limits of Conservative Source Interpolation Methods Using a Low Mach Number Hybrid Aeroacoustic Workflow, Graz, 2021.

[31] [Online]. Available: https://opencfs.gitlab.io/userdocu/DataExplanations/ConservativeInterpolators/#cell-centroid-conservative-interpolation.

[32] "Ansys: Turbulent Boundary Layers : Basics of Turbulent Flows - Lesson6," [Online]. Available: https://courses.ansys.com/wp-content/uploads/2020/09/Basics-of-Turbulent-Flows-Lesson-6-Handout.pdf.

[33] "Large eddy simulation of magnetohydrodynamic turbulent channel flows with local subgrid-scale model based on coherent structures," [Online]. Available: https://pubs.aip.org/aip/pof/article-abstract/18/4/045107/915368/Large-eddy-simulation-of-magnetohydrodynamic?redirectedFrom=fulltext.

[34] Simcenter STAR-CCM+ 2310 User Guide, Theory - Turbulence - Scale-Resolving-Simulations - LES - Smagorinsky Subgrid Scale Model.